UNIVERSITY OF SOUTHAMPTON

FACULTY OF ENGINEERING, SCIENCE AND MATHEMATICS

School of Chemistry

Tailoring plasmonic substrates for SERS

By

Jonathon David Speed

Thesis for the degree of Doctor of Philosophy

October 2010

UNIVERSITY OF SOUTHAMPTON

ABSTRACT

FACULTY OF ENGINEERING, SCIENCE AND MATHEMATICS

School of Chemistry

Doctor of Philosophy

TAILORING PLASMONIC SUBSTRATES FOR SERS

By Jonathon David Speed

SERS is a useful spectroscopic technique that was discovered 30 years ago, and has recently seen a renaissance in research. Sphere segment void (SSV) substrates have been developed as reproducible, stable SERS substrates by electrodeposition of a metal through a colloidal template.

The effect of adsorbing an organic monolayer on the surface of an SSV substrate was studied, which results in a slight shift in the plasmonic absorption. This was compared with the reduction of a diazonium salt on the surface, which results in a significant increase in plasmonic absorption, attributed to a physical sharpening of the metal structure, and in turn better defined plasmon modes.

The Au surface was also modified with an ultra thin layer of Pt, and a comparison was made between oxidation-reduction cycled roughened (ORC) and SSV substrates with and without Pt. The SSV substrates were found to be more reproducible, and (after modification with a thin-layer of Pt), gave spectra more representative of bulk Pt substrates than ORC.

Lastly the surface was functionalised with metallic nanoparticles (NPs), and a large increase in spectral intensity was observed. This was attributed to a strongly localised electric field between the NP and the substrate, which resulted in an additional enhancement of between 10^2-10^3 depending on the method of assembly used. Functionalisation of the NPs introduced the possibility of drug detection or studies in drug delivery using such a system.

TABLE OF CONTENTS

DECLARATION OF AUTHORSHIP

I, **Jonathon David Speed** declare that the thesis entitled

Tailoring Plasmonic Substrates for SERS

and the work presented in the thesis are both my own, and have been generated by me as the result of my own original research. I confirm that:

- this work was done wholly or mainly while in candidature for a research degree at this University;
- where any part of this thesis has previously been submitted for a degree or any other qualification at this University or any other institution, this has been clearly stated;
- where I have consulted the published work of others, this is always clearly attributed;
- where I have quoted from the work of others, the source is always given. With the exception of such quotations, this thesis is entirely my own work;
- I have acknowledged all main sources of help;
- where the thesis is based on work done by myself jointly with others, I have made clear exactly what was done by others and what I have contributed myself;

Signed: ……..

Date:…….

ACKNOWLEDGEMENTS

First and foremost I would like to thank my supervisor Prof. Andrea Russell for all her help, expertise, enthusiasm, advice, but most importantly for putting up a fight for me, and taking me on in the first place. I will always remember the difference between “marry”, “Mary” and “merry”, and will never forget metal-ion-sock-puppet-theatre...no matter how hard I try.

I would also like to thank my advisor, Prof. Phil Bartlett, Prof. Jeremy Baumberg, Dr Suzanne Cintra, Dr Sumeet Mahajan, James Hugall and Niraj Lal for their help and advice with electrochemistry, substrate preparation and optical measurements. I am also grateful to Alastair Clarke who made all my gold and palladium slides, as well as taught me how to use the SEM. And of course Prof. Patrick Hendra, whose lectures on “how to build a spectrometer from scratch” have proved invaluable, as well as his bespoke SERS cells.

Thanks must also go to Russell and Bartlett groups: Dr Gale Chouchlemane, Prabalini Kannan, Dr Maciej Sosna, Dr David Cook, Dr Jatin Sinha, Ahmet Celiktas, Thomas Esterle, Pete Richardson, Rosemary Baker, and Dr Laura Cavillo. Also to Anna Wise (who’d have thought steak and cocktails were an important part of scientific research?), Stephen Price (I’m NEVER driving to Yeovil again...), Dr Katie Blaney (“Small or large wine” “I’ll let you decide”), Dr Fabrice Birembaut (one gin is more than enough), and Rob Johnson (I hope Zippy, George and Bungle serve you well). Not forgetting Pat Dear, who has kept me fuelled with coffee for the last three years.

I’d also like to thank the numerous friends I’ve met through TG, who have let me bounce ideas of them, taken me to the Edinburgh Festival, and generally kept me (more or less) sane. Lastly I want to express my gratitude to my family, who have put up with me for the last 25 years, who have never tried to stop me doing anything, and have supported everything I’ve ever undertaken, thank you.

ABBREVIATIONS

IR	Infrared
SERS	Surface enhanced Raman spectroscopy
EM	Electromagnetic
CT	Charge transfer
SAS	SERS active sites
ORC	Oxidation reduction cycle
MFON	Metal film over nanoparticle
SSV	Sphere segment void
BT	Benzenethiol
DMF	Dimethyl formamide
IPA	Isopropyl alcohol
SDS	Sodium dodecyl sulphate
CV	Cyclic voltammogram
SCE	Saturated calomel electrode
MMS	Mercury-mercury sulphate electrode
SEM	Scanning electron microscope
FT	Fourier transform
NA	Numerical aperture
DS	Diazonium salt
TU	Thiouracil
EDX	Energy dispersive Xray
TERS	Tip enhanced Raman spectroscopy
NP	Nanoparticle
MA	Mercaptoaniline
MBA	Mercaptobenzoic acid
FG	Flat gold
MP	Mercaptopyridine
MUA	Mercaptoundecanoic acid

1. Introduction

1.1. General introduction

With the ever increasing catalogue of known chemicals, reactions and processes involved in modern society a scientist's ability to monitor their experiments needs to improve in parallel. One important weapon in such a scientific arsenal is molecular spectroscopy.

Vibrational spectroscopy is a very useful analytical technique as it provides information on the chemical identity of a compound, its structure and its environment. It is also non-destructive and quick. Both Raman and infrared (IR) spectroscopies offer these benefits, but IR is very difficult to use in aqueous environments. It requires very thin layers of solvent or electrolyte to be used effectively; whereas the Raman cross section of water is low, which enables Raman to be used in a variety of environments.

1.2. Raman Spectroscopy

The one great drawback of Raman spectroscopy is that it is a very weak process, with only 1 in 10^{12} photons undergoing Raman scattering. However, by utilizing resonance Raman spectroscopy (RRS) and surface enhanced Raman spectroscopy (SERS) the effect may be greatly enhanced.

Whilst IR spectroscopy is an absorbance process, Raman scattering relies on emission from the target, induced by irradiation from a laser; the process is shown in Figure 1-1. The molecule undergoes excitation to a virtual state, and during relaxation can return to its original vibrational state (Rayleigh scattering), a higher vibrational state (Stokes scattering) or a lower vibrational state (anti-Stokes).

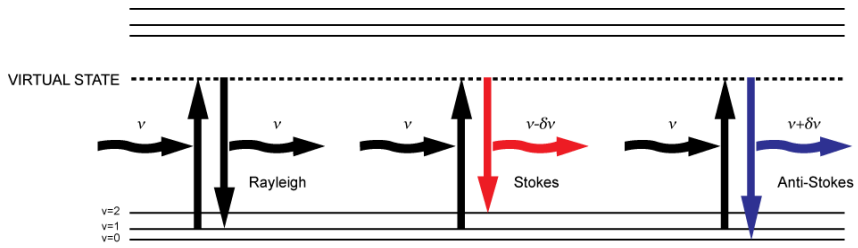

Figure 1-1 – Diagram of excitation to virtual state and relaxation resulting in Rayleigh, Stokes and anti-Stokes emission

This was first demonstrated by C.V. Raman in 1928 [1] whilst observing the spectrum of liquid benzene. In the following 80 years, Raman spectroscopy has developed to become one of the most powerful tools to investigate molecular structure.

1.3. Quantum theory of Raman scattering

The intensity of Raman scattering, *I*, is given [2] in the following equation:

$$I = Kl\alpha^2\omega^4$$

Equation 1

where *K* is a constant derived from the speed of light, *l* is the laser power, ω is the frequency of incident radiation and α is the polarisability of the molecule. The polarisability of a molecule can be calculated from the Kramer Heisenberg Dirac equation, shown below:

$$(\alpha_{\rho\sigma})_{GF} = k\sum_{I}\left(\frac{\langle F|r_\rho|I\rangle\langle I|r_\sigma|G\rangle}{\omega_{GI} - \omega_L - i\Gamma_I} + \frac{\langle I|r_\rho|G\rangle\langle F|r_\sigma|I\rangle}{\omega_{IF} + \omega_L - i\Gamma_I}\right)$$

Equation 2

where ρ and σ are the incident and scattered polarization directions. *G* is the ground vibronic state, *I* is the vibronic state of an excited electronic state, and *F* is the final vibronic state of the ground state. *F* and *G* are represented diagrammatically in Figure 1-1 as $v = 2$ and $v = 1$ (for Stokes scattering) and $v = 0$ and $v = 1$ (for anti-Stokes scattering).

The numerator models the excitation process, and consists of two integrals. Taking the left hand integral as an example, it models starting in the ground state *G*, ending in an excited state, *I*, using the dipolar operator, r_σ. The left hand term describes the process starting from the ground state, whilst the right hand term represents starting form a different excited state. The process is summed over all possible states, and eventually models the entire excitation of the molecule.

The denominator is used to model the virtual state of the excited molecule. $i\Gamma_I$ represents the lifetime of the excited state, and is very small in comparison to the energies of ω_{GI} and ω_L. Whilst small, the $i\Gamma_I$ term is vitally important to the first part of the equation, as otherwise when the frequency of the incident light were the same

of an electronic transition then the denominator would be infinite. It is worth noting that in the second part of the equation the frequencies are summed, making the denominator large, which in turn makes modeling the excitation from a non-ground state much less important than modeling the excitation from the ground state itself.

1.4. Classical theory of Raman scattering

A full understanding of the quantum theory of Raman scattering is beyond the scope of this work, and to understand the process of SERS, the effect will be explained in terms of the classical theory of Raman scattering.

Suppose a light wave of frequency v_0 with electric field strength E is incident on a sample, then:

$$E = E_0 \cos 2\pi v_0 t$$

Equation 3

where E_0 is the amplitude and t is time. If this light wave irradiates a diatomic molecule, the dipole moment, μ, can be given by:

$$\mu = \alpha E = \alpha E_0 \cos 2\pi v_0 t$$

Equation 4

If the molecule is vibrating with frequency v_1 then the nuclear displacement, Q, can be given by:

$$Q = Q_0 \cos 2\pi v_1 t$$

Equation 5

where Q_0 is the vibrational amplitude. If the amplitude of vibration is small, α can be described as a linear function of Q. Therefore:

$$\alpha = \alpha_0 + \left(\frac{\partial \alpha}{\partial Q}\right)_0 Q$$

Equation 6

where α_0 is the polarisability at the equilibrium position and $\left(\frac{\partial \alpha}{\partial Q}\right)_0$ is the rate of change of the polarisability with respect to the change in the nuclear coordinate, Q. By combining Equation 4, Equation 5 and Equation 6 the dipole moment can be expressed as:

$$\mu = \alpha E_0 \cos 2\pi v_0 t$$

$$= \alpha_0 E_0 \cos 2\pi v_0 t + \left(\frac{\partial \alpha}{\partial Q}\right)_0 Q_0 E_0 \cos 2\pi v_0 t \,.\cos 2\pi v_1 t$$

$$= \alpha_0 E_0 \cos 2\pi v_0 t + \frac{1}{2}\left(\frac{\partial \alpha}{\partial Q}\right)_0 Q_0 E_0 [\cos\{2\pi(v_0 + v_1)t\} + \cos\{2\pi(v_0 - v_1)t\}]$$

Equation 7

The first part of Equation 7 describes radiation of an oscillating dipole with the same frequency of the incident photon, (Rayleigh or elastic scattering). The second term gives the Raman scattering of the photon with frequencies $v_0 + v_1$ (anti-Stokes) and $v_0 - v_1$ (Stokes). The most important part of the equation is the $\left(\frac{\partial \alpha}{\partial Q}\right)$ term, as this denotes there must be a change in the polarisability of the molecule during vibration, or the Raman scattering term is equal to zero.

1.5. Surface enhanced Raman spectroscopy (SERS)

SERS was first observed in Southampton University in 1974 when Fleischmann *et al* [3] recorded a spectra of pyridine 10^6 times more intense than expected on an electrochemically roughened silver electrode. Initially the increase was attributed to a larger surface area, but Creighton and Jeanmaire [4, 5] both suggested that this could only lead to a 10 fold increase in intensity, and that some other system must be at play.

1.5.1. Electromagnetic Enhancement

It is known that in a system with a structure smaller than the wavelength of light, it is possible to excite plasmons on the surface of the structure [6-9]. This in turn leads to an increase in local electric field intensity. The electric field of the substrate (E_s) can be represented by the following equation:

$$E_S = gE_0$$

Equation 8

where g is the averaged field enhancement across the substrate and E_0 is the incident radiation. So from Equation 4:

$$\mu \propto \alpha g E_0$$

Equation 9

and the amplitude of the SERS field, E_{SERS}, will be:

$$E_{SERS} \propto \alpha g g' E_0$$

Equation 10

where g' is the averaged field enhancement for Raman scattered light.

The SERS intensity, I_{SERS} will be proportional to the square of E_{SERS}:

$$I_{SERS} \propto |\alpha|^2 |g g'|^2 I_0$$

Equation 11

where I_0 is the intensity of the incident radiation. The enhancement of the SERS effect of the metal compared to non-enhanced Raman, G, can be described as:

$$G = \left|\frac{\alpha_R}{\alpha_{R0}}\right| |g g'|^2$$

Equation 12

where α_R is the polarisability of the bound molecule, and α_{R0} the polarisability of the free molecule, (the impact in change of polarisabilities will be discussed in section 0). In the low frequency region, where $g \sim g'$, then $G \propto |g|^4$, which means a relatively small increase in electric field enhancement which can lead to a very large increase in Raman intensity. This is known as the electromagnetic enhancement (EM).

The size of the surface's topographical features is crucial to this effect: if the structure is smaller than ~ 5 nm then the conductive ability of the structure is reduced due to electronic scattering; if the size is larger than ~ 100 nm then surface plasmons become multipoles, which do not lead to SERS. Dipolar plasmons can be thought of as a standing oscillation of the surface electrons in the structure, leading to an increase in local electric field.

The electronic configuration of the metal used also plays a role in the SERS properties of the substrate used. Metals with one electron in their outer shell (such as the alkali metals) [10] exhibit strong SERS. The electron is easily excited into a surface plasmon, resulting in strong EM enhancement. The high reactivity of the alkali metals has limited their use, however, and the vast majority of SERS research has been performed on the coinage metals (Cu [11], Ag [3, 4, 12-14] and Au [15]).

In recent years, SERS enhancements have been reported on Pt group metals [16, 17], and even UV SERS on other transition metals [18-21].

1.5.2. Charge Transfer

As shown in Equation 12, the SERS enhancement from a substrate is not due to the EM enhancement alone, the polarisability of the molecule is also an integral factor. If there is no change in polarisability, then $\frac{\alpha_R}{\alpha_{R0}} = 1$ and the enhancement becomes solely dependant on EM enhancements. However, binding an adsorbate to the surface of the metal sometimes results in metal-to-adsorbate charge transfer (CT) that can lead to a modest enhancement in signal. Otto has written an excellent explanation on the 'electronic effects' of SERS [22].

In order to observe CT enhancement, an electron from the metal must be transferred to the adsorbate. This leads to a change in polarisability for certain vibrations. The exact mechanism depends on the metal used, as electron-hole pairs play an important role. In the case of 'slow moving' electrons and holes (such as the case of cobalt [23]), then the mechanism is as follows:

$$M + Ads \xrightarrow{v_{laser}} M^+ + Ads_{\pi^* occupied} \xrightarrow{v_{stokes}} M + Ads_{vibrating}$$

Scheme 1-1

However, in the case of a metal with 'fast moving' electrons and holes, this is not the case. For example, in the case of ethylene on Ag, the electron is transferred into the π^* antibonding orbital, resulting in a *ν*(C-C) stretch. However, this effect is not observed on flat Ag as the time the electron spends in the antibonding orbital (~5 fs), is comparable to the time it takes the resulting hole to leave the surface, and recombine with another electron. This results in an electron-hole excitation continuum in the place of a Raman band. When the silver is nanostructured, the areas of structure result in 'hole-retention sites' – or SERS active sites (SAS), that trap the hole for long enough for the CT induced vibration to occur, resulting in SERS. The scheme in this instance is as follows:

$$Ag_{SAS} + C_2H_4 \xrightarrow{v_{laser}} Ag^+_{SAS} + C_2H_{4_{\pi^* occupied}} \xrightarrow{v_{stokes}} Ag_{SAS} + C_2H_{4_{vibrating}}$$

Scheme 1-2

The major limitations to the CT enhancement are that the adsorbate must be chemisorbed to the surface of the metal, and that the enhancement is chemical specific. It is also strongly perturbed by the application of a potential across the system. This means both that the effect may be investigated by electrochemistry, but also that using the effect to study electrochemical systems is virtually impossible.

1.6. SERS Substrates

Numerous research groups have designed their own surfaces, normally for a particular application, and as such SERS substrates come in a variety of shapes, sizes and composition, but fall into three main categories. These are: roughened, colloidal, and nanostructured, each of which will be presented below.

1.6.1. Roughened Substrates

The simplest form of SERS substrate is the roughened surface (see Figure 1-2), and the most common way to create one is *via* electrochemical roughening using an oxidation-reduction cycle (ORC).

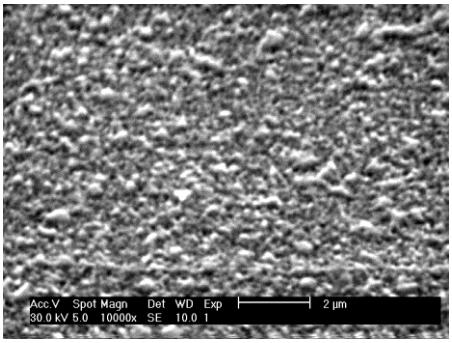

Figure 1-2 – Scanning electron micrograph of an ORC roughened silver substrate

In a typical ORC, the substrate is held at a potential where the metal exists in metallic form, then quickly swept to a more positive potential to oxidize it, held there for a second or two, then quickly swept back to deposit the metal back in its solid form. The process creates peaks all over the surface of the metal (see Figure 1-3) that both act as SAS in the CT mechanism, and generate plasmons for the EM

mechanism.

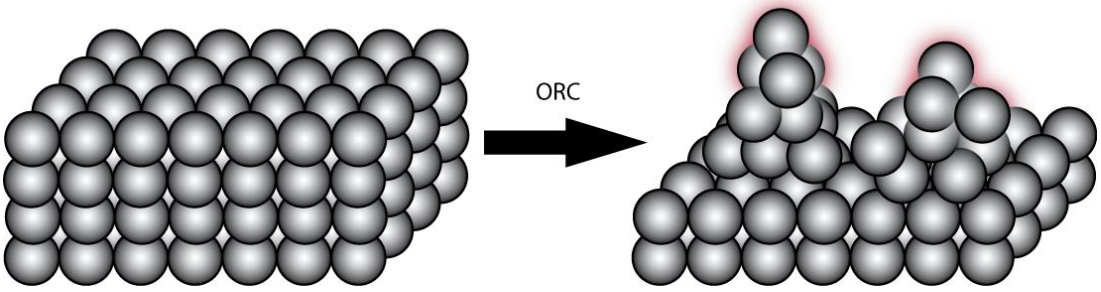

Figure 1-3 – Schematic of flat silver surface to ORC roughened

The ORC SERS substrate was first created by Fleischmann [3], and due to their relative ease of fabrication they have been used for a wide variety of spectroscopic experiments, ranging from electrochemical [24-29] to detection of drugs or other small molecules [14, 30-32]. A major drawback with this technique, is the chaotic nature of the resulting substrates. Electrochemically roughening a surface is relatively simple, but maintaining control over its surface topography and understanding the resulting SERS enhancements is not.

Tian [33] has developed and refined the process of roughening, on a wide variety of metals, including Au, Ag, Cu, Pt and Rh. In an experiment with Ni surfaces he prepared the substrates by mechanically polishing, chemical etching, *ex situ* and *in situ* roughening, before taking the spectrum of pyridine. Predictably, the mechanically polished surface gave very poor signal (although a signal was obtained, indicating roughness at some level). The chemical etching showed much better enhancement, (about 20 times the signal), which was beaten by *ex situ* roughening (about 50 times the original signal), but if the roughening was performed *in situ* with the pyridine present, then the enhancement was double the *ex situ* (about 100 times the original). All of these substrates were, however, superseded by an array of organized nanorods (see 1.6.3).

Another way of creating a roughened surface is to grow a silver film under kinetically controlled conditions, and the most common way to do this is *via* deposition of silver from Tollens reagent and glucose [34]. In this method, a clean glass slide is introduced to a solution of $[Ag(NH_3)_2]^+$ and glucose, before heating to 55 °C. This causes the silver to deposit onto the slide, with a very rough morphology (see Figure 1-4).

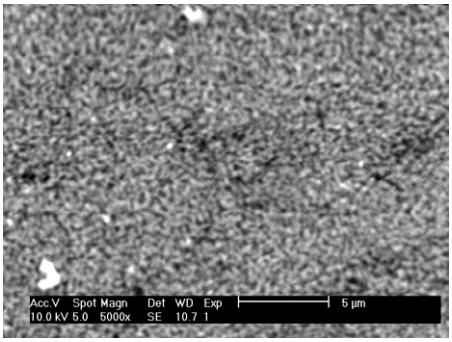

Figure 1-4 - Scanning electron micrograph of a Tollens silver substrate

These surfaces are suitable rough to show SERS enhancement, and recent work by Shegai *et al.* [35] have shown that near single-molecule detection and electrochemical experiments are possible on them too. However, as in ORC roughened substrates, there is no uniformity to the SERS enhancement, and low detection limits are only observed when on a 'hot-spot', (an area where conditions on the surface are perfect for SERS to occur reliably).

Another method of creating a roughened surface involves creating nanoparticles or nanostructures, then fixing them to an otherwise flat surface, resulting in a SERS active surface. A common approach is to use nanoparticles [36] (discussed in more detail below), or nanowires [13]. These surfaces tend to be more ordered than ORC substrates, but still depend on 'hot-spots' from their inherent roughness.

1.6.2. Metallic Colloids and Nanoparticles

Due to its ability to provide detailed information in aqueous media, it is unsurprising that SERS has found its way into biological and biochemical research. Flat surfaces, are not suitable for many biological experiments, particularly *in vivo* studies. A suitable alternative to the rigid electrode or substrate is to use a colloidal suspension of nanoparticles. In much the same way as a roughened substrate produces plasmons across its surface, a nanoparticle can also exhibit plasmonic resonance.

The first reported SERS from nanoparticles was performed by Albrecht and Creighton [37] in 1979, in a similar experiment to Fleischmann. Nanoparticles were prepared by reduction of the metal salt (dilute solutions of $Ag[NO_3]$ or $K[AuCl_4]$ were added to ice cold solutions of $Na[BH_3]$ and stirred). The brightly coloured solutions were found to contain particles of sizes between 1-50 nm, and were highly stabled, with no colour change or precipitation for several weeks.

After addition of pyridine (100 mM solution) the particles almost immediately began to aggregate, which was evident from the colour change. The aggregation led to a large change in the UV spectrum, with a decrease in absorption maximum, but more notably a red-shift in the position of the maximum. When tested for Raman activity, the sols showed notably strong bands at 1038, 1010 and 228 cm^{-1}. This is characteristic for pyridine, and with intensities ~5 times greater than the sample of 100 mM aqueous pyridine.

Since then, a veritable plethora of colloidal based SERS systems have been developed, ranging from spherical particles [38], to depositing the particles onto surfaces [36], to biological [39] or even *in vivo* use [40].

1.6.3. Rationally Designed Nanostructured Substrates

The third type of common SERS substrate is the rationally designed substrate. These can consist of a variety of different shapes and methods, but all contain a uniform, reproducible structure. There are some very good reviews on plasmonic nanostructures, notably those by Vo-Dinh [41] Banholzer and Millstone [42]. The majority of nanostructures are made by various processes of lithography.

One of the most reproducible methods that fall into this category is electron-beam lithography [43, 44]. A polymer electron-sensitive resist is etched by the electron-beam, and chemically developed (usually in a MIBK/IPA solution). The template is then coated with Au from an evaporator, resulting in a periodic array of nanofeatures.

Another type of substrate created by metal evaporation is the metal film over nanosphere (MFON) surface. This was first reported by Van Duyne *et al.* in 1993 [45, 46]. In this substrate, a solution of nanospheres is deposited onto a glass slide, which then form a hexagonal array. A thin film of Ag is then evaporated on top of the nanospheres, resulting in a continuous (albeit quite rough) metal film (see Figure 1-5).

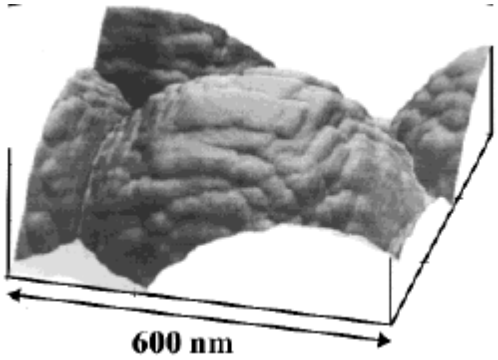

Figure 1-5 – Atomic force microscopy image of a MFON substrate taken from [46]. The structure consists of a 200 nm layer of Ag evaporated over 542 nm latex spheres.

These substrates are tunable in the respect that the size of the spheres and the thickness of the metal film can be altered to suit the excitation wavelength. A structure such as this has been shown to give an enhancement of 10^7 with a 532 nm laser. The MFON substrates were one of the first wholly reproducible SERS substrates, but were still fairly rough (as can be seen from Figure 1-5), although a lot smoother than the ORC or Tollens substrates (see 1.6.1).

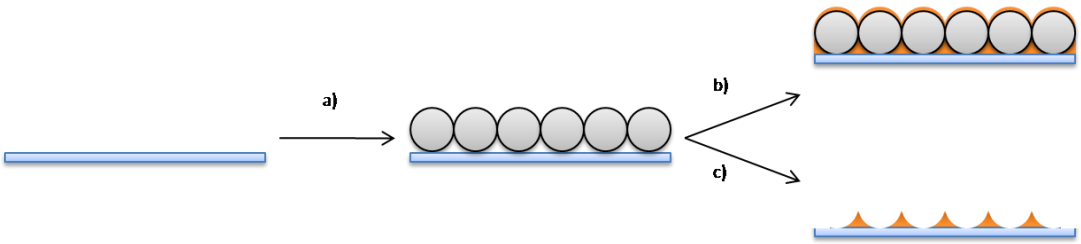

Figure 1-6 – Schematic of MFON and colloidal mask substrate formation. a) Formation of nanosphere array on glass slide, b) evaporation of film onto nanospheres to form MFON, c) evaporation of metal, followed by removal of spheres to form colloidal mask substrate.

If the metal is deposited through the spheres, (which are then removed), then an array of triangular nanoparticles is formed [47, 48] (see Figure 1-6). These substrates – known as colloidal mask substrates - exhibit comparable enhancements to the MFON substrate, with enhancements typically in the range of 10^7.

1.7.Sphere Segment Void substrates

The MFON substrates exhibit a high enhancement, are reproducible and stable, but are limited by the need to be able to evaporate the metal required. They are also still fairly rough, and whilst tunable to a degree, this is still fairly limited. If nanosphere lithography is combined with electrodeposition of the metal, a hexagonal array of

spherical nanovoids is created. This is known as a sphere segment void (SSV) substrate (see Figure 1-7) [49].

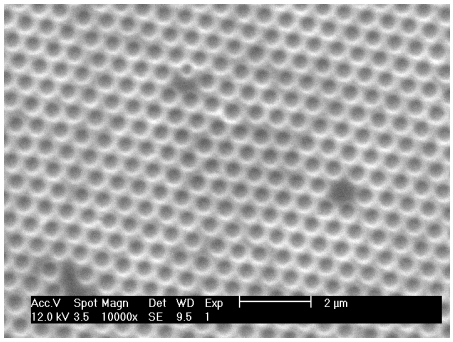

Figure 1-7 - Scanning electron micrograph of a Au SSV substrate. The pores are 600 nm in diameter and the film height is 0.75 *d*.

The size of the sphere and film height can be controlled independently, allowing for fine tuning of the substrate for a specified excitation wavelength. The normalized film height, *d*, is given as the film height (*t*) / sphere diameter (*D*), (see Figure 1-8). So for a sphere 600 nm in diameter, and a film height of 450 nm, $d = 0.75$.

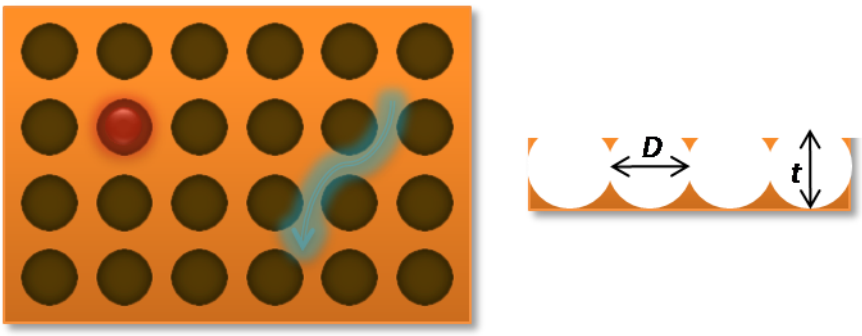

Figure 1-8 – Schematic of SSV substrate from above and side on. The Bragg plasmon is shown in blue, and the Mie plasmon in red.

SSV substrates give rise to two different types of plasmon, delocalized surface plasmons, formed from the periodic grating-type structure (a Bragg plasmon); and localized plasmons constrained to the voids, (Mie plasmons). Because both types of plasmons are generated by different facets of the structure, they are tunable in different ways.

1.7.1. Bragg plasmons

The surface plasmons present in an SSV substrate are known as Bragg plasmons because they are created from a periodic array of corrugations across the surface. The energy of these plasmons can be calculated from the following equation:

$$E = \hbar c \sqrt{\epsilon_m^{-1}(E) + \epsilon_d^{-1} f(\varphi) |\boldsymbol{k_0} sin\theta + \boldsymbol{q}_m|}$$

Equation 13

where $\epsilon_m^{-1}(E)$ is the energy dependant dielectric constant of the Au, ϵ_d^{-1} is the dielectric constant of the surrounding media, $f(\varphi)$ is a function that accounts for the sample orientation, $\boldsymbol{k_0}$ is the wave vector of the incident light, θ is the angle of incidence, and finally $\boldsymbol{q}_m$ is a factor of the spacing between voids [50]. Equation 13 shows that the energy of a given plasmon is dependant not only on the material used, and wavelength of light, but also the angles of incidence and azimuth..

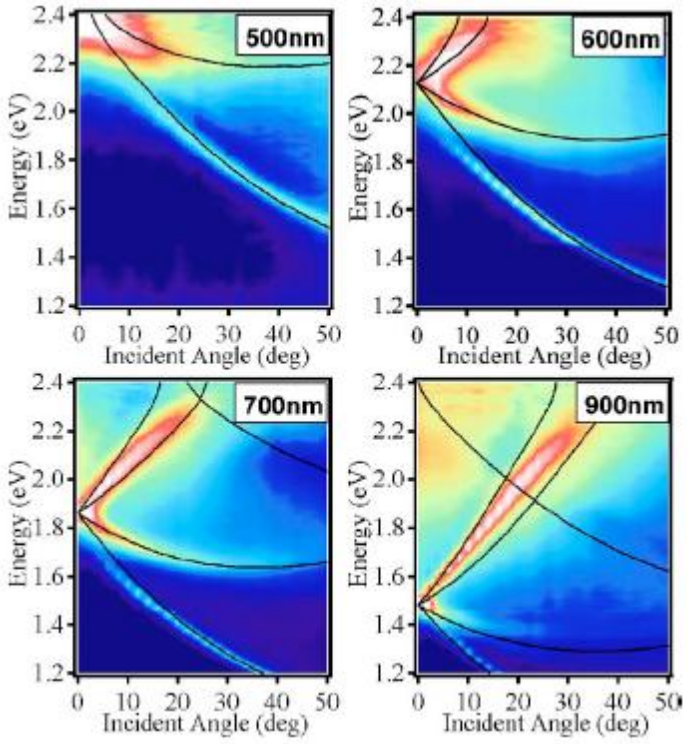

Figure 1-9 – Reflectance plots of SSV substrate with various void sizes, with *d* = 0.1. The lines show theoretically calculated values for Bragg plasmons, taken from [50].

This angular dependence is clearly shown in Figure 1-9, which shows the white light reflectance spectra of four SSV substrates of equal normalized film height but varying sphere size. The plasmons actually consist of several factors, all of which shift with changing incident angle. The minor component is red-shifted as the incident angle is increased, but the major component in most cases (the 500 nm case being a notable exception) is blue-shifted with increasing angle of incidence.

1.7.2. Mie plasmons

The spherical voids themselves generate another type of plasmon, the Mie plasmon. It is thought this is the major factor in SERS from SSV substrates. The plasmons for a perfectly sealed void in an infinite Au medium can be calculated [50, 51], and take a rather similar form to molecular orbitals (see Figure 1-10), which are known as Mie modes (l=1, 2 etc…).

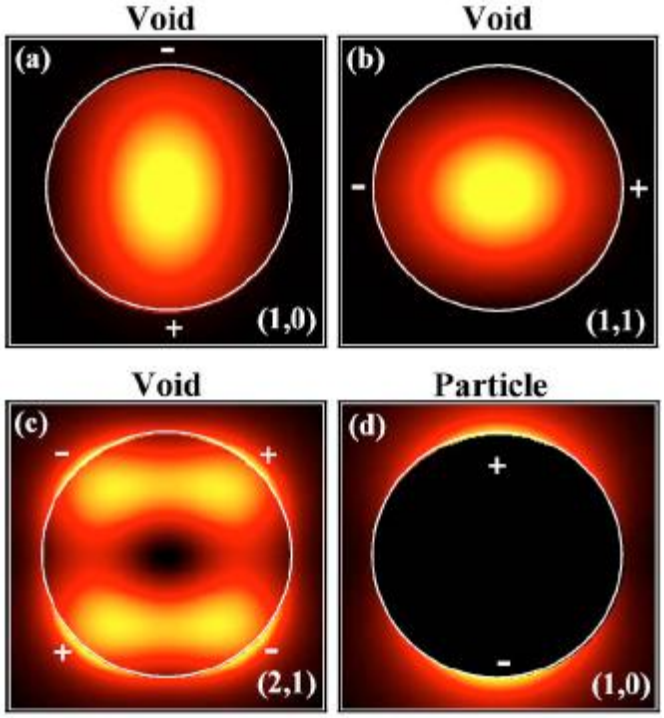

Figure 1-10 – Mie plasmon modes for a fully encapsulated void in an infinite Au medium, taken from [50].

Whereas on a nanoparticle the plasmon is located around the poles, in the case of a void the plasmon is found in the centre, with the strongest intensity relatively far away from the surface of the metal. In reality the voids are truncated; and the best solution for a truncated void is to treat the plasmons as a standing wave that propagates in the void, reflected off the rim. A one dimensional wave vector, k_{swp}, can be calculated by:

$$k_{swp} = p\frac{2\pi}{y} = \frac{\pi p}{\cos^{-1}(1-2d)}$$

Equation 14

where p is an integer of half wavelengths that will fit into a rim-to-rim distance, y, (see Figure 1-11).

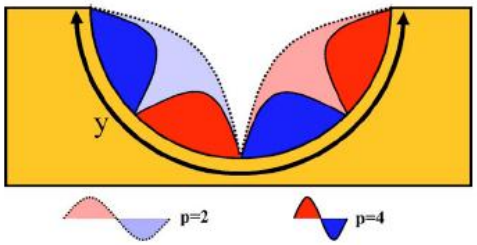

Figure 1-11 – Schematic of standing wave plasmon inside a void on a SSV substrate, taken from [50]

In this case, the energy of the plasmon can be calculated using a similar method than for the Bragg plasmons (see Equation 13):

$$E = \hbar c k_{swp} \sqrt{\epsilon_d^{-1} + \epsilon_m^{-1}(E)}$$

Equation 15

where, as before, ϵ_d and ϵ_m are the dielectric constants for the surrounding medium and the metal, respectively. In this case, the energy of the plasmon is dependant solely on the wave vector, which in turn is dependant on the mode being probed and the circumference of the void. This can be seen from reflectance spectra of a graded sample (see Figure 1-12).

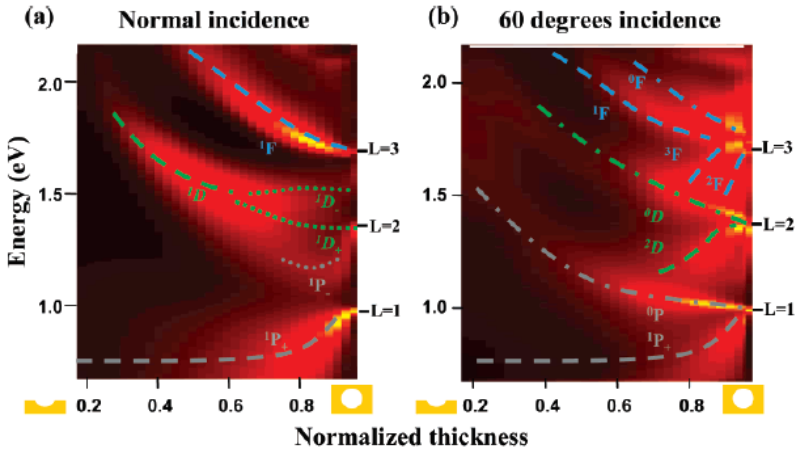

Figure 1-12 – Reflectance spectra of a graded sample with increasing thickness at (a) normal incidence and (b) 60° incidence, taken from [51]

The various Mie modes of P, D and F correspond to L = 1, 2 and 3 (and p = 2, 3, and 4 respectively). The exact shapes and energies of various modes are shown in Figure 1-13. Unless otherwise stated, the work in this thesis uses substrates of d =

0.75 and normal incidence, with a 633 nm (1.96 eV). This means that a combination of ^{1}D and ^{1}F Mie modes will be used.

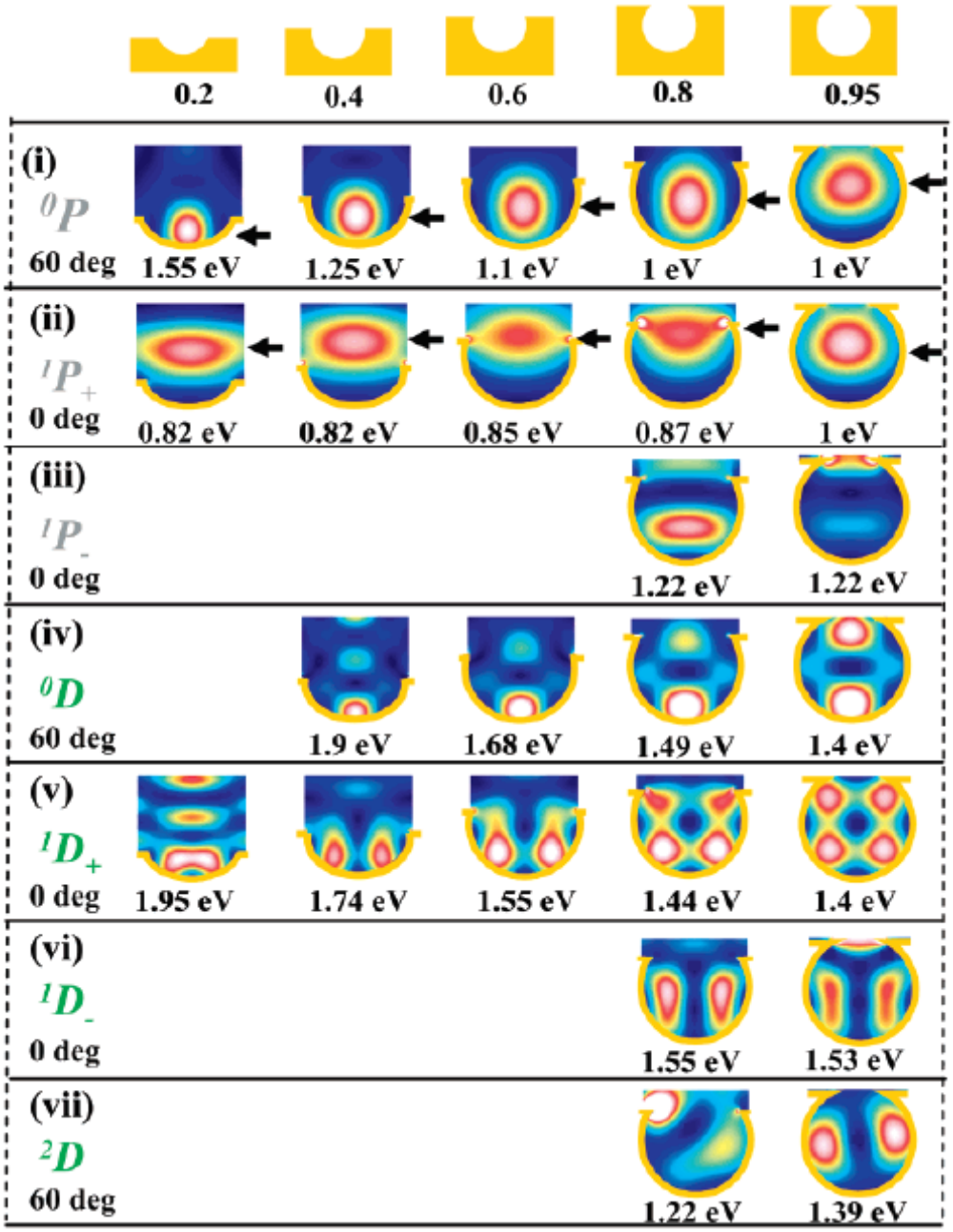

Figure 1-13 – Calculated Mie modes and their energies for increasing values of L and *d*, taken from [51].

At very thin film heights ($d < 0.2$), the Bragg plasmons are much more dominant than the Mie plasmons. At film heights of $0.4 < d < 0.6$ the Bragg plasmons will have almost disappeared (as the sections between the voids at this height are very small). But at film heights of $d > 0.6$ both plasmons are important simultaneously, and a degree of plasmon mixing (or hybridization) occurs.

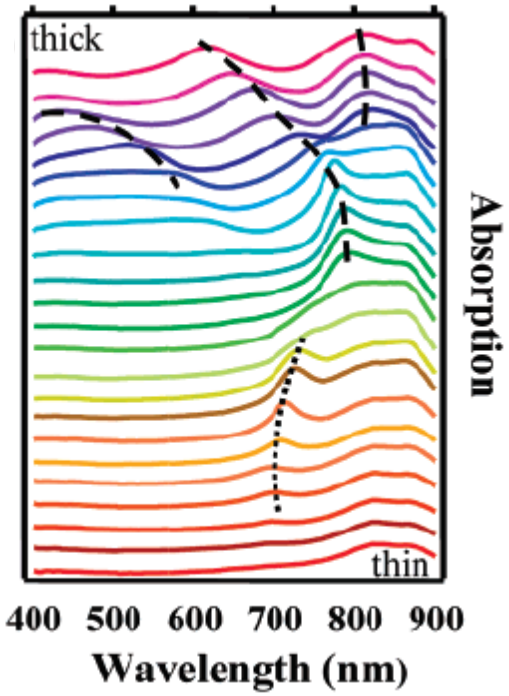

Figure 1-14 – Reflectivity of a graded sample ranging from d = 0.1 (bottom) to d = 0.95 (top). The dotted line represents a Bragg mode and the dashed lines represent the Mie modes, taken from [51].

The growth and shifting of various plasmon modes is illustrated in Figure 1-14, and it can be seen that the Bragg modes are evident at lower film heights and shift very slightly with increasing film heights, until disappearing at ~ d = 0.5. After that, three different Mie modes are seen, and are affected dramatically with increasing film height.

1.7.3. SSV substrates in the literature

SSV substrates make good electrodes for study in spectroelectrochemistry, so it is unsurprising that one of the first uses was to recreate the study of pyridine chemisorption by electrochemistry [15]. In this study a layer of pyridine was chemisorbed to the surface of a 500 nm, 0.75 d Au substrate, and spectrum acquired at various potentials in 0.1 M KCl and 50 mM pyridine solution. The spectra followed similar patterns to those reported for pyridine on silver [3], with the majority of desorption occurring between -0.6 and -0.8 V vs SCE.

The enhancement for both an ORC roughened and SSV structured Au substrate were calculated (from confocal microscopy), and they were found to be 2.3 x 10^4 and 1.5 x 10^5 respectively. This showed the SSV to yield stronger SERS. Another advantage of an SSV substrate is its tolerance to relatively extreme potentials. Roughened substrates are intolerant of highly cathodic potentials, resulting in an

irreversible loss in SERS intensity. However, after cycling to potentials as low as -1.6 V vs SCE, the SSV substrate still showed strong SERS enhancements.

One of the major benefits of electrochemical deposition coupled with nanosphere lithography is that any metal can be used to create a substrate, (whereas only a limited few can be used for evaporation). One of the metals of considerable interest to the electrochemical community is Pt, as it is a highly active electrocatalyst, and so the ability to study reactions on a Pt surface is desirable. In 2007, Abdelsalam *et al* [17] reported both Pt and Pd SSV substrates, showing strong SERS. They noted that the maximum enhancements always occur when $0.7 < d < 0.9$, (whilst on Au the greatest enhancement could occur for $d = 0.5$). The enhancement factors for the substrates were 1800 for Pd and 550 for Pt. These are lower than other reported Pt group nanostructures, but with the benefit of being uniform enhancements across the surface (unlike other current Pt group structures, which depend on hotspots).

Moreover, Pd substrates have recently shown an enhancement in UV excited SERS [18]. When using very small voids (200 nm) and film heights of $d = 0.3$, the SER spectrum of adenine adsorbed on a Pd SSV substrate gave an enhancement factor of 150 with an excitation source of 325 nm. The benefits of UV SERS are much lower fluorescence, higher spatial resolution, and in the case of organic adsorbates, a much higher chance of the resonance with the excitation laser, resulting in much lower detection limits.

1.8. Research aims and thesis overview

In this thesis the previous work on SSV substrates [52] was built upon to achieve an even greater understanding of their capabilities and limitations. This thesis focuses on simple modifications that can be made to the substrate to customize it for a variety of different environments.

The techniques, equipment, chemicals and methods used to create and subsequently modify the surfaces will be given in Chapter 2. A detailed description of the Raman spectrometer used in this work will be also be given, as well as information on the optical methods used.

There are a number of processes that can be investigated by SERS, and a handful of these will be discussed in Chapter 3. SERS of organic films adsorbed onto an SSV

substrate will be observed as well as spectroelectrochemical probing of a CO coated Pt surface. The distance dependence of the SERS enhancement will be investigated through variable lengths of DNA and SERS markers.

Chapter 4 will focus on surface modification of the Au bulk with ultra thin films of other metals through under potential deposition. The change in both SERS spectrum and intensity will be discussed, and compared to so-called "borrowed SERS" [26, 36, 53] techniques.

Chapter 5 will investigate the adsorption of metallic nanoparticles onto an SSV surface and observe further SERS enhancement than with the substrate alone. The strength and nature of the enhancement will be determined, and any possible tuning of the localised electromagnetic field to perform specific tasks.

By combining the results from the preceding chapters in this thesis, Chapter 6 will focus on using overlayers and substrate-particle nanolenses to probe chemical environments.

Finally, conclusions and suggestions of further work will be present in Chapter 7.

1.9.References

1. C. V. Raman and K. S. Krishnan, *Indian Journal of Physics*, 1928, 387.
2. E. Smith and G. Dent, *Modern Raman Spectroscopy*, Wiley, 2005.
3. Fleischmann M, Hendra P. J. and McQuillan A. J., *Chemical Physics Letters*, 1974, **26**, 163-166.
4. M. G. Albrecht and J. A. Creighton, *Journal of the American Chemical Society*, 1977, **99**, 5215-5217.
5. D. L. Jeanmaire and R. P. Van Duyne, *Journal of Electroanalytical Chemistry*, 1977, **84**, 1-20.
6. M. Moskovits, *Rev. Mod. Phys.*, 1985, **57**, 783-826.
7. D.-S. Kim, J. Heo, S.-H. Ahn, S. W. Han, W. S. Yun and Z. H. Kim, *Nano Letters*, 2009, **9**, 3619-3625.
8. S. Kawata, Y. Inouye and P. Verma, *Nat. Photonics*, 2009, **3**, 388-394.
9. J. Henzie, J. Lee, M. H. Lee, W. Hasan and T. W. Odom, *Annual Review of Physical Chemistry*, 2009, **60**, 147-165.
10. P. A. Lund, D. E. Tevault and R. R. Smardzewski, *The Journal of Physical Chemistry*, 1984, **88**, 1731-1735.
11. F. Li, Y. Lu, G. Xue and Q. Cao, *Chemical Physics Letters*, 1997, **264**, 376-380.
12. M. Moskovits, D. P. DiLella and K. J. Maynard, *Langmuir*, 1988, **4**, 67-76.
13. S. J. Lee, A. R. Morrill and M. Moskovits, *Journal of the American Chemical Society*, 2006, **128**, 2200-2201.
14. M. Fan and A. G. Brolo, *Physical Chemistry Chemical Physics*, 2009, **11**, 7381-7389.
15. M. E. Abdelsalam, P. N. Bartlett, J. J. Baumberg, S. Cintra, T. A. Kelf and A. E. Russell, *Electrochemistry Communications*, 2005, **7**, 740-744.
16. J.-Z. Zheng, B. Ren, D.-Y. Wu and Z.-Q. Tian, *Journal of Electroanalytical Chemistry*, 2005, **574**, 285-289.
17. M. E. Abdelsalam, S. Mahajan, P. N. Bartlett, J. J. Baumberg and A. E. Russell, *Journal of the American Chemical Society*, 2007, **129**, 7399-7406.
18. L. Cui, S. Mahajan, R. M. Cole, B. Soares, P. N. Bartlett, J. J. Baumberg, I. P. Hayward, B. Ren, A. E. Russell and Z. Q. Tian, *Physical Chemistry Chemical Physics*, 2009, **11**, 1023-1026.

19. B. Ren, X. F. Lin, Z. L. Yang, G. K. Liu, R. F. Aroca, B. W. Mao and Z. Q. Tian, *Journal of the American Chemical Society*, 2003, **125**, 9598-9599.
20. Z. Q. Tian, Z. L. Yang, B. Ren and D. Y. Wu, *Surface-Enhanced Raman Scattering: Physics and Applications*, 2006, **103**, 125-146.
21. Z. L. Yang, D. Y. Wu, B. Ren, H. G. Zhou and Z. Q. Tian, *Spectroscopy and Spectral Analysis*, 2004, **24**, 682-685.
22. A. Otto, *Journal of Raman Spectroscopy*, 2005, **36**, 497-509.
23. Y. Xie, D. Y. Wu, G. K. Liu, Z. F. Huang, B. Ren, J. W. Yan, Z. L. Yang and Z. Q. Tian, *Journal of Electroanalytical Chemistry*, 2003, **554-555**, 417-425.
24. T. Luczak, M. BeltowskaBrzezinska, M. Bron and R. Holze, *Vibrational Spectroscopy*, 1997, **15**, 17-25.
25. X. Gao, Y. Zhang and M. J. Weaver, *Langmuir*, 1992, **8**, 668-672.
26. S. Zou and M. J. Weaver, *Analytical Chemistry*, 1998, **70**, 2387-2395.
27. H. Luo and M. J. Weaver, *Langmuir*, 1999, **15**, 8743-8749.
28. M. F. Mrozek, S. A. Wasileski and M. J. Weaver, *Journal of the American Chemical Society*, 2001, **123**, 12817-12825.
29. M. F. Mrozek and M. J. Weaver, *Journal of Physical Chemistry B*, 2001, **105**, 8931-8937.
30. M. F. Mrozek and M. J. Weaver, *Analytical Chemistry*, 2002, **74**, 4069-4075.
31. J. J. Laserna, *Analytica Chimica Acta*, 1993, **283**, 607-622.
32. T. E. Barber, M. S. List, J. W. Haas and E. A. Wachter, *Appl. Spectrosc.*, 1994, **48**, 1423-1427.
33. Z. Q. Tian, B. Ren and D. Y. Wu, *Journal of Physical Chemistry B*, 2002, **106**, 9463-9483.
34. F. Ni and T. M. Cotton, *Analytical Chemistry*, 1986, **58**, 3159-3163.
35. T. Shegai, A. Vaskevich, I. Rubinstein and G. Haran, *Journal of the American Chemical Society*, 2009, **131**, 14390-14398.
36. S. Park, P. X. Yang, P. Corredor and M. J. Weaver, *Journal of the American Chemical Society*, 2002, **124**, 2428-2429.
37. J. A. Creighton, C. G. Blatchford and M. G. Albrecht, *Journal of the Chemical Society-Faraday Transactions Ii*, 1979, **75**, 790-798.
38. D. S. Wang and M. Kerker, *Physical Review B*, 1981, **24**, 1777.
39. W. E. Smith, *Chemical Society Reviews*, 2008, **37**, 955-964.
40. X. M. Qian and S. M. Nie, *Chemical Society Reviews*, 2008, **37**, 912-920.

41. T. Vo-Dinh, *TrAC Trends in Analytical Chemistry*, 1998, **17**, 557-582.
42. M. J. Banholzer, J. E. Millstone, L. D. Qin and C. A. Mirkin, *Chemical Society Reviews*, 2008, **37**, 885-897.
43. Q. Yu, P. Guan, D. Qin, G. Golden and P. M. Wallace, *Nano Letters*, 2008, **8**, 1923-1928.
44. A. Gopinath, S. V. Boriskina, W. R. Premasiri, L. Ziegler, B. r. M. Reinhard and L. Dal Negro, *Nano Letters*, 2009, **9**, 3922-3929.
45. R. P. Vanduyne, J. C. Hulteen and D. A. Treichel, *Journal of Chemical Physics*, 1993, **99**, 2101-2115.
46. L. A. Dick, A. D. McFarland, C. L. Haynes and R. P. Van Duyne, *The Journal of Physical Chemistry B*, 2001, **106**, 853-860.
47. T. R. Jensen, M. D. Malinsky, C. L. Haynes and R. P. Van Duyne, *The Journal of Physical Chemistry B*, 2000, **104**, 10549-10556.
48. C. L. Haynes and R. P. Van Duyne, *Journal of Physical Chemistry B*, 2003, **107**, 7426-7433.
49. J. J. Baumberg, T. A. Kelf, Y. Sugawara, S. Cintra, M. E. Abdelsalam, P. N. Bartlett and A. E. Russell, *Nano Letters*, 2005, **5**, 2262-2267.
50. T. A. Kelf, Y. Sugawara, R. M. Cole, J. J. Baumberg, M. E. Abdelsalam, S. Cintra, S. Mahajan, A. E. Russell and P. N. Bartlett, *Physical Review B*, 2006, **74**.
51. R. M. Cole, J. J. Baumberg, F. J. Garcia de Abajo, S. Mahajan, M. Abdelsalam and P. N. Bartlett, *Nano Letters*, 2007, **7**, 2094-2100.
52. S. Cintra, M. E. Abdelsalam, P. N. Bartlett, J. J. Baumberg, T. A. Kelf, Y. Sugawara and A. E. Russell, *Faraday Discussions*, 2006, **132**, 191-199.
53. S. Zou, M. J. Weaver, X. Q. Li, B. Ren and Z. Q. Tian, *The Journal of Physical Chemistry B*, 1999, **103**, 4218-4222.

2. Experimental methods

The experimental procedures described in this chapter are the general methods employed throughout this work. Details provided here relate to general substrate preparation and cleaning as used throughout every chapter. For details regarding specific substrate modifications see Table 2-1.

Table 2-1 – List of section specific experimental details

Experiment	Section	Page
Instrumental optimisation	Instrumental and adsorbate effects	39
Diazonium salt electroreduction	Diazonium salt reduction	48
ORC substrate preparation	Metal Overlayers and borrowed SERS	67
Metal overlayer preparation	Thin film deposition on SSV and ORC substrates	67
Nanoparticle preparation	Ag nanoparticle enhanced SERS	85
Assembly of nanoparticle adduct	Mercaptoaniline	87
Preparation and modification of cis-platin coated nanoparticles	Cis-platin coated NPs	112

2.1. Materials

All aqueous solutions were prepared with deionised water from a commercially available purifying system (Purite) and with a resistivity of 18 MΩcm. The chemicals employed in the course of this study are provided in Table 2-2 and were used without further purification.

Table 2-2 – List of reagents and materials used and their suppliers

Chemical	Supplier
Benzenethiol (BT)	Sigma Aldrich
Concentrated sulphuric acid	Fisher Scientific
Cysteamine hydrochloride	Sigma Aldrich
Dimethyl formamide (DMF)	Sigma Aldrich
Ethanol HPLC grade	Fisher Scientific

Gold plating bath	Metalor, Technic Inc
Gold wire	Agar Scientific
Hexadecyltrimethylammonium bromide (CTAB)	Sigma Aldrich
Hydrogn hexachloroplatinate hydrate	Sigma Aldrich
Isopropanol	Sigma Aldrich
Mercaptoaniline	Sigma Aldrich
Mercaptobenzoic acid	Sigma Aldrich
Nitrogen	BOC Gases
Perchloric acid (70%)	Sigma Aldrich
Polystyrene Spheres (1% wt solution)	Duke Scientific
Potassium chloride	BDH Supplies
Potassium hydroxide	BDH Supplies
Potassium tetrachloroplatinate hydrate	Sigma Aldrich
Pyridine	BDH Supplies
Ruthenium trichloride	Sigma Aldrich
Silver nitrate	Sigma Aldrich
Sodium dodecyl sulfate (SDS)	Fisher Scientific
Sodium perchlorate	Fisher Scientific
Sodium tricitrate hydrate	Fisher Scientific

2.2.Sphere Segment Void substrates

2.2.1. Substrate preparation

The SSV SERS active substrates were prepared using a well established procedure [1-10], detailed as follows.

2.2.1.1. Template assembly

Firstly, a glass microscope slide was coated with layers of chromium (10 nm) and gold (200 nm) by evaporation. The slide was then cleaned by sonication in water and IPA for 30 and 90 min respectively. Early substrates were the immersed in 10 mM ethanolic cysteamine solution for a week. This is firstly to create a more hydrophilic surface of the substrate, (this can be seen as the addition of cysteamine decreases the contact angle of the Au and water from 93° to 35°); secondly the amine group in the adsorbate becomes protonated in aqueous solution resulting in an electrostatic attraction between the surface and the negatively charged polystyrene spheres. Midway through the project a change in the surfactant formula used to stabilise the spheres meant that cysteamine started to have an adverse affect on the template formation, and so this step was dropped.

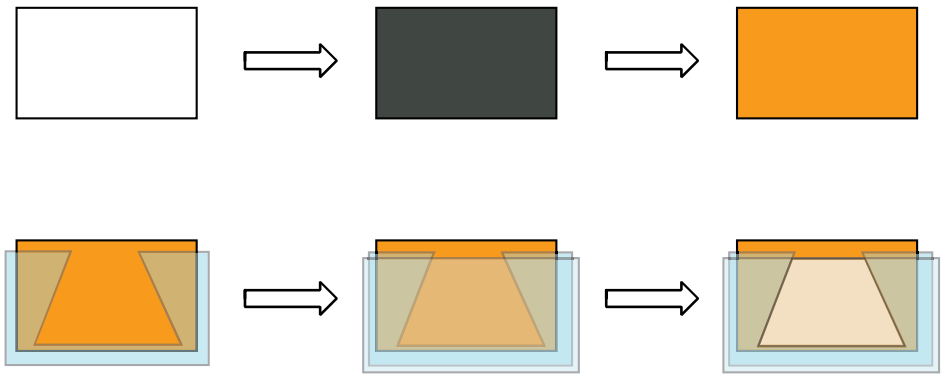

Figure 2-1 - Schematic of the assembly procedure for SERS substrates: i) glass microscope slide, ii) chromium coating, iii) gold coating, iv) parafilm wedge, v) glass cover slip, vi) filled with spheres

A cavity was then created by first placing a template of parafilm onto the surface and a glass coverslip was sealed onto that by heating to ~80 °C. The cavity was then filled with an aqueous suspension of 600 nm diameter polystyrene nanospheres and incubated at 15 °C overnight.

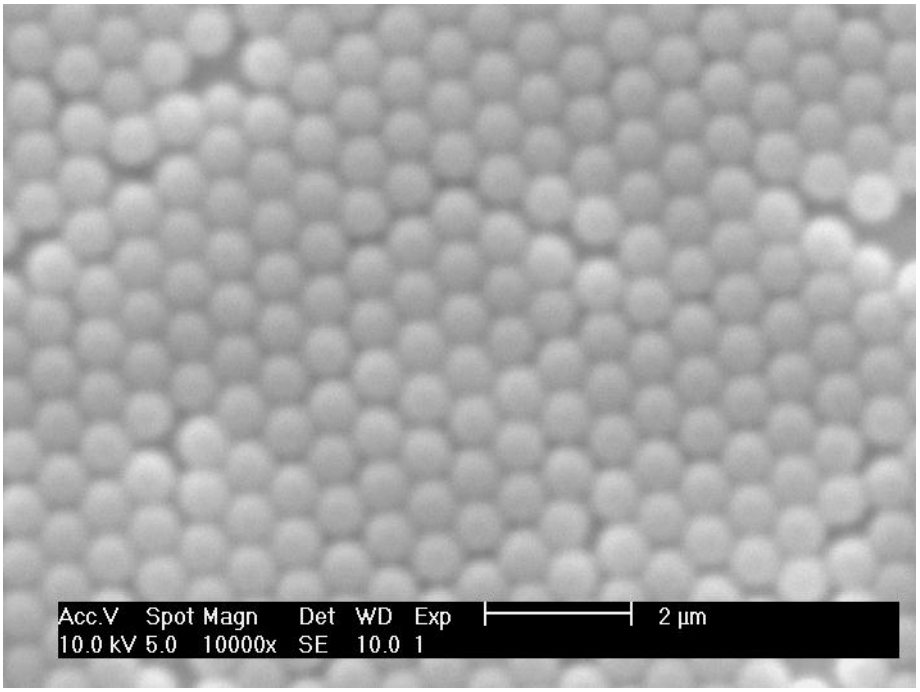

Figure 2-2 – SEM image of 600 nm polystyrene spheres aligned on a Au surface, the spheres have been sputter coated with Au to make them conducting, and the scale bar is 2 µm.

During incubation the water evaporates, causing the spheres to align into a hexagonal array (see Figure 2-2). This is due to attractive capillary forces between the spheres [11] and is shown in Figure 2-3. As the level of water decreases (shown by the red arrow) the spheres are brought closer together until eventually all the water has evaporated and all the spheres have formed a template.

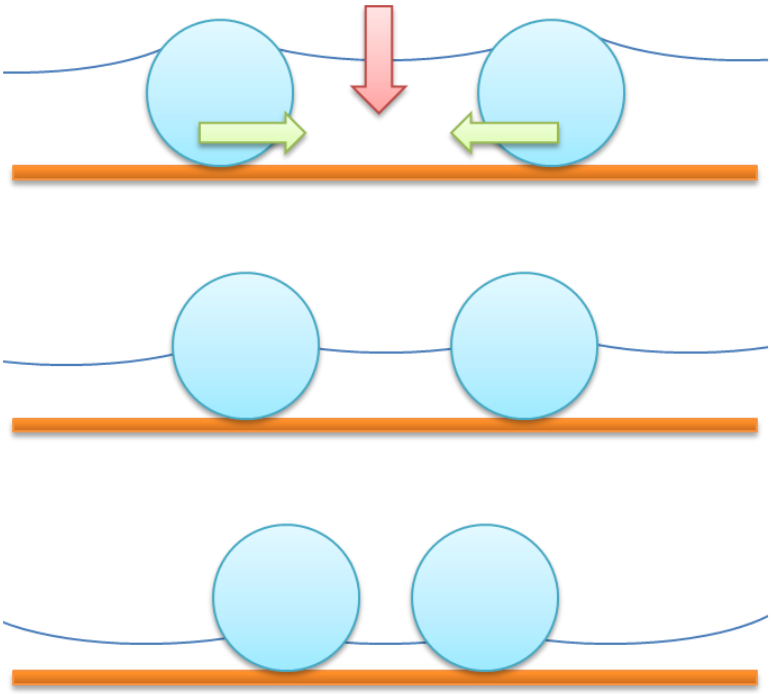

Figure 2-3 – Diagram of attractive capillary forces that drive the formation of the template. The red arrow shows the decreasing level of water (as it evaporates), and the green arrows show the subsequent movement of the spheres towards each other.

After incubation the coverslip was removed by carefully heating to ~60 °C, in order to melt the parafilm whilst leaving the spheres intact.

2.2.1.2. Substrate electrodeposition

The substrates were grown by electrodeposition from a plating bath, (see Table 2-3).

Table 2-3 – Electrodeposition conditions for SSV plating

Metal	**Plating bath**	**Deposition potential**	**Charge needed for 0.75 *d* template**
Au	Metalor gold plating solution, plus 5 mL brightener per 1 L plating solution	-0.70 V vs SCE	0.225 C cm^{-2}
Pt	5 mM H_2PtCl_6 & 50 mM SDS	0.05 V vs SCE	0.180 C cm^{-2}

All electrochemical modification and deposition of the substrates was performed using a custom-made setup shown in Figure 2-4, consisting of a stage that allows control of the height of the template with a 10 µm resolution, a Pt gauze counter electrode and a reference electrode (unless stated otherwise SCE).

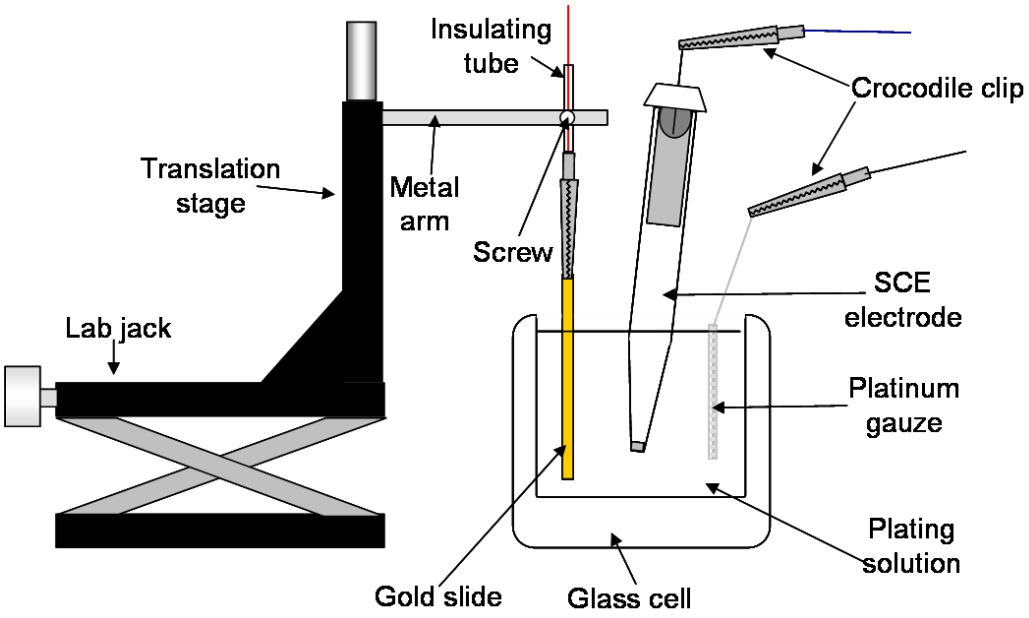

Figure 2-4 – Diagram of the electrochemical cell and stage used for substrate fabrication and modification

Deposition was performed using chronoamperometry. The technique involves applying the desired potential in one instant "potential step" and the current-time response is collected and measured. Control over the film height of the substrate was achieved by depositing at a constant potential, and specifying a cutoff charge. This charge was calculated using Faraday's equation:

$$Q = \frac{m}{nF}$$

Equation 2-1

where Q is the required charge in Coulombs, m is the number of moles deposited, n is the number of electrons involved in the process, and F is Farady's constant.

By taking into consideration the thickness of the deposit and density of the metal, the following equation can be derived:

$$Q = \frac{nFADT}{M_w}$$

Equation 2-2

where D is the density of the metal, A is the area to be deposited, T is the film thickness and M_w is the molecular weight of the metal. For Au deposition a 100% efficiency is assumed, as was established in previous work [9].

The current transient for deposition (see Figure 2-5) shows three distinctive regions.

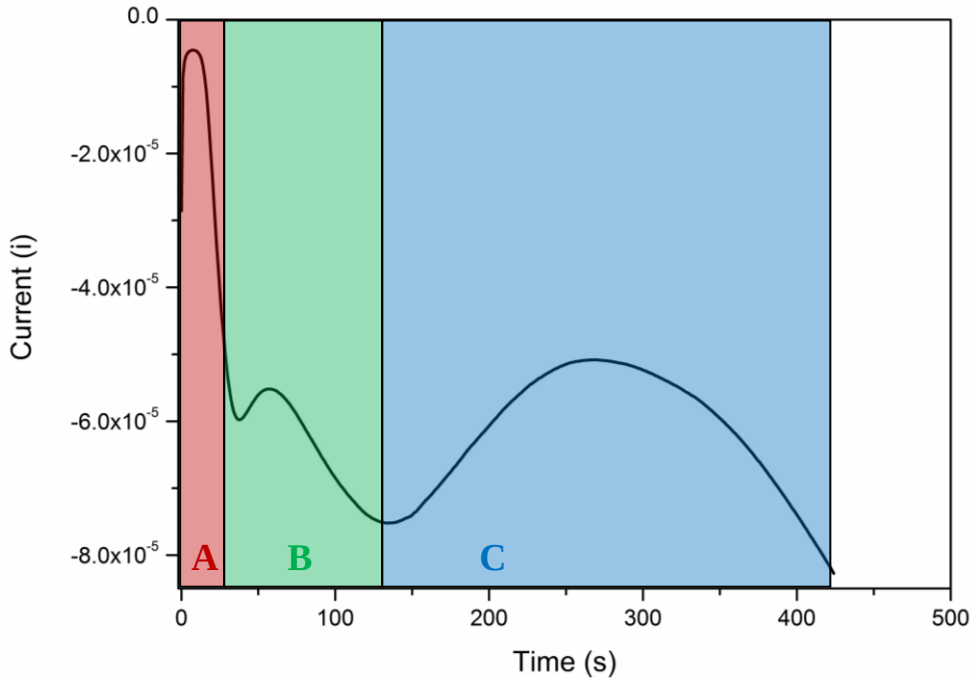

Figure 2-5 – Current-time transient for electrodeposition of a 600 nm 0.75 *d* SSV substrate deposited at -0.72 V vs SCE.

The first region, (A), shows monolayer formation with instant nucleation, and relates to the very first layer of metal deposition. The second region, (B), shows the first few layers of deposition, before the shape of the spheres becomes important and starts to dominate the transient. The final region, (C), shows the bulk of the deposition with a current proportional to surface area of the exposed layer of the substrate. As the film height grows to 0.5 *d*, the amount of exposed surface decreases, resulting in a drop in current (shown on Figure 2-5 at ~275 s) before an increase in current as the surface area starts to increase again. Further work on electrodeposition through three dimensional sphere systems has been reported by Szamocki *et al* [12].

The result is a metal film containing a periodic hexagonal array of spheres, which are then removed by dissolution in DMF, leaving a substrate consisting of sphere segment voids. Finally, the morphology of the substrate was checked with electron microscopy.

Unless otherwise stated, analytes were adsorbed onto the substrate by soaking in a 10 mM ethanolic or aqueous solution overnight. The substrate was then rinsed with the relevant solvent and dried under nitrogen.

2.2.2. Scanning Electron Microscopy

All the substrates were analysed by scanning electron microscopy (SEM) to ensure the structure obtained matched the desired form (see Figure 2-6), however it is beyond the scope of this thesis to explain the inner workings of electron microscopy.

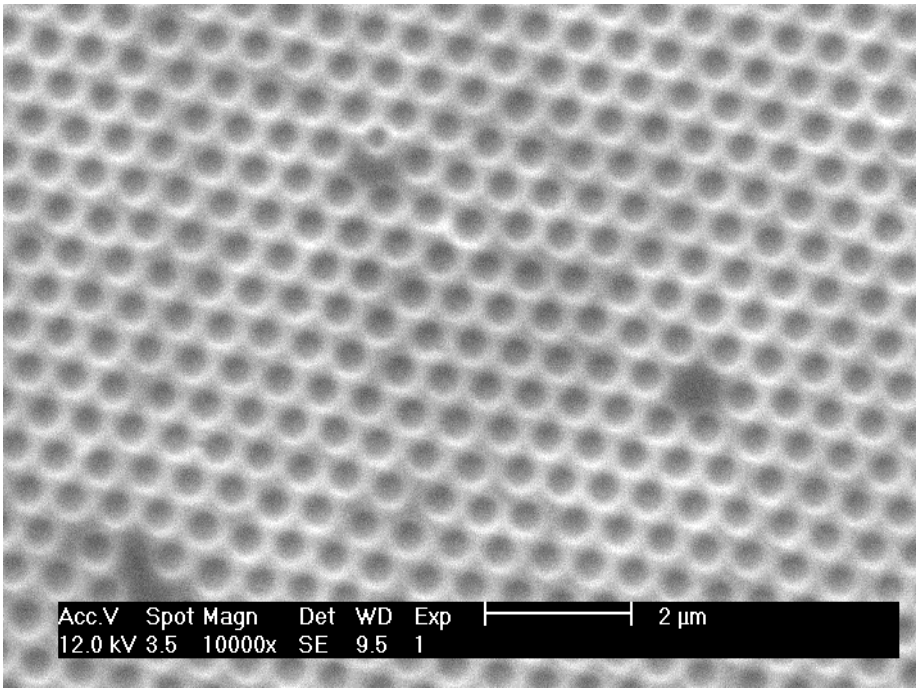

Figure 2-6 – SEM image of a Au SSV showing the regular array of nanovoids with only limited defects, the scale bar is 2 µm.

The SEM used was a Philips XL30 ESEM in which electrons are accelerated by a tungsten filament source to energies of 15-30 keV, and a spot size of 4 (arbitrary units) was used.

2.2.3. Substrate cleaning

One of the major benefits of a SSV substrate is that they can be used multiple times with minimal degradation. In order to achieve this, the substrate must first be cleaned

to remove any contaminants from previous experiments. Organic adsorbates can be removed by reduction following a simple procedure from Yuan *et al* [13]. The substrate is immersed in 0.5 M $NaBH_4$ dissolved in 1:1 H_2O/EtOH for several hours, then rinsed with ethanol and water before drying under nitrogen. This is a very reliable method for the majority of adsorbates; however certain compounds (such as pyridine or isocyanides) must be removed by electrochemical cleaning.

A substrate can be cleaned electrochemically by cyclic voltammetry in acidic or basic media. During formation and the subsequent stripping of Au oxide any adsorbates are gradually removed, resulting in a clean Au surface. The use of acid (typically 0.1 M H_2SO_4) was found to be too harsh on the structuring of the surface, causing slight damage with repeated cycling, so 0.1 M KOH is used as standard. A typical CV (see Figure 2-7) shows a distinctive peak at 0.2 V on the initial scan, associated with the oxidative removal of an adsorbed species.

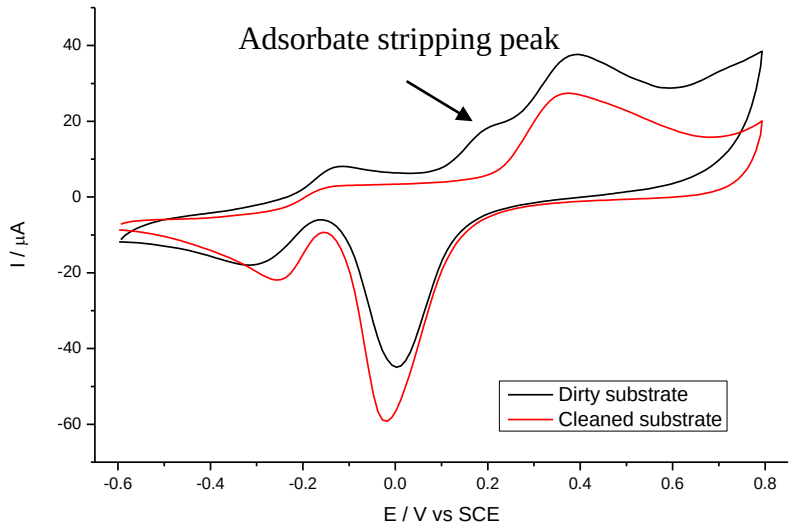

Figure 2-7 – Cyclic voltammogram of a Au 600 nm 0.75 d SSV substrate when dirty and after cleaning, (with 50 cycles) recorded in 0.1 M KOH with a scan rate of 100 mV s^{-1} a Pt gauze counter electrode and a SCE reference electrode.

After cleaning with 50 cycles in the KOH solution the peak at 0.2 V is no longer present, and the area of the Au oxide peak is much larger. This is due to removal of all the adsorbed species and results in a clean electrode surface. It is important to carry out the cleaning in a slow and controlled manner with sweep rates no faster greater than 100 mV s^{-1} as otherwise surface roughening can occur.

2.1.1. Reflectance spectroscopy

Angle resolved reflectance spectroscopy is performed on a custom-built instrument consisting of a computer-controlled goniometer and sample holder that allows for complete control of the incident (θ) and azimuthal (φ) angles of reflection (see Figure 2-8). The source is a supercontinuum white light laser, allowing simultaneous study of the visible through to near infrared region. Unless otherwise stated the samples were monitored at a fixed azimuthal angle and between 0° and 60° angle of incidence.

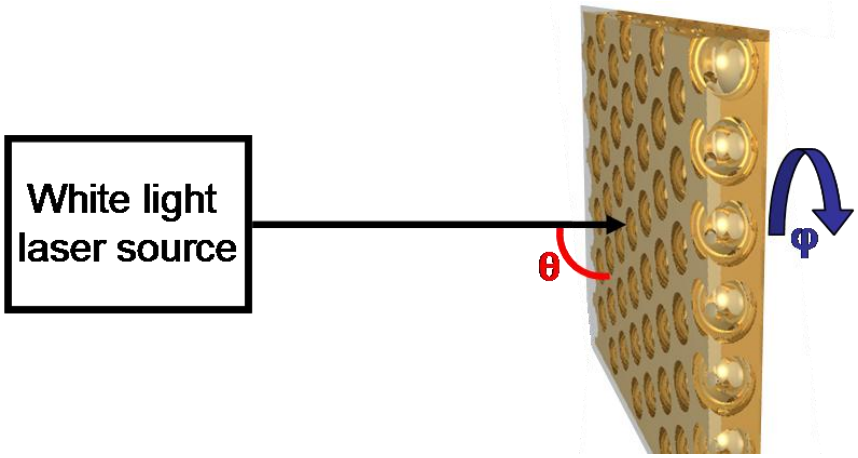

Figure 2-8 – Sample geometry and setup for angle dependant reflectance geometry using supercontinuum white light laser. The laser source irradiates the sample at a user-decided angle of incidence (θ) and azimuth (φ), and the reflected light is collected by a detector.

The light is polarized through filters and its intensity is modified with a neutral density filter before illuminating the sample, and collected by an optical fiber. The light is then passed through a beam-splitter and the spectra recorded by separate optical and infrared spectrometers (Ocean Optics USB2000 and NIR512 respectively).

2.1.2. Raman microscopy

This project makes extensive use of a dispersive Raman spectroscope, working in conjunction with a Leica DMLM series microscope with a variety of interchangeable objectives. A dispersive system differs from a Fourier transform (FT) spectrograph machine in that the FT machine uses an interferometer to detect and display the spectrum, whilst the dispersive spectrometer relies on a grating to disperse the light

into its constituent wavelengths before hitting the detector. A schematic of a dispersive instrument is shown in Figure 2-9.

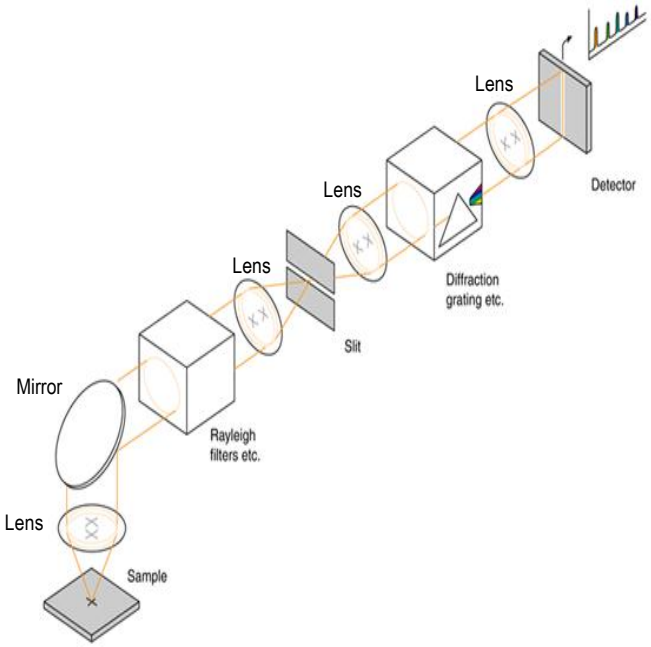

Figure 2-9 – Schematic of the workings of a dispersive spectrometer, the yellow lines show the light pathway through the spectrometer.

The sample is illuminated by a monochromatic light source and the emitted light collected by the internal optics. The Rayleigh light is removed by a filter and the observed wavelengths split using a diffraction grating before being collected on a detector.

The instrument used in this study is a Renishaw 2000 Raman spectrometer, (see Figure 2-10). The laser, (with excitation wavelength of 633 nm) enters the instrument via an adjustable mirror, is fed through a beam expander and directed through the microscope and onto the sample *via* a series of mirrors and a microscope objective. A holographic notch filter with a cut-off of ~ 200 cm^{-1} is used to remove Rayleigh light, and a grating of 1,800 lines/mm is used to disperse the light, before detection with a peltier cooled CCD detector.

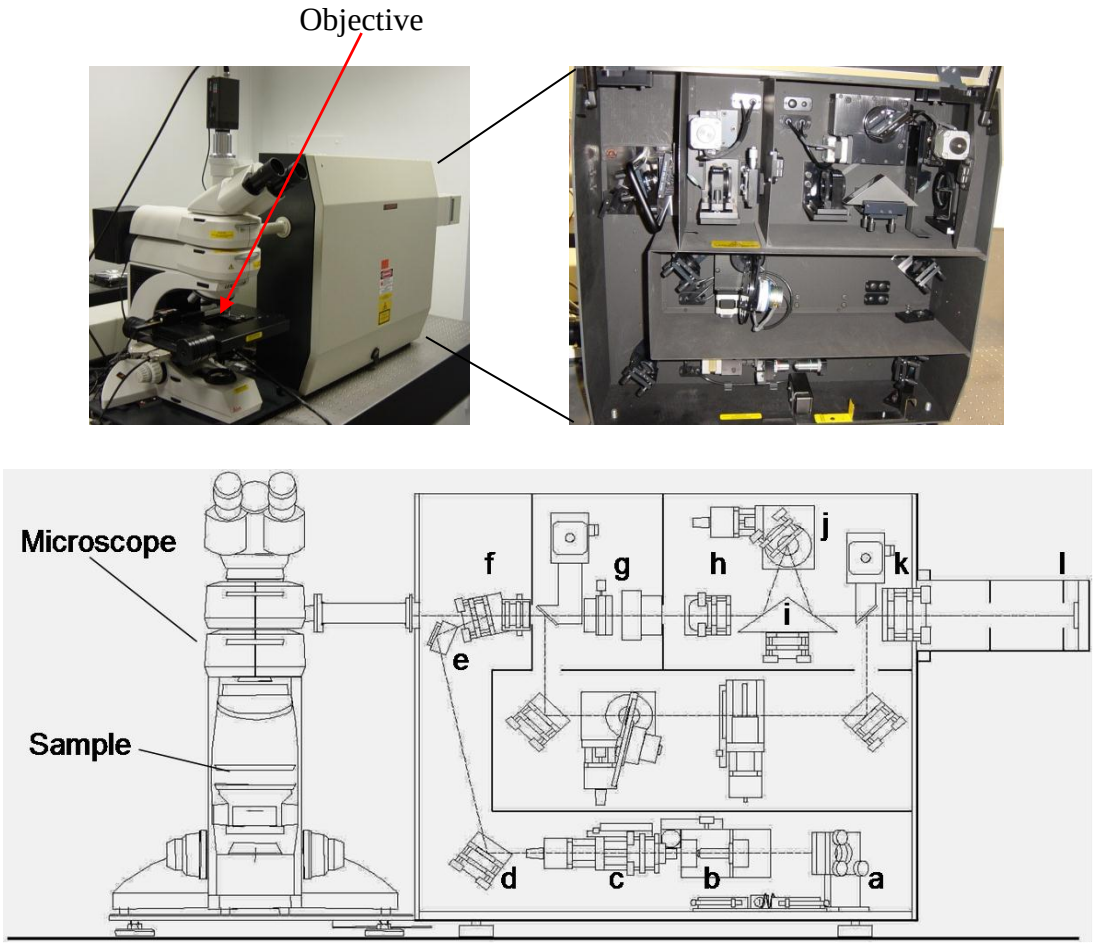

Figure 2-10 - Photograph and schematic of the Renishaw 2000 spectrometer. The components listed are:

a) laser alignment mirror, b+c) beam expander objective, d) adjustable mirror, e) fixed mirror, f) holographic notch filter, g) adjustable spectrographic entrance slit, h) prism lens, i) prism, j) grating, k) CCD focusing lens, l) CCD detector

The area of the CCD is much larger than the area illuminated by the scattered light, so the signal is only collected by a small proportion of the total area of the detector. In older versions of the Renishaw Wire software this is manually selected, whereas in the more modern versions this is controlled automatically. The size of the area chosen to use can be used to change the confocality of the system: if 10 pixels above and below the centre of the crosshair are used then the system is in "standard confocality" mode; if the CCD uses ±2 pixels then it operates in "high confocality". The degree of confocality can be even further enhanced by closing the slit (g) width down to 20 µm when necessary as well.

The Raman microscope is fitted with a variety of objective lenses, the specifications of which are given below (see Table 2-4). Unless otherwise specified, spectra of

dried substrates were collected using the X50 0.75 NA objective and *in situ* spectroelectrochemical spectra the X50 0.55 NA objective.

Table 2-4 – Specifications for objective lenses used with the Raman microscope

Magnification	Numerical aperture (NA)	Working distance/ mm	Relative collection efficiency
X50	0.75	0.37	1
X20	0.40	0.39	0.25
X5	0.12	14.00	0.02
X50	0.55	8.00	0.49

Unless otherwise stated, Raman spectra were averaged over five different spots observed on the same substrate.

2.2.Electrochemistry

All electrochemical measurements were made using computer controlled Autolab potentiostats, namely the μAutolabII and PGSTAT20 models, coupled with GPES software. In all cases a platinum counter electrode was employed, and either saturated calomel (SCE) or mercury-mercury sulphate (MMS) reference electrodes (both of which were homemade).

2.2.1. Spectroelectrochemistry

In situ spectroelectrochemical measurements were performed in a custom built spectroelectrochemical cell (see Figure 2-11) consisting of a Pt ring as a counter electrode, Lugin capillary with a reference electrode, and a mount for the working electrode to be positioned close to the glass window. Electrical contact between the electrode face and the input cable was through a Pt wire touching the surface of the substrate.

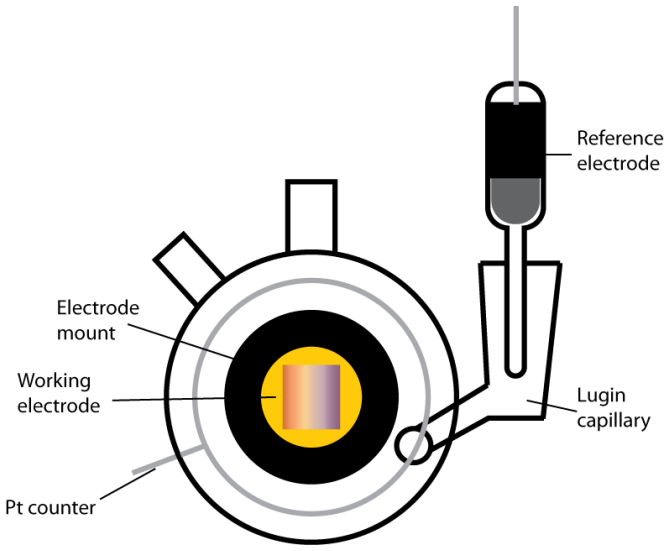

Figure 2-11 – Schematic diagram of spectroelectrochemical cell used for potential dependant SERS

Raman spectra were collected using a macro lens set (Ventacon) which transmits the laser through a 90° angle to allow measurements to be carried out in a horizontal orientation.

Spectroelectrochemical measurements were performed using potential step electrochemistry, where the desired potential was applied and the system allowed to equilibrate for 1 min before Raman spectra were collected.

2.3. References

1. M. E. Abdelsalam, P. N. Bartlett, J. J. Baumberg, S. Cintra, T. A. Kelf and A. E. Russell, *Electrochemistry Communications*, 2005, **7**, 740-744.
2. S. Cintra, M. E. Abdelsalam, P. N. Bartlett, J. J. Baumberg, T. A. Kelf, Y. Sugawara and A. E. Russell, *Faraday Discussions*, 2006, **132**, 191-199.
3. M. E. Abdelsalam, S. Mahajan, P. N. Bartlett, J. J. Baumberg and A. E. Russell, *Journal of the American Chemical Society*, 2007, **129**, 7399-7406.
4. J. J. Baumberg, T. A. Kelf, Y. Sugawara, S. Cintra, M. E. Abdelsalam, P. N. Bartlett and A. E. Russell, *Nano Letters*, 2005, **5**, 2262-2267.
5. R. M. Cole, J. J. Baumberg, F. J. Garcia de Abajo, S. Mahajan, M. Abdelsalam and P. N. Bartlett, *Nano Letters*, 2007, **7**, 2094-2100.

6. T. V. Teperik, F. J. G. de Abajo, A. G. Borisov, M. Abdelsalam, P. N. Bartlett, Y. Sugawara and J. J. Baumberg, *Nature Photonics*, 2008, **2**, 299-301.
7. L. Cui, S. Mahajan, R. M. Cole, B. Soares, P. N. Bartlett, J. J. Baumberg, I. P. Hayward, B. Ren, A. E. Russell and Z. Q. Tian, *Physical Chemistry Chemical Physics*, 2009, **11**, 1023-1026.
8. T. A. Kelf, Y. Sugawara, R. M. Cole, J. J. Baumberg, M. E. Abdelsalam, S. Cintra, S. Mahajan, A. E. Russell and P. N. Bartlett, *Physical Review B*, 2006, **74**.
9. S. H. Pelfrey, University of Southampton, 2008.
10. S. Mahajan, University of Southampton, 2008.
11. P. A. Kralchevsky and N. D. Denkov, *Current Opinion in Colloid & Interface Science*, 2001, **6**, 383-401.
12. R. Szamocki, S. Reculusa, S. Ravaine, P. N. Bartlett, A. Kuhn and R. Hempelmann, *Angewandte Chemie International Edition*, 2006, **45**, 1317-1321.
13. M. Yuan, S. Zhan, X. Zhou, Y. Liu, L. Feng, Y. Lin, Z. Zhang and J. Hu, *Langmuir*, 2008, **24**, 8707-8710.

3. Instrumental and adsorbate effects

3.1. Introduction

This project studies SSV substrates in a variety of different physical and chemical environments, using a number of techniques. To fully understand and interpret the results obtained it is important that any effects from the instrumentation itself is recorded and taken into consideration.

When obtaining the vibrational spectra of bulk, amorphous samples with a non-polarised light source, there is very little effect from sample orientation, and hence no angular dependence [1]. The use of a SERS substrate, however, changes this as plasmon modes show high levels of angular dependence. Recently reported work by McLellan *et al.* [2] showed that the intensity of Ag nanocube-enhanced spectra varies with the orientation of the incident radiation with respect to the cube. If the polarisation of the laser runs along the corner-to-corner axis of the cube then the spectra are strong. If the polarisation runs along the face-to-face axis of the cube, then spectrum is weaker, especially at higher frequencies. This effect decreased as the particles became more spherical.

Similar effects have also been observed on other nanostructured substrates, as is shown in the case of Ag nanorods reported by Liu *et al.* [3]. The intensity of absorbed trans-1,2-bis(4-pyridyl) ethene was plotted as a function of the incident angle of the excitation laser. The enhancement was found to increase steadily to a maximum of 45°, before dropping off quickly at higher angles.

An angular dependence is also evident on SSV substrates and previous results [4] have shown that the intensity of the spectrum of adsorbed benzenethiol (BT) varies significantly (for a fixed void size, film height and excitation wavelength) as a function of the angle of incidence of the pump and collection angle. For example, on a 900 nm 0.5 *d* Au SSV substrate with 760 nm excitation wavelength set at a fixed pump angle of 16°, the maximum peak counts occurred between 18° and 40° collection angle, which is in agreement with the position of plasmonic absorption of the substrate from a reflectance map.

3.2. Objective dependence

The spectra in this study were collected using a Renishaw 2000 spectrometer with a Leica DMLM series microscope. Whilst the internal aspects of the spectrometer remained constant for all experiments, the objectives used to illuminate the sample (and subsequently gather emitted radiation) were changed for different experiments. Each objective has its own numerical aperture, which in turn leads to a unique depth of field and spot size. The numerical aperture (NA) is simply a function of cone angle [5], and is represented as:

$$NA = nsin(\theta)$$

Equation 3-1

where n is the refractive index of the medium between the objective and the sample, and θ is half the angular aperture of the objective, (or the angle of illumination). A general trend is that the larger the magnification, the larger the NA (and the shorter the working distance). Larger NAs also lead to shallower depths of field, as shown by:

$$d \propto \frac{\lambda n}{NA^2} + \frac{n}{M \times NA}$$

Equation 3-2

where *d* is the depth of field, λ is the wavelength of light, and *M* is the magnification. This means that whilst objectives with high magnification offer large NAs, (and hence better collection efficiencies), the depth of field is smaller. In practice, this equates to objectives with higher NAs yielding better spectra, but lower NAs offering more flexibility with experimental conditions.

Table 3-1 – Numerical apertures, angles of illumination and relative collection efficiency for the objectives used in this study SWD and LWD stand for short and long working distances respectively

Objective	Numerical aperture	Angle of illumination (θ/°)	Collection efficiency	Max intensity of peak at 1571 cm^{-1}
X50 SWD	0.75	49	1	107
X50 LWD	0.55	33	0.49	64
X20	0.40	24	0.25	77
X5	0.12	7	0.02	22

The objectives used in this study are listed along with their NA, angle of illumination, and collection efficiency in Table 3-1. The difference in collection angle between the maximum (X50 SWD - 49°) and minimum (X5 - 7°) is large, and will have a significant effect on the accessible plasmon modes. This can be represented graphically, and is shown in Figure 3-1. The plasmon mode at 1.85 eV is strongly attenuated at higher angles of incidence, and the absorption is strongest between 0° and 15°.

The X5 objective has the benefit of a longer working distance of 14 mm, and its small aperture (see Table 3-1) means that is has a larger depth of field, both of which are useful for spectroelectrochemical measurements. However, the small angle of illumination means that the objective is not well matched to the substrate as much of the plasmon mode at 1.85 eV is excluded. The other three objectives all encompass the strongest part of the plasmon mode, but the X50 short working distance objective (with a NA of 0.75) is the only one to capture the entirety of the mode.

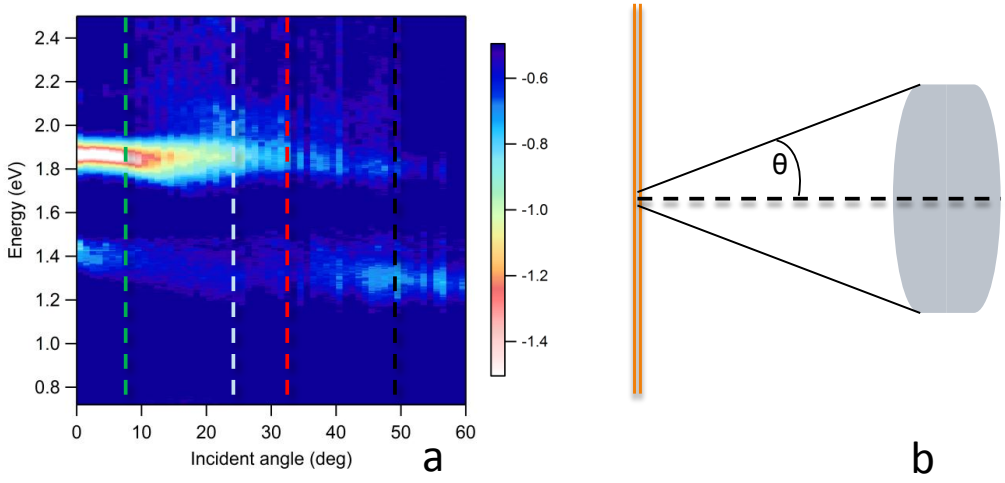

Figure 3-1 – (a) Reflectance map for 600 nm 0.75 *d* Au SSV substrate with an adsorbed layer of mercaptoaniline, and the illumination angles , defined as θ in (b) for objectives of numerical aperture of 0.12, 0.4, 0.55 and 0.75.

The practical applications of variable collection angles was determined by obtaining the SERS spectrum of BT adsorbed on a 600 nm 0.75 *d* Au SSV substrate with identical collection times, and normalizing the spectra to the stated collection efficiency of the objectives (provided by the manufacturer). The spectra are shown in Figure 3-2, and clearly show the expected trend of decreasing counts with smaller NA.

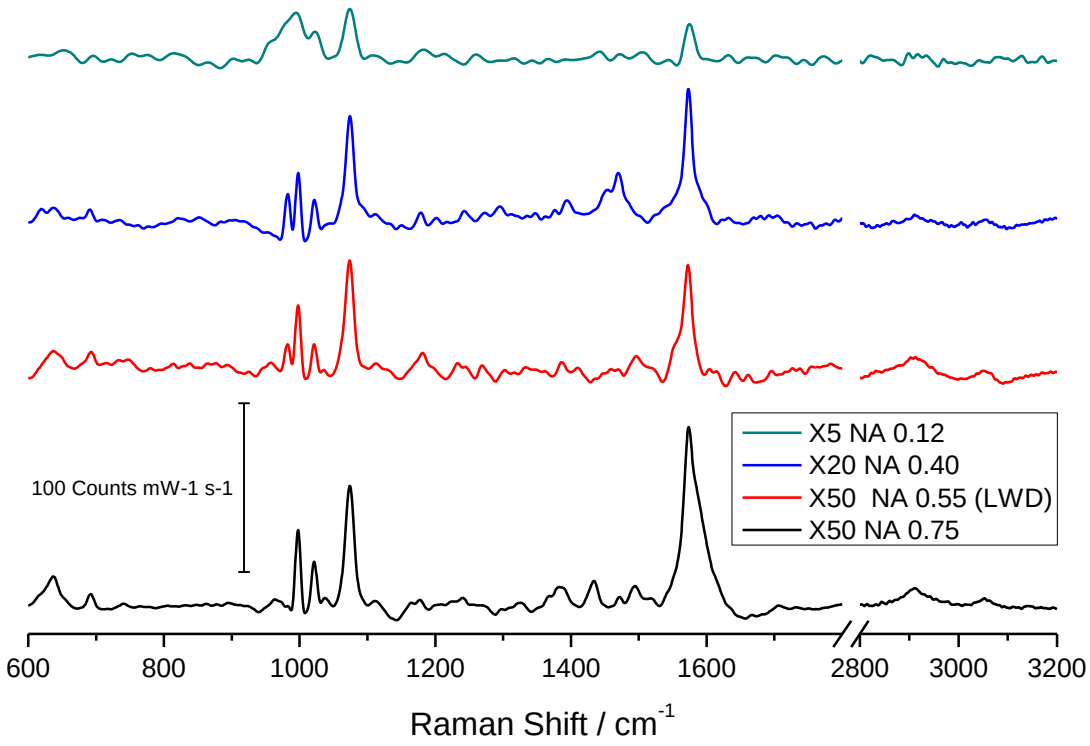

Figure 3-2 – SERS spectra of benzenethiol on a 600 nm 0.75 *d* Au SSV substrate taken with a 633 nm HeNe laser with a power of 3 mW and an accumulation time of 10 s. The objective magnification and corresponding numerical aperture are displayed in the legend, and the spectra have been normalized to the collection efficiencies of the objectives.

A full assignment [6] is given in Table 3-2. There is very little difference between the spectra from the objectives with NA 0.75, 0.55 and 0.40, but given that the corresponding θ values encompass most if not all of the plasmonic absorption, this is expected. The only major difference lies in the *ν*(C-H) modes, between 2800 and 3200 cm^{-1}, which are noticeably smaller in the 0.40 NA spectrum. At higher angles of incidence the plasmon mode is slightly broader, allowing the coupling of higher frequencies of outgoing radiation (such as *ν*(C-H) modes). The 0.40 NA objective does not encompass this section, and so the higher frequency region is lower in intensity. This is demonstrated even further with 0.12 NA objective, where the high frequency region is all but disappeared. The major ring breathing modes are still evident, however they are significantly lower in intensity. In this case even less of the plasmon mode is captured by the objective, and so the efficiency of enhancement is consequently lower.

Table 3-2 – Peak assignments for benzenethiol

Peak centre / cm^{-1}	Assignment
420	ν(M-S)
694	ν(C-S)
740	γ(C-H)
999	12
1023	18a
1072	1
1571	8a
2927	ν_{as}(C-H)
3056	ν_{s}(C-H)

As mentioned above, practical aspects of spectroelectrochemical measurements require the use of the X5 objective, as it has a very long working distance, and large depth of field. Figure 3-1 shows that if the objective is aligned with normal incidence to the sample, then only a small amount of the plasmonic absorption accessed. Through manipulation of the illumination angles (see Figure 3-3) it may be possible to achieve an optimal alignment that offers the largest enhancement.

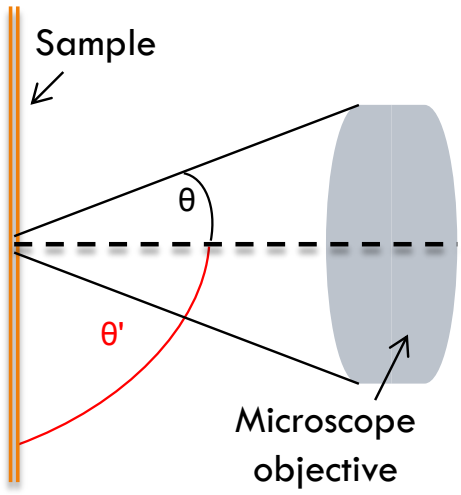

Figure 3-3 – Schematic of experimental setup for angular dependent SERS using a X5 objective with NA of 0.12. θ is the cone angle determined by the NA of the objective, whilst θ' is the angle between the objective and the sample

The experimental system illustrated above allows the fixed illumination and collection angle to be effectively shifted across the plasmon map, and to see how this affects the intensity obtained SERS spectra. Figure 3-4 shows which areas of plasmonic absorption are available for values of θ' between 0° and 45°.

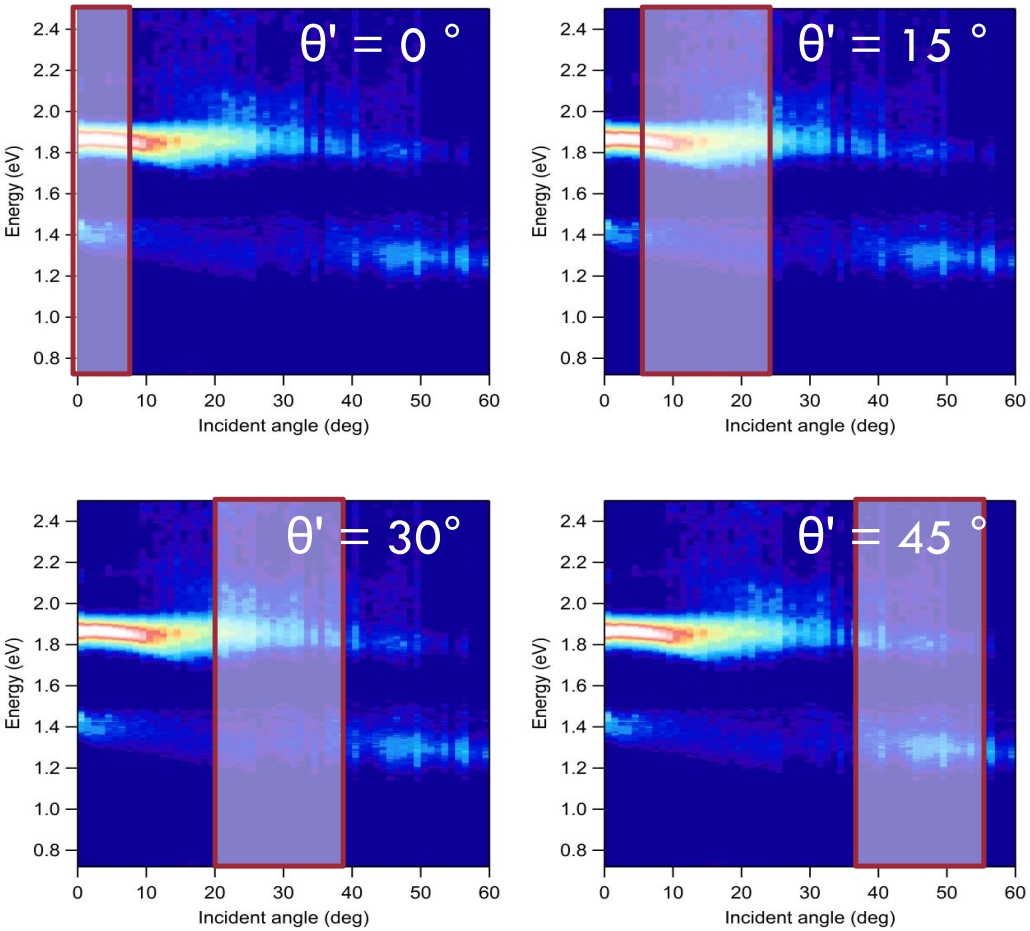

Figure 3-4 – Annotated reflectance maps to show the angles covered by the X5 objective at various angles of incidence

The corresponding spectra (see Figure 3-5) show a general decrease in intensity with increasing angle of incidence. There is minimal change from 0° to 15°, which can be explained by retention of the overlap with the maximum of the plasmonic absorption. There is a decrease in intensity when the angle is changed to 30°, and a notable decrease at 45°. This is again explained by the fact that the strength of the absorption decreases with increasing angle, and at 45° very little overlap with the plasmon mode remains.

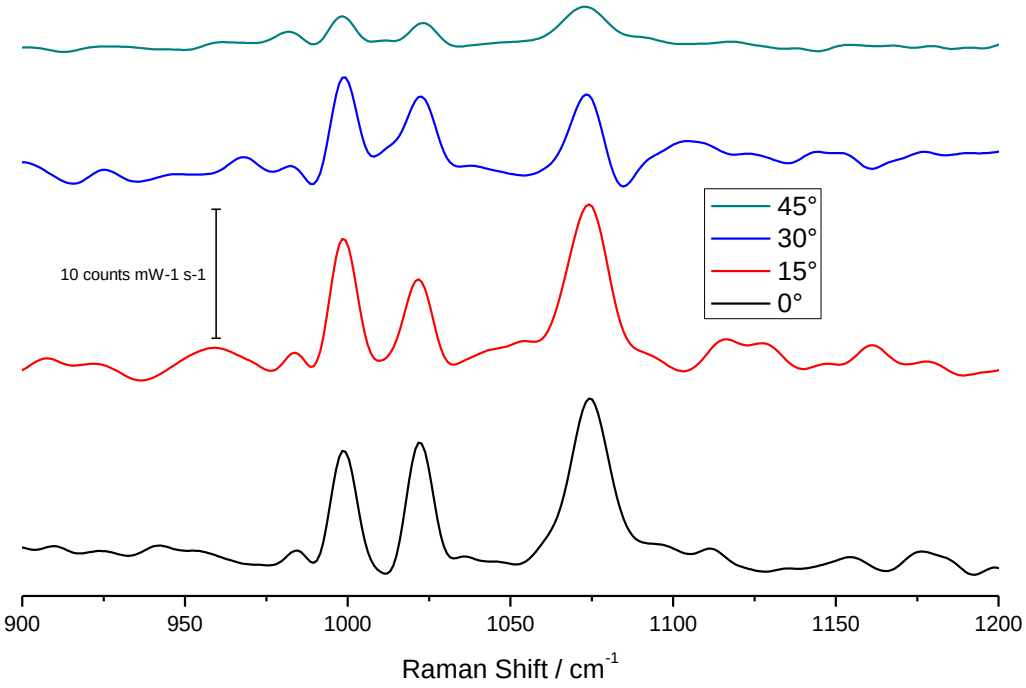

Figure 3-5 – SERS spectra of benzenethiol on a 600 nm 0.75 *d* Au SSV substrate taken with a 633 nm HeNe laser with a power of 3 mW and an accumulation time of 60 s and a X5 objective. The angle of incidence was increased in 15° steps and the spectrum taken at each step.

As mentioned above, previous research on SSV substrates [4] has shown that the outgoing radiation (Rayleigh and Raman scattered light) has an optimum collection angle (as well as incoming radiation's optimum illumination angle). This may explain why the band at 1075 cm^{-1} is larger in the 15° spectrum than the 0°. If that particular arrangement includes both the optimal incoming and outgoing angles then the intensity of the spectrum will be greater than if only one of the angles is covered. It is worth noting that whilst these results do further confirm that the plasmonic absorption is responsible for the SERS enhancement, the fact that the data obtained at 30° still showed an acceptable spectrum means that the substrate is fairly forgiving with respect to exactly how much of the absorption is covered by the objective's cone angle. This means that even if the maximum of the plasmonic absorption does not overlay with the incoming laser line (as is the case with modified substrates in Chapter 4), a decent spectrum is still obtainable.

There is no significant overall benefit to a change in experimental angular-setup, and so all subsequent experiments in this project will be performed using normal incidence.

3.3.Effect of adsorbate

3.3.1. Benzenethiol chemisorption

The dependence of the SERS intensity of BT on the film height and void size of SSV substrates has been well documented [6, 7], and so an ideal selection of sphere diameter and film height for further studies may be identified. The ideal substrate dimensions used in this project are 600 nm voids and film height of 0.75 *d* (450 nm) - the reflectance map of which is shown in Figure 3-6a. However little study has been made of the effect an adsorbate has on the plasmonics of an SSV substrate. Reflectance measurements were therefore also obtained after adsorption of a monolayer of mercaptoaniline (which is very similar to benzenethiol with respect to its binding to Au). A change in the plasmonics was observed, as shown in Figure 3-6b.

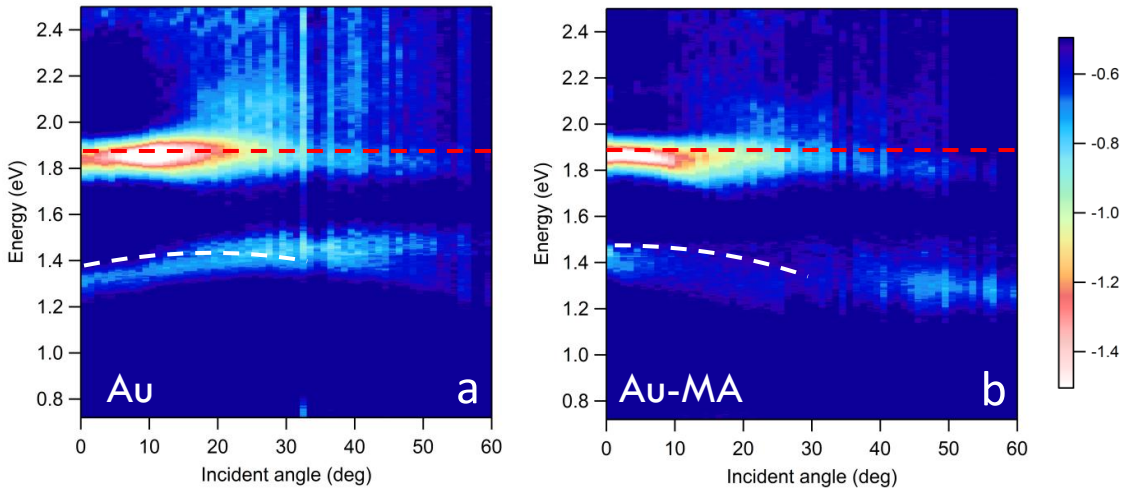

Figure 3-6 – Reflectance maps of 600 nm 0.75 *d* Au SSV substrate (a) with no adsorbate and (b) with a monolayer of mercaptoaniline. The angular dependence of the low energy mode is shown in white and 1.85 eV is shown in red The colour scale shows log(reflectivity).

The change is more clearly seen when the absorption for a single energy is plotted vs angle of incidence (see Figure 3-7, which corresponds to the dotted red lines in Figure 3-6). The maximum centred at 21° in the unmodified substrate is shifted to 15°, the absorption is increased and the mode is sharpened. The second maximum is shifted from 41° to 46° and its intensity is decreased (although it is also sharpened with respect to the unmodified substrate).

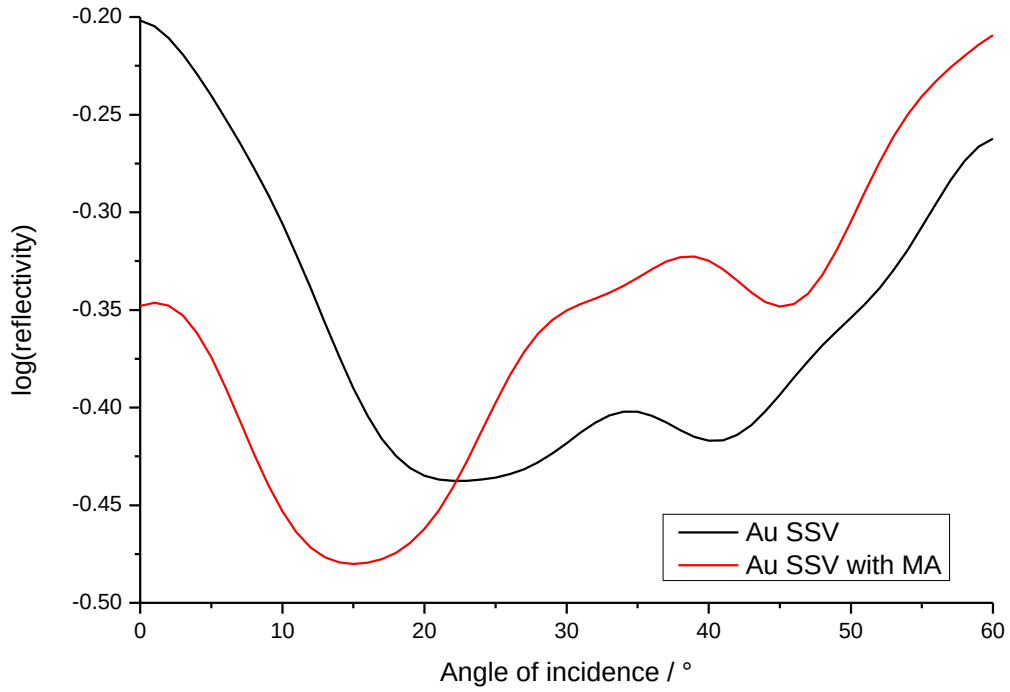

Figure 3-7 – Plot of log(reflectivity) vs angle of incidence for 600 nm 0.75 *d* Au SSV before and after modification with MA taken from the reflectance maps in Figure 3-6 across 1.85 eV

The lower energy mode (starting at 1.3 eV in the Au SSV and 1.4 eV in the Au-MA) is strongly attenuated with the addition of the organic monolayer, with very little absorption between 5° and 42°. The mode also increases in energy with increasing angle of incidence on Au, but moves to lower energy on the Au-MA.

This shift in plasmonics is an example of the strong correlation between localised surface plasmon resonance (LSPR) and the refractive index of the surrounding medium [8-10]. As described in Chapter 1, the energy of the plasmon modes are dependant on the square root of the sum of the dielectric constants of the metal and its surrounding medium. The adsorbate layer has a significantly different dielectric constant to air, and thus the formation of a monolayer on the surface causes a shift in plasmon modes.

3.3.2. Diazonium salt reduction

One of the most common ways of forming a monolayer on a Au substrate is through self-assembly of organic thiols [11-15]. This is a very facile and effective technique, and has been used extensively throughout this project. However the monolayers are susceptible to oxidative removal [16, 17]. A possible alternative to thiol adsorption is through reduction of a Boc protected diazonium salt (DS) in acetonitrile [18, 19].

The cleaned Au electrode is immersed in a mixture of 3 mM 4-(*N*-Boc-aminomethyl)benzene diazonium tetrafluoroborate salt in acetonitrile with 0.1 M tetrabutylammonium tetrafluoroborate and the potential swept from 0.6 to -1.2 V vs Ag/AgCl (see Figure 3-8). With each subsequent scan the negative current decreases as the coverage of the molecule approaches 100%.

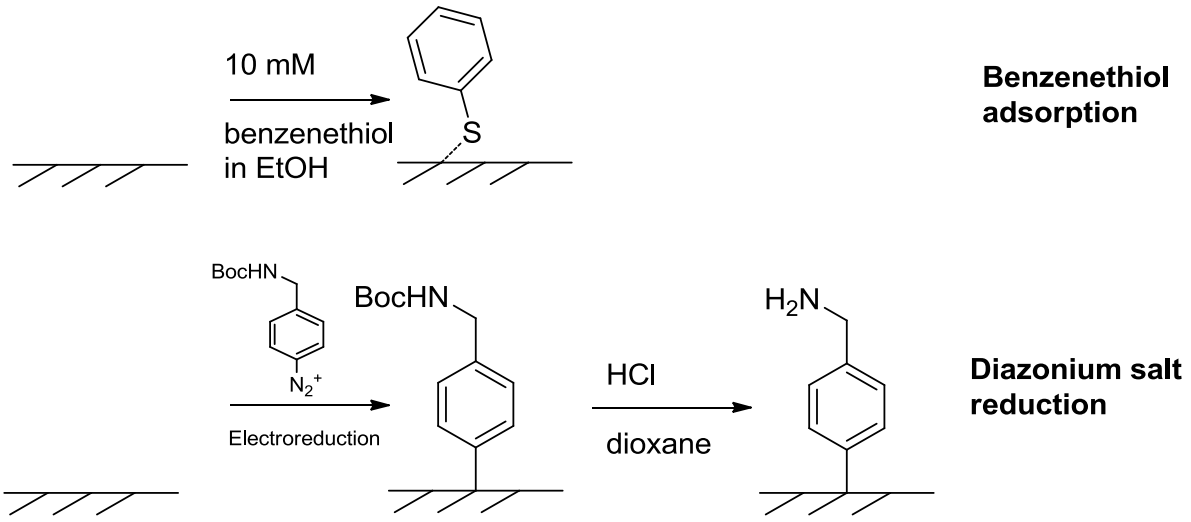

Figure 3-8 – Reaction scheme for benzenethiol adsorption and diazonium salt reduction onto a Au surface

The reflectance map of Au-DS (see Figure 3-9) shows greatly enhanced absorptions over an unmodified or thiol-modified substrate (see Figure 3-6). Both the mixed mode at 1.9 eV and the Mie mode at 1.45 eV (seen at 1.3 eV in the unmodified substrate) have different angular dependencies compared to thiol bound adsorbates.

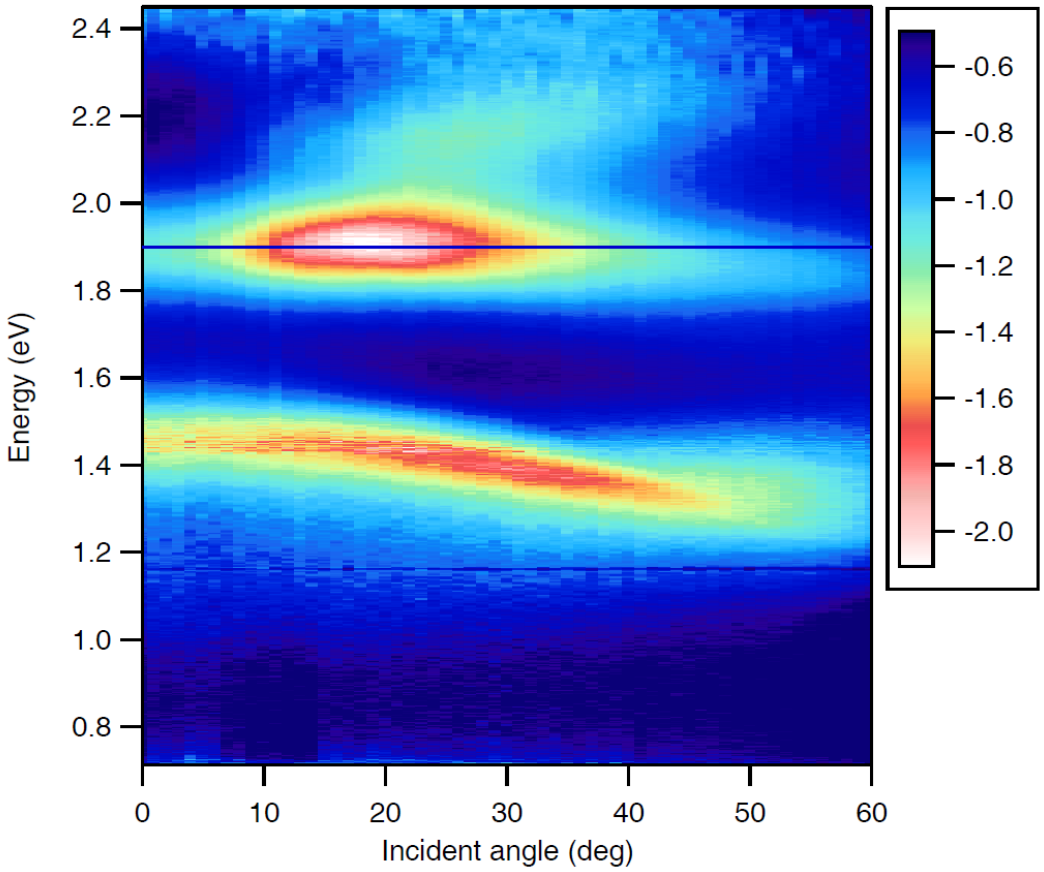

Figure 3-9 – Reflectance map of DS modified Au SSV substrate, the colour scale shows log(reflectivity)

The mixed mode at 1.85 eV shows a much stronger absorption than before, (see Figure 3-10) with an increase from -0.5 to -2.1. The characteristic double-maximum seen in the absorptions in Figure 3-7 is also missing, showing a greater angular dependence, which suggests that the Mie portion of the mixed mode is the dominant factor.

The explanation for the increased Mie absorption comes from the fact that thiol adsorption and diazonium salt reduction affect the Au topography differently. It is well known that thiols have a smoothing effect on Au surfaces [20, 21], whereas the mobility of reduced diazonium salts is limited [22] and hence so is their smoothing effect. This smoothing effect may be causing the rim of the voids to become slightly curved in the case of the modified substrate, and indeed this is taken into consideration when calculating the modes inside the void [23].

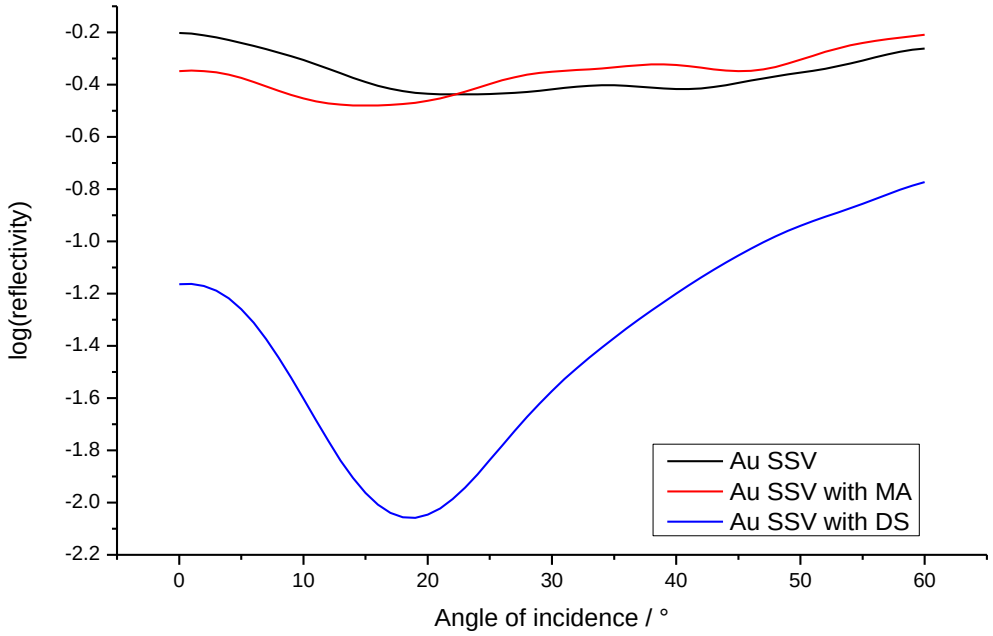

Figure 3-10 – Plot of log(reflectivity) vs angle of incidence for a 600 nm 0.75 *d* Au SSV substrate with no modification, a monolayer of MA and after DS modification for the mode at 1.85 eV, taken from Figure 3-6 and Figure 3-9

Moreover, calculations performed by Calvo *et al.*[22] suggest that the Au-C bond results in a slight perturbation of the Au surface, causing the metal atom to be lifted up slightly from the surface, which could result in a sharpening of the void rim. There is minimal difference to the calculated plasmonics for a curvature of 10 – 100 nm, (which would be expected for a thiol or unmodified substrate), but the DS modified substrate is likely to have a curvature < 10 nm, and therefore a much sharper and stronger Mie mode can be expected, and hence stronger absorption.

With such excellent plasmonics on a DS modified substrate it is expected that the SERS spectrum of the adsorbate would be stronger than BT, but in fact the opposite is seen, as is shown in Figure 3-11.

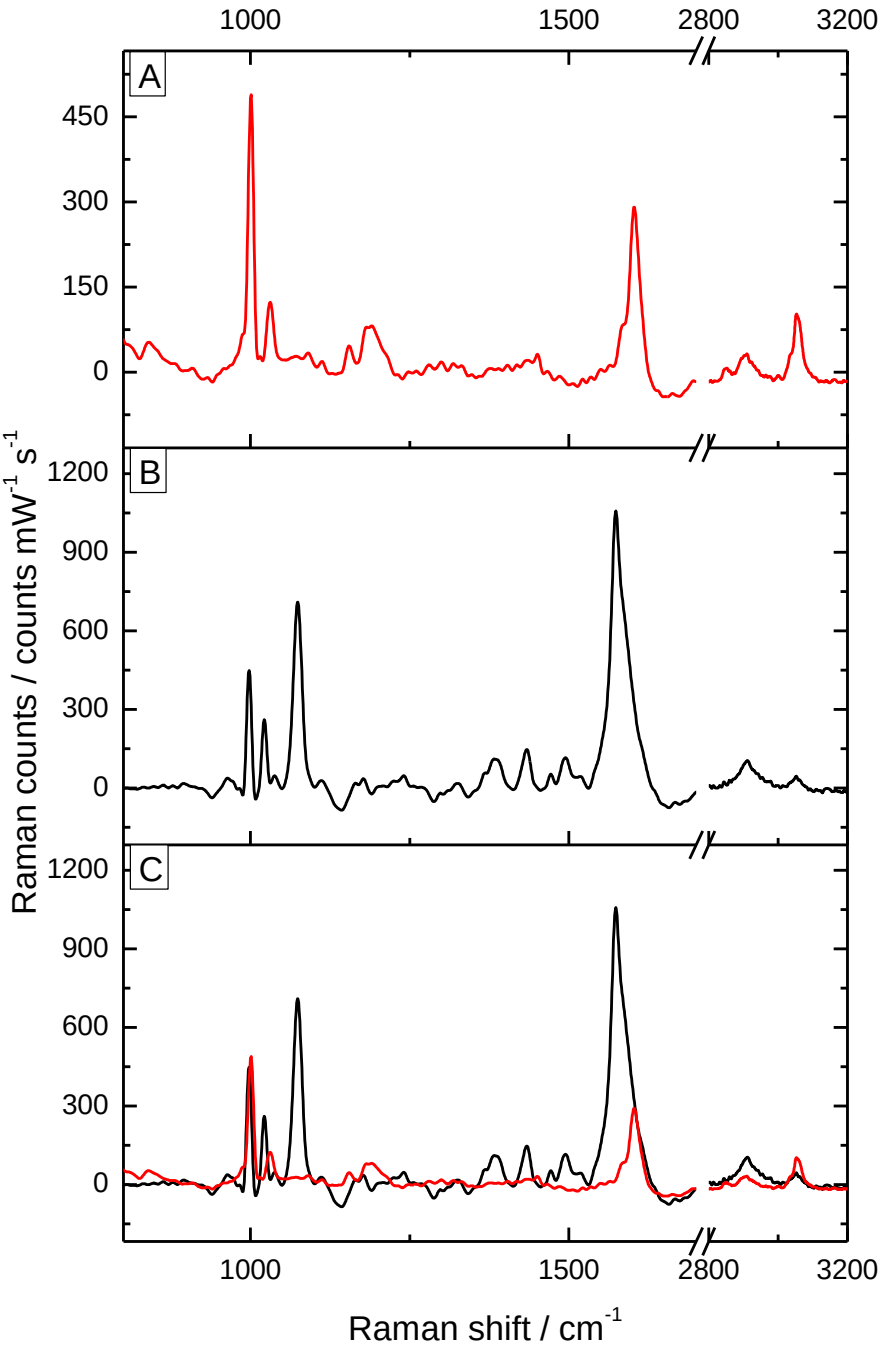

Figure 3-11 – Spectra of (a) DS monolayer and (b) BT and (c) both on the same scale, on a 600 nm 0.75 *d* Au SSV substrate with a 10 s acquisition and a HeNe 633 nm laser at power of 3 mW and a X50 objective.

Whilst two of the peaks corresponding to ring breathing modes (999, 1023 cm^{-1} for the 12 and 18a respectively) are still observed (see Figure 3-11), the band at 1072 cm^{-1} corresponding the 1 mode is not seen. This is caused by constraints placed on the possible vibrations of the ring from the Au-C bond. The 1 mode has A1 symmetry and is the symmetric ring breathing mode. In the case of BT, there are comparatively few geometric constraints, and the ring can stretch and vibrate more

or less independently of the surface, due the thiol spacer. In the DS case, the ring is fixed to the surface directly by the C-Au bond, so most ring breathing modes are physically hindered, whilst completely symmetric modes such as the 1 stretch are not.

The large band at 1576 cm^{-1} is smaller than the other bands again due to constraints from bonding. This corresponds to the 8a mode, which is a whole ring deformation that pivots about the X-C bond. With the thiol spacer of BT this mode occurs without any hindrance, whereas the C-Au bond of the DS layer makes the ring too rigid to undergo this vibration.

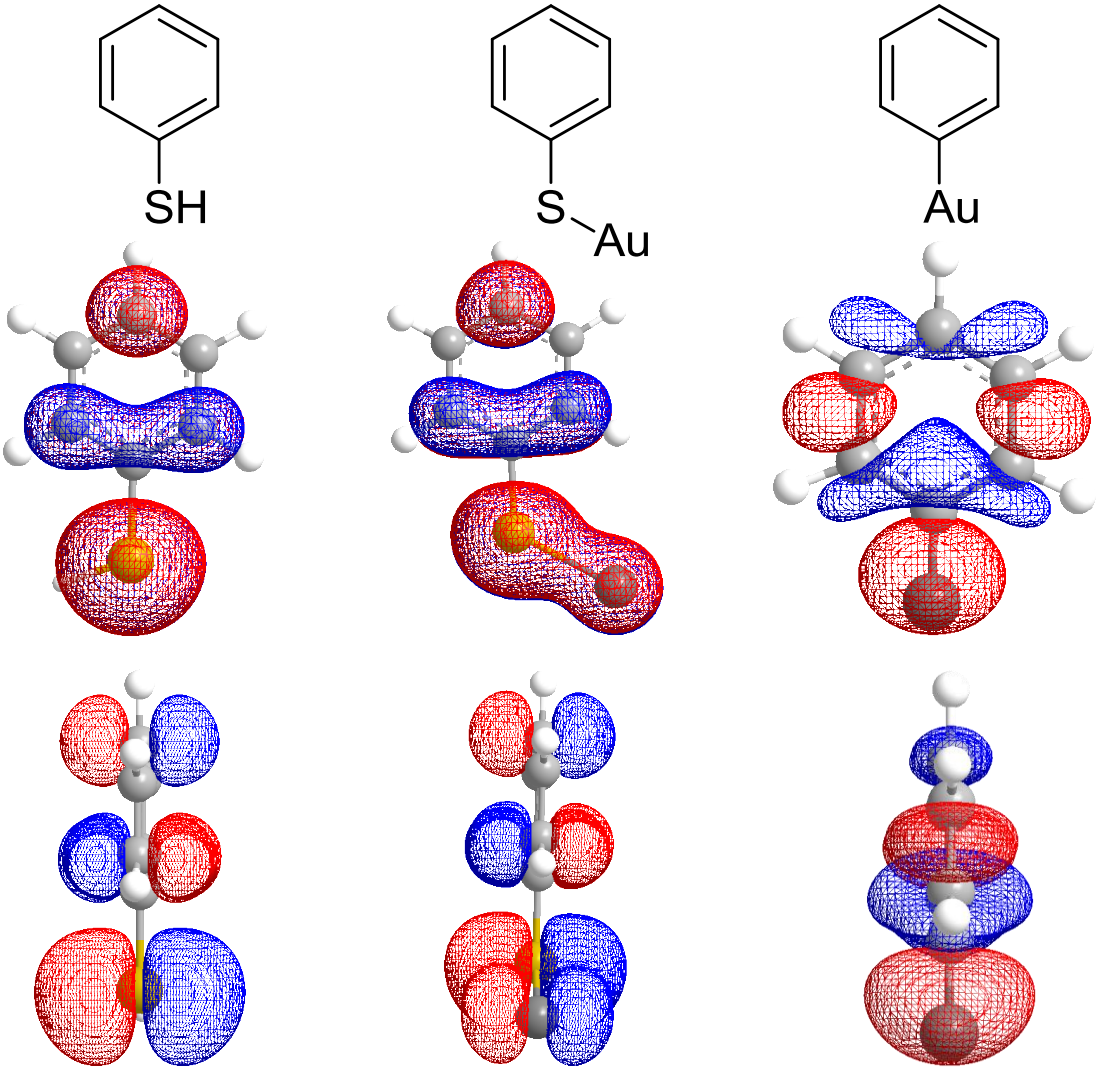

Figure 3-12 – Calculation HOMOs for free and Au bound benzenethiol and DS-Au

The various ring stretching modes in the DS spectrum are much less intense than in BT, whilst the *ν*(C-H) modes are comparable. This can be explained by the effect that the different binding motifs have on the electron density within the ring itself. Calvo *et al.* [22] have thoroughly investigated the difference between C-Au and S-Au bonds on a Au(111) surface, and have shown that the p orbitals of the S atom in BT totally delocalise upon formation of the S-Au bond. For the DS case, however, the C-Au bond does not result in any significant change to the density of states of the p orbital of the C atom, showing no delocalisation.

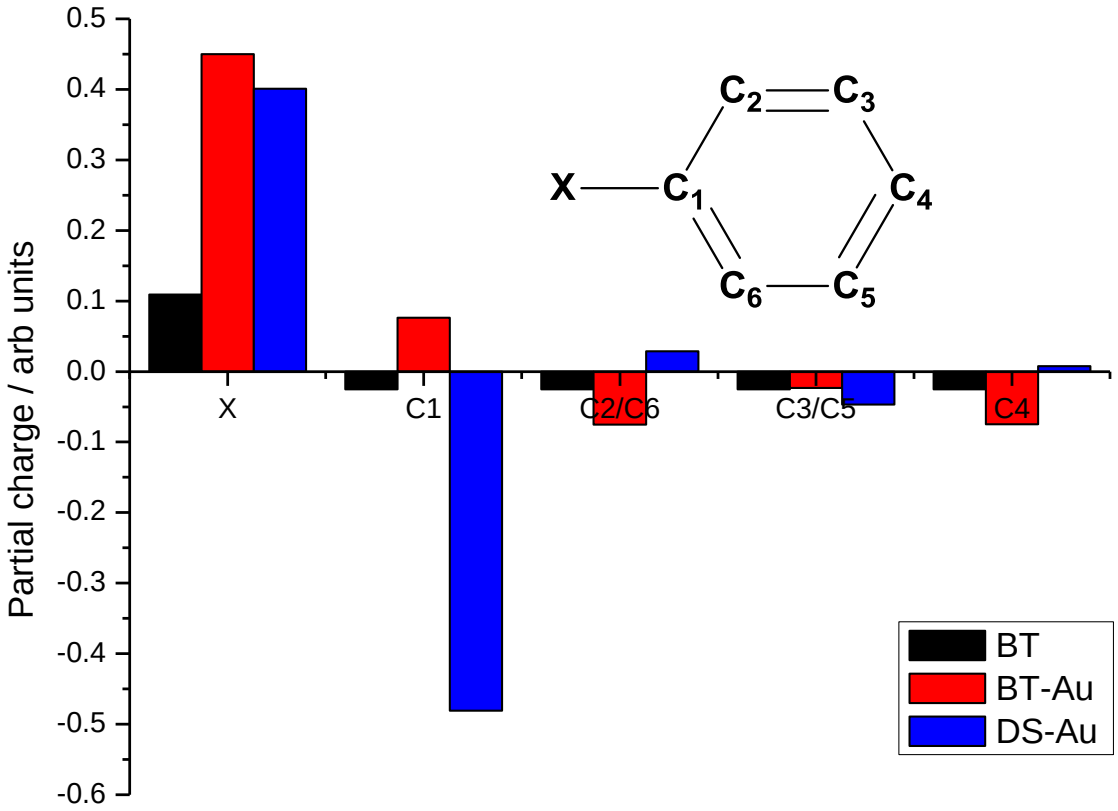

Figure 3-13 – Calculated partial charges for free BT, BT-Au and DS-Au using extended Hückel calculations

Electron density effects also evident in the results for extended Hückel calculations in the CambridgeSoft Chem3D program [24].The HOMO was calculated for free BT, BT-Au and DS-Au (see Figure 3-12). The formation of the Au-S bond results in a extension of the lobe centred on the S atom towards the Au, and corresponds to the delocalisation of the p orbitals also predicted by Calvo *et al.* The formation of the Au-C bond, however, results in a substantial change to the electron density. The π-

cloud above and below the plane of the ring is lost, and a large lobe of density is centred on the C from the Au-C bond.

Again, this increase in electron density is predicted by Calvo *et al.*, who report that the average electron density difference across the molecule is almost three times as great in the Au-C bond than the Au-S equivalent, with a decreased density on the Au atom itself. Partial charge calculations (see Figure 3-13) show that binding BT to a Au atom results in little change to the benzene ring, but positive charge on the S atom, which is a result of the delocalisation of the p orbitals as mentioned above. For the DS case, however, a large negative charge is formed on the C1 atom, resulting in an induced polarisation in the ring, which leads to a strong decrease in spectral intensity.

It is well known that the intensity of a Raman band is proportional to the change in polarisability of the bond, $I \propto \frac{\partial \alpha}{\partial Q}$ [25], and much work has been undertaken to try and understand this phenomenon [26-28]. An investigation into the intensities of ring breathing modes of various substituted benzenes by Schmid *et al.* [29] shows some variation in intensity with differing electron donating or withdrawing properties of the substituent, however they explain this through a change in molecule size.

If the decrease in intensity is caused by lack of polarisability of the C-C bonds within the ring, then in contrast one would expect the *ν*(C-H) bands to be comparatively unchanged, and this is indeed the case (see Figure 3-11). The lack of change in the intensity of bands associated with vibrations far away from the polarisation within the ring confirms that the decrease in ring breathing modes is indeed caused by a lack of polarisability.

3.4.Spectral "background" continuum

Previous work has enabled extensive characterisation of the plasmonic [23, 30] properties of SSV substrates. The optical properties have also been investigated, including studies of the reflectivity of the surface [31], the SERS enhancement [6] and how the SERS background is affected by the choice of adsorbate [32]. The background is a photoluminescent process dependant partially on the plasmonics of the substrate, but also on the adsorbate itself.

The current model for the SSV background (see Figure 3-14) attributes the background response to Raman scattering by the image molecule, (a complimentary, opposite and imaginary form of the charge density of the adsorbate found inside the metal at its surface). During the Raman scattering process the real molecule relaxes to a discreet energy state, resulting in either Rayleigh, Stokes or anti-Stokes scattering, and produces well-defined Raman peaks. The excited image molecule, however, relaxes down to one of a multitude of states in the electronic continuum of the metal surface, and hence a broad band of radiation is emitted, namely the background.

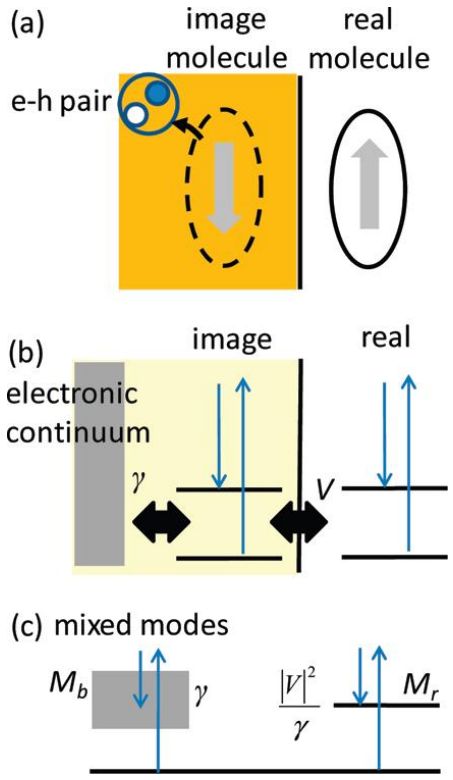

Figure 3-14 – (a) Schematic of the real and image molecules adsorbed on a metal surface; (b) excitation of both the image and real molecules by incident radiation; (c) the image molecule relaxes down into an energy band, whilst the real molecule relaxes to a discreet energy level

Changing the nature of the environment at the surface of the substrate alters the background observed. This may be done by changing the properties of the adsorbate, as different electron withdrawing/donating groups change the intensity of the background. It may also be done by changing the electron density at the surface, as is the case in an electrochemical environment at potentials away from the potential of zero charge.

To determine the potential dependence of the background a Au SSV substrate was soaked in the desired adsorbate overnight before immersing in a spectroelectrochemical cell and using 0.1 M $NaClO_4$ as the electrolyte. The potential was varied with respect to SCE and the spectra acquired.

3.4.1. Electrochemical stripping of benzenethiol

The first system tested was electrochemical stripping of BT, and the spectra are shown in Figure 3-15.

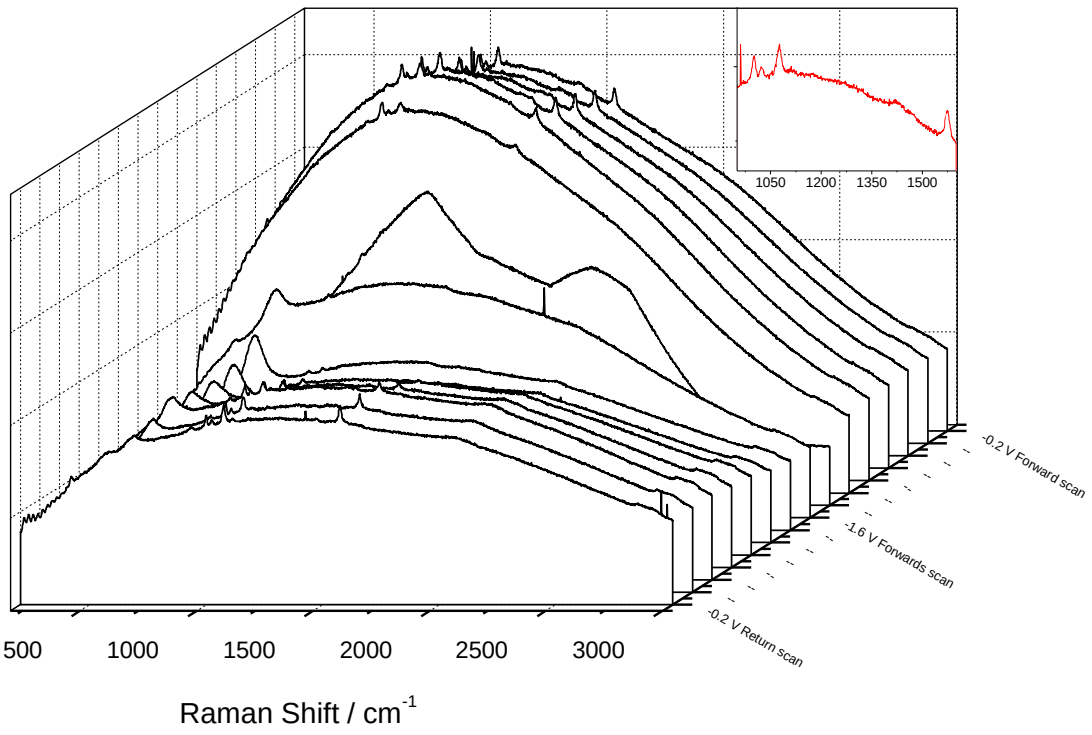

Figure 3-15 – Potential dependant SERS spectra of BT during electrochemical stripping off a Au 600 nm 0.75 *d* SSV substrate in 0.1 M $NaClO_4$. All spectra were obtained with 3 mW HeNe 633 nm laser, a scan time of 10 s and all potentials are reported vs SCE. Spectra were collected between -0.2 and -1.6 V for forward and reverse scans every 0.2 V. Inset shows the spectrum at -0.2 V.

The BT is retained on the surface of the electrode until -1.2 V, at which point it is reductively removed from the surface, which is confirmed by the loss of peaks relating to BT. The intensity of the background decreases drastically with the loss of the adsorbate.

The centre of the background was taken to be 952 cm^{-1}, from a single Gaussian curve fit across an entire spectrum of BT (see Figure 3-16), and all subsequent descriptions of background intensity (for BT) are taken from this point.

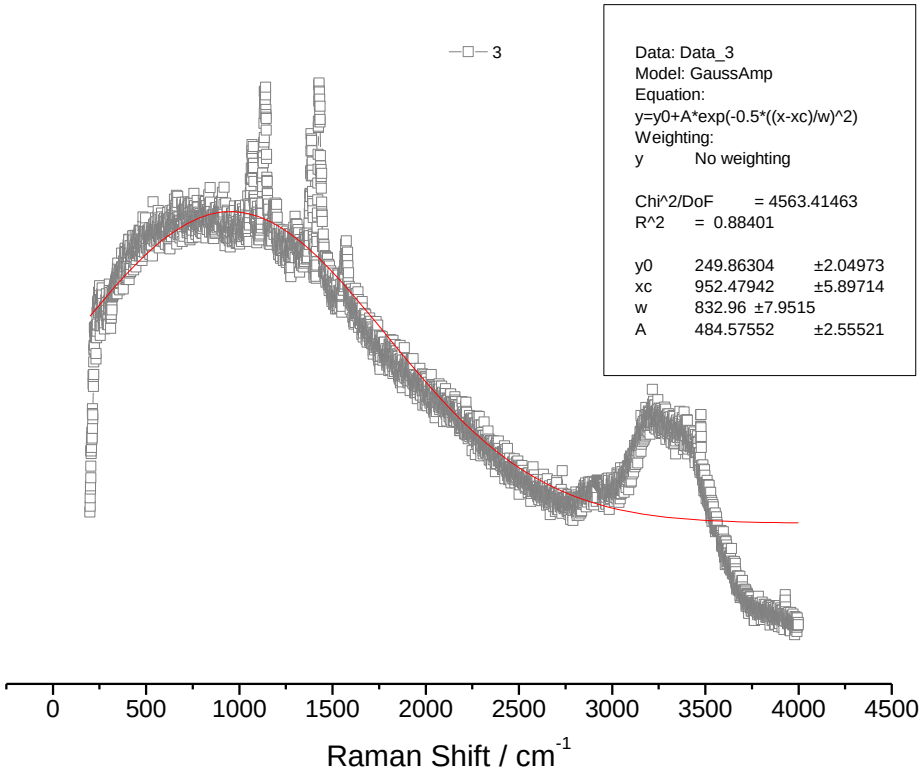

Figure 3-16 – Example of curve fitting to find background centre of BT using a Gaussian curve fit

The intensity of the background as a function of potential is shown in Figure 3-17. The most striking feature is the decrease in background intensity upon stripping of the adsorbate layer, (above -1.2 V). This further confirms the mechanism described above, as when the adsorbate is removed from the surface there can be no spectrum from the image molecule, and hence no background.

Another feature to note is that the background increases in intensity with increasingly negative potential (until stripping, that is). This can be explained by an increase in the polarisability of the real and image molecules, cause by an increase in

electron density at the electrode surface. A small increase in electron density (unlike the large increase seen in 3.3.2) would result in a greater polarisability, and hence stronger Raman spectrum, and subsequently a larger background. Moreover an increase in electron density at the surface of the electrode (from an applied potential), will result in an increase in the Raman spectrum from the image molecule (and consequently the background), as it is caused by the electrons of the metal.

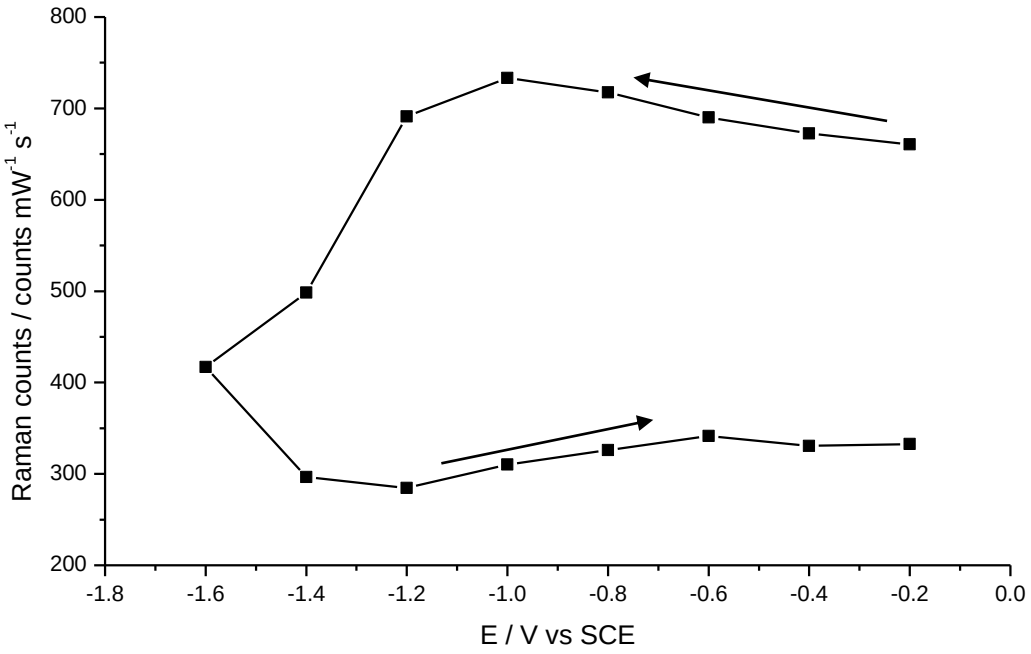

Figure 3-17 – Intensity of background at 954 cm^{-1} for BT during electrochemical stripping

On the return scan there is a slight increase in background intensity as the potential becomes more positive, however this can simply be attributed to the reformation of the adsorbate layer. This is confirmed by the reappearance of BT peaks in the spectra at these potentials (see Figure 3-15).

3.4.2. Electrochemical stripping of pyridine

The potential dependent experiment was repeated with the electrochemical stripping of pyridine, again in 0.1 M $NaClO_4$. Previous electrochemical stripping of pyridine [33] showed that at negative potentials (below -0.6 V vs SCE) pyridine is no longer chemisorbed to the surface (see Figure 3-18), and at -1.6 V is stripped completely.

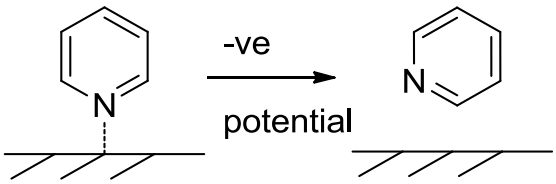

Figure 3-18 – Schematic of the change from chemisorbed to physisorbed pyridine at negative potentials

The spectra are shown in Figure 3-19, and the intensity of the pyridine peaks are in agreement with those in the literature. Again a correlation between substrate stripping and background intensity is observed, (as in the case of BT).

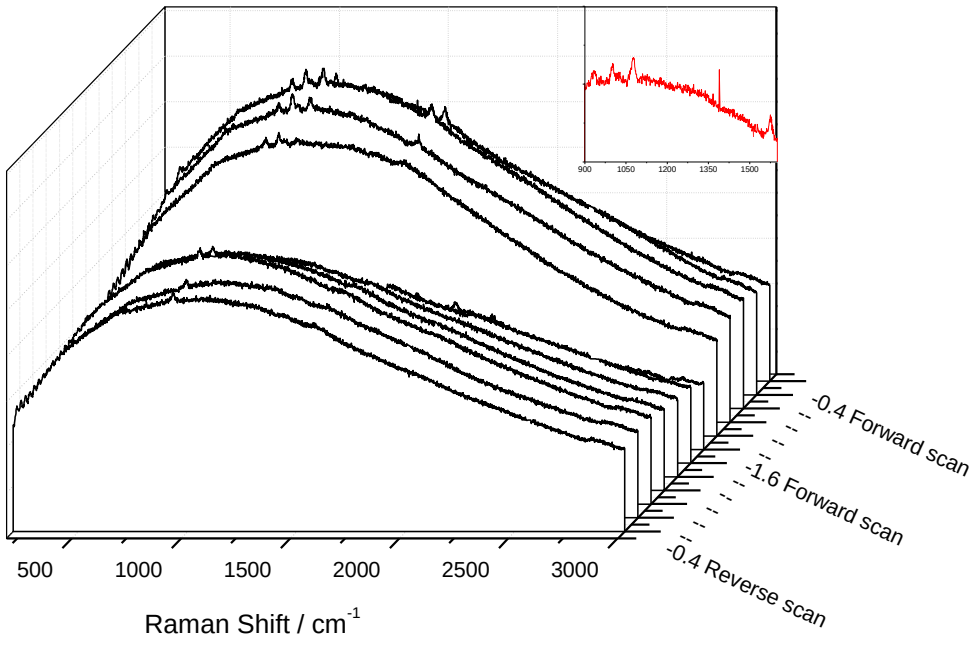

Figure 3-19 – Potential dependant SERS spectra of pyridine during electrochemical stripping off a Au 600 nm 0.75 *d* SSV substrate in 0.1 M $NaClO_4$. All spectra were obtained with 3 mW HeNe 633 nm laser, a scan time of 10 s and all potentials are reported vs SCE. Spectra were obtained from -0.4 and -1.6 V for forward and reverse scans at 0.2 V intervals. Inset shows the initial spectrum at -0.4 V.

The centre of the background was taken to be at 1010 cm^{-1}, (from Gaussian curve fitting), and its intensity as a function of potential is shown in Figure 3-20. The background increases in intensity until a maximum at -0.8 V before decreasing slowly until -1.2 V and then quickly until -1.6 V. This is consistent with the results on BT, as a slight stripping effect is observed between -0.8 and -1.2 V, which explains the small decrease (before the sharp decline associated with complete removal of the pyridine <-1.2 V).

The increase in intensity on the return sweep can be attributed to the reformation of the adsorbate layer again. The maximum at -0.8 V is still observed on the return scan, with a subsequent small decrease in intensity as the potential is increased to -0.4 V.

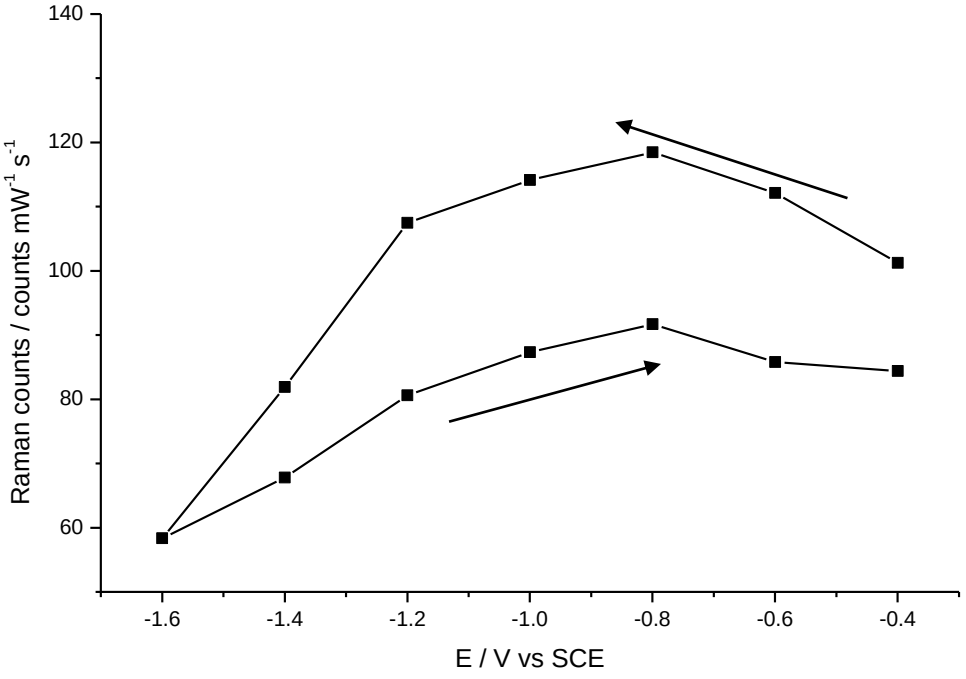

Figure 3-20 – Intensity of background at 1010 cm^{-1} for pyridine during electrochemical stripping

It is worth noting that whilst the pyridine is still present at the surface of the substrate the background is still strong. The change in binding nature from chemisorption to physisorption makes very little difference, if anything the background continues to increase in intensity (attributed to an increase in electron density from the applied potential).

3.4.3. Electrochemcial stripping of thiouracil

The stripping of BT illustrates a correlation between background intensity and the presence of an adsorbate, and stripping of pyridine shows that the change in nature of the interaction from chemisorption to physisorption does not affect its intensity. To gain a grasp of how the molecular orientation affects the background the stripping of thiouracil (TU) was investigated, as TU is known to change orientation without breaking the adsorbate-metal bond before desorption [34].

The CV of TU on Au (see Figure 3-21) clearly shows a feature corresponding to the reorientation of the molecule from perpendicular to the surface (at 0 V) to becoming more parallel (at -0.8 V), which is in agreement with the literature [34].

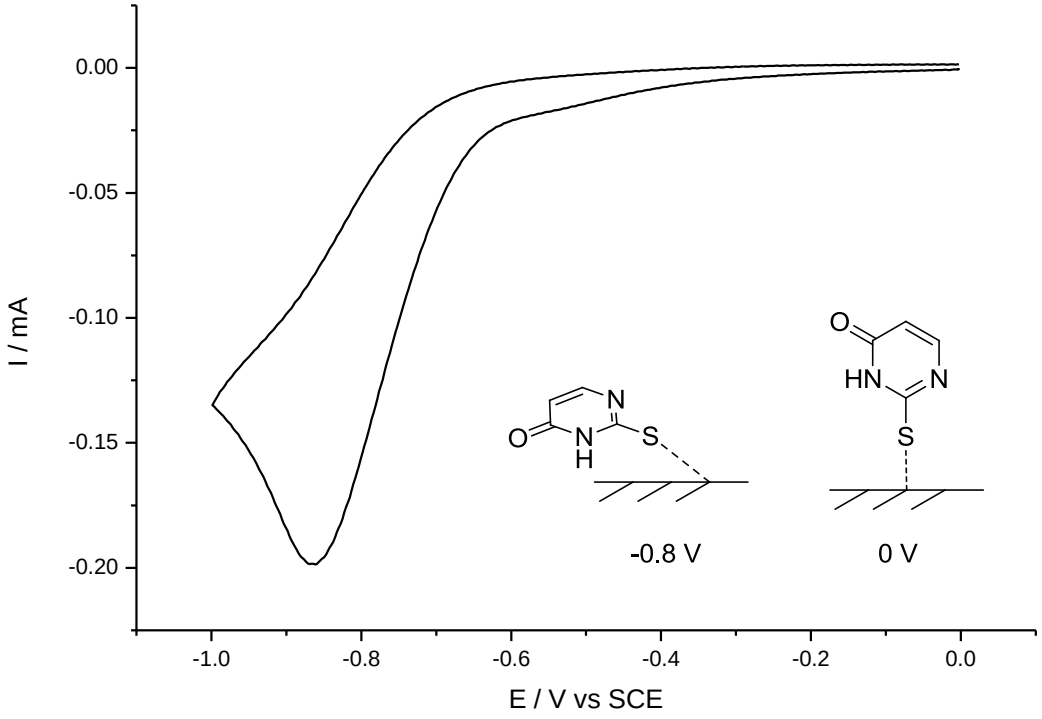

Figure 3-21 – Cyclic voltammogram of an adsorbed layer of TU on a Au 600 nm 0.75 *d* SSV substrate in 0.1 M $NaClO_4$ at 100 mV s^{-1} with a Pt gauze counter and SCE reference electrode. The reported [34] orientations of TU at various potentials are shown in the inset.

The spectra (see Figure 3-22) show a strong background for the initial scan (at -0.1 V), the exact reason for which is unclear. This may be due to a disordered adsorbate structure, or the presence of some TU bound through a N-Au interaction. Either way, the spectrum changes appearance at -0.3 V, and all subsequent spectra maintain the new shape, suggesting that applying a sufficiently large potential causes reorientation of the adsorbate to a more homogenous structure.

Although small amounts of TU may be removed from the surface during the change in orientation, no significant stripping occurs, as is evident from the presence of peaks in the spectrum over the entire potential range.

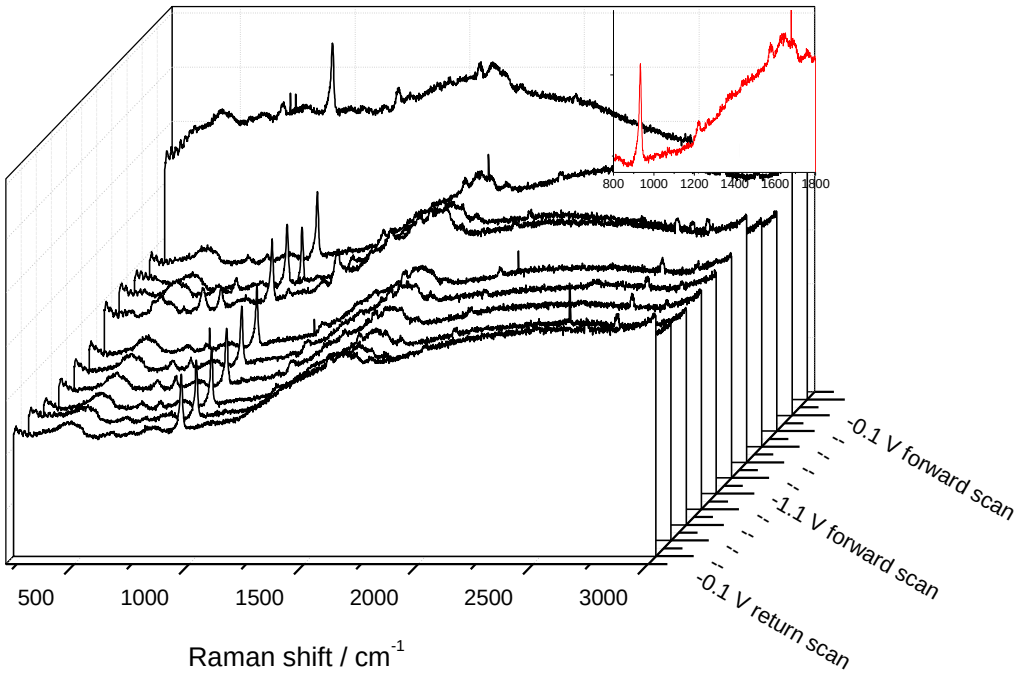

Figure 3-22 – Potential dependant SERS spectra of TU during electrochemical stripping off a Au 600 nm 0.75 *d* SSV substrate in 0.1 M $NaClO_4$. All spectra were obtained with 3 mW HeNe 633 nm laser, a scan time of 10 s and all potentials are reported vs SCE.

The centre of the background was taken to be 2200 cm^{-1}, and its intensity as a function of potential is shown in Figure 3-23. The background decreases in intensity initially with increasingly negative potential, possibly due to an ordering of adsorbate structure. The background then increases up to a maximum -0.9 V before decreasing as the TU switches to lie parallel to the surface of the electrode.

These results continue the trend of both BT and pyridine, as increasing negative potential increases the background intensity, until a change in the environment occurs. If the adsorbate is stripped off the surface the background decreases significantly: by ~66% and ~50% for BT and pyridine respectively. In this case the TU only changes orientation, which results in a decrease in Raman intensity (explained by the surface selection rules – see Chapter 1), and subsequently only a decrease of ~20%.

The background remains relatively constant on the return scan as there is no driving force for a reorientation of the adsorbate to the original perpendicular orientation. The parallel orientation will have a greater interaction of the N and O atoms of the TU with the Au, and is stable up until -0.3 V where a small degree of reorientation

can be deduced from the background intensity. There is no significant peak in the CV however showing complete reorientation of the adsorbate, which explains why the initial background intensity is not recovered.

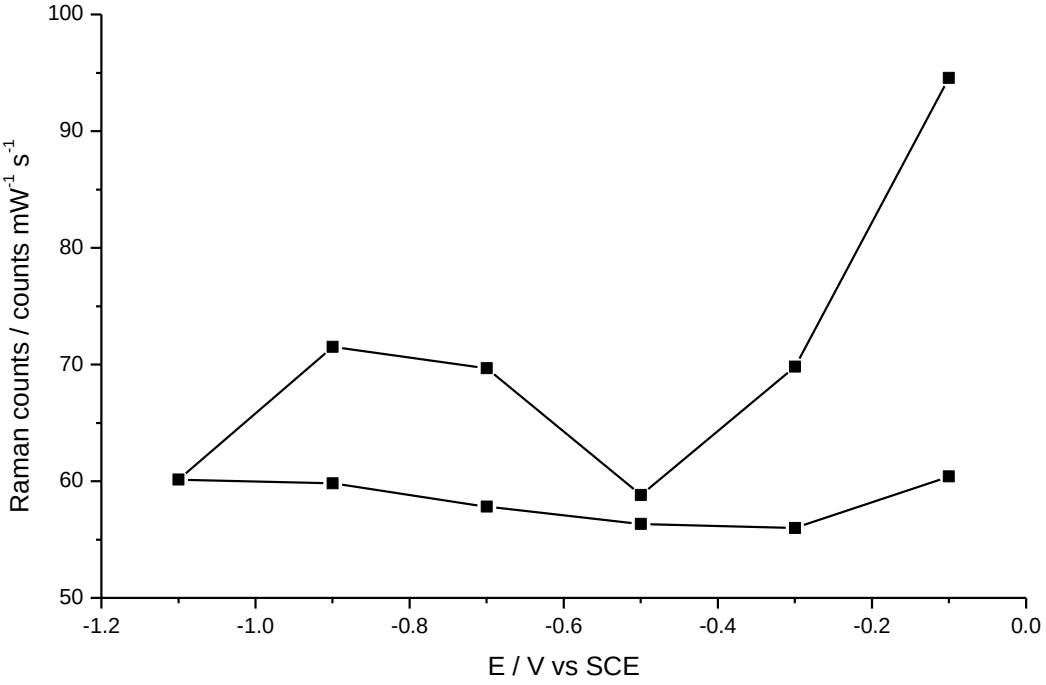

Figure 3-23 – Intensity of background at 2200 cm^{-1} for TU during an electrochemically induced change in orientation

3.5. Summary

The effect that instrumental setup and experimental design on SERS response has been briefly investigated. A comparison of the various objectives used in this study has been performed, which confirms that if a small aperture (and hence small cone angle) is used only part of the plasmon mode is accessed, and a less intense spectrum is obtained. The optimum angular orientation of the long working distance X5 objective (used for spectroelectrochemical measurements) and substrate was found to be close to normal incidence.

It has been shown that the binding of an organic adsorbate *via* chemisorption results in a slight change to the plasmonics of a 600 nm 0.75 *d* SSV substrate. The largest difference is the reduction of absorption at lower energies (~1.35 eV), and a small change in angular dependence. The larger mode at 1.9 eV remains largely unaffected.

The SERS spectra resulting from two different binding motifs (thiol adsorption and diazonium salt reduction) have been compared, and a drastic difference between the two observed. The thiol adsorption results in a strong spectrum, whilst the DS reduction shows a much weaker spectrum than expected. Theoretical calculations suggest that when the organic monolayer is formed through electroreduction of a diazonium salt the formation of a Au-C bond results in an inherent polarisation within the probe molecule, which (certainly for simple small molecules such as benzene) cause a drastic loss of SERS for the related vibration whilst other vibrations such as the various C-H stretches for example in benzene are relatively unchanged. The electrons in the p orbital of the S in benzenethiol effectively act as a buffer between the ring and the Au, allowing the molecule to maintain its high levels of polarisability, and hence stronger SERS.

The proposed model for the origin of the spectral background has also been introduced, as well as some electrochemical stripping experiments to gain further insight into the adsorbate dependence. When the organic adsorbate is removed, (as in the case of BT) the background drops significantly at the point of oxidative stripping, resulting in a decrease of ~66%.

The change in nature of absorption (from chemisorption to physisorption) evident with stripping of pyridine from the electrode does not result in any significant change either. It is not until the pyridine is removed from the surface completely that the background is seen to decrease, (by ~50%). When the adsorbate is not removed and only forced to undergo a change in orientation, the background demonstrates a slight dependency on orientation, which is explained by the surface selection rules. All these results further suggest that the background is indeed caused by the Raman scattering of the image molecule, as previously hypothesised.

For clarity all subsequent spectra in this thesis will be background substracted.

3.6.References

1. P. Hendra, C. Jones and W. Warnes, *Fourier Transform Raman Spectroscopy*, Ellis Horwood, Chichester, 1991.
2. J. M. McLellan, Z.-Y. Li, A. R. Siekkinen and Y. Xia, *Nano Letters*, 2007, **7**, 1013-1017.
3. Y. J. Liu, J. G. Fan, Y. P. Zhao, S. Shanmukh and R. A. Dluhy, *Applied Physics Letters*, 2006, **89**.
4. J. J. Baumberg, T. A. Kelf, Y. Sugawara, S. Cintra, M. E. Abdelsalam, P. N. Bartlett and A. E. Russell, *Nano Letters*, 2005, **5**, 2262-2267.
5. Nikon, MicroscopyU.
6. S. Cintra, M. E. Abdelsalam, P. N. Bartlett, J. J. Baumberg, T. A. Kelf, Y. Sugawara and A. E. Russell, *Faraday Discussions*, 2006, **132**, 191-199.
7. S. H. Pelfrey, University of Southampton, 2008.
8. A. J. Haes, S. L. Zou, J. Zhao, G. C. Schatz and R. P. Van Duyne, *Journal of the American Chemical Society*, 2006, **128**, 10905-10914.
9. J. N. Anker, W. P. Hall, O. Lyandres, N. C. Shah, J. Zhao and R. P. Van Duyne, *Nat Mater*, 2008, **7**, 442-453.
10. A. J. Haes, L. Chang, W. L. Klein and R. P. Van Duyne, *Journal of the American Chemical Society*, 2005, **127**, 2264-2271.
11. J. J. Hickman, P. E. Laibinis, D. I. Auerbach, C. F. Zou, T. J. Gardner, G. M. Whitesides and M. S. Wrighton, *Langmuir*, 1992, **8**, 357-359.
12. A. Kudelski and W. Hill, *Langmuir*, 1999, **15**, 3162-3168.
13. S. Frey, V. Stadler, K. Heister, W. Eck, M. Zharnikov, M. Grunze, B. Zeysing and A. Terfort, *Langmuir*, 2001, **17**, 2408-2415.
14. C. D. Zangmeister, S. W. Robey, R. D. van Zee, J. G. Kushmerick, J. Naciri, Y. Yao, J. M. Tour, B. Varughese, B. Xu and J. E. Reutt-Robey, *The Journal of Physical Chemistry B*, 2006, **110**, 17138-17144.
15. J. Tien, A. Terfort and G. M. Whitesides, *Langmuir*, 1997, **13**, 5349-5355.
16. X.-M. Lin, Y. Cui, Y.-H. Xu, B. Ren and Z.-Q. Tian, *Analytical and Bioanalytical Chemistry*, 2009, **394**, 1729-1745.
17. M. Yuan, S. Zhan, X. Zhou, Y. Liu, L. Feng, Y. Lin, Z. Zhang and J. Hu, *Langmuir*, 2008, **24**, 8707-8710.

18. J. M. Chretien, M. A. Ghanem, P. N. Bartlett and J. D. Kilburn, *Chem.-Eur. J.*, 2008, **14**, 2548-2556.
19. J. M. Chretien, M. A. Ghanem, P. N. Bartlett and J. D. Kilburn, *Chem.-Eur. J.*, 2009, **15**, 11928-11936.
20. B. L. V. Prasad, S. I. Stoeva, C. M. Sorensen and K. J. Klabunde, *Chemistry of Materials*, 2003, **15**, 935-942.
21. S. Mahajan, University of Southampton, 2008.
22. E. de la Llave, A. Ricci, E. J. Calvo and D. n. A. Scherlis, *The Journal of Physical Chemistry C*, 2008, **112**, 17611-17617.
23. R. M. Cole, J. J. Baumberg, F. J. Garcia de Abajo, S. Mahajan, M. Abdelsalam and P. N. Bartlett, *Nano Letters*, 2007, **7**, 2094-2100.
24. CambridgeSoft, in *ChemOffice 2009*, CambridgeSoft, 12.0 edn., 2009, p. Chem3D.
25. K. Nakamoto, *Infrared and Raman spectra of inorganic and coordinated compounds, 3rd edition*, Wiley, 1977.
26. H. R. Wang and G. Z. Wu, *Chemical Physics Letters*, 2006, **421**, 460-463.
27. Y. M. Zhao, H. R. Wang and G. Z. Wu, *Spectrochimica Acta Part a-Molecular and Biomolecular Spectroscopy*, 2007, **66**, 1175-1179.
28. K. M. Gough and H. K. Srivastava, *J. Phys. Chem.*, 1996, **100**, 5210-5216.
29. E. D. Schmid and R. D. Topsom, *Journal of the American Chemical Society*, 1981, **103**, 1628-1632.
30. T. A. Kelf, Y. Sugawara, R. M. Cole, J. J. Baumberg, M. E. Abdelsalam, S. Cintra, S. Mahajan, A. E. Russell and P. N. Bartlett, *Physical Review B*, 2006, **74**.
31. T. V. Teperik, F. J. G. de Abajo, A. G. Borisov, M. Abdelsalam, P. N. Bartlett, Y. Sugawara and J. J. Baumberg, *Nat. Photonics*, 2008, **2**, 299-301.
32. S. Mahajan, R. M. Cole, J. D. Speed, S. H. Pelfrey, A. E. Russell, P. N. Bartlett, S. M. Barnett and J. J. Baumberg, *Journal of Physical Chemistry C*, 2010, **114**, 7242-7250.
33. M. E. Abdelsalam, P. N. Bartlett, J. J. Baumberg, S. Cintra, T. A. Kelf and A. E. Russell, *Electrochemistry Communications*, 2005, **7**, 740-744.
34. H. B. Aguiar, A. C. Sant'Ana, M. L. A. Temperini, P. Corio and F. Cunha, *Vibrational Spectroscopy*, 2006, **40**, 127-132.

4. Metal Overlayers and borrowed SERS

This chapter focuses on the use of the borrowed SERS effect [1] to study electrochemical and electrocatalytic environments on Pt surfaces using the plasmonic properties of Au SSV substrates. The technique employed uses an ultra thin metal overlayer deposited galvanostatically as first described by Weaver *et al.* [2-4]. Conventionally, to achieve borrowed SERS, either an electrochemically roughened surface [2, 4, 5] or colloidal aggregate [6] is used as the base substrate, both of which have been used previously to study electrocatalytic reactions [7].

4.1. Thin film deposition on SSV and ORC substrates

The highly ordered and reproducible nature of SSV substrates allows an in depth knowledge of their plasmonics [8, 9], and how this translates into performance as SERS substrates [10]. This section will focus on how a galvanostatically deposited Pt overlayer affects the plasmonics and Raman spectra obtained on SSV substrates, and compare this to ORC roughened substrates.

The ORC roughened substrates were prepared according to a literature procedure [11] whereby a Au coated slide was immersed in 0.1 M KCl and roughened by 25 oxidation-reduction cycles from 1.25 V to -0.25 V vs SCE.

Ultrathin Pt overlayers were deposited on both types of substrate galvanostatically from 5 mM H_2PtCl_6 in 0.5 M Na_2HPO_4 solution with a current of -0.4 mA cm^{-2} (real area) for 40 s. All Pt modified Au substrates shall be referred to as PtAu substrates.

4.1.1. Plasmonics

Reflectance maps of SSV and ORC substrates were collected using the goniometer-based spectrometer described in Chapter 2. To fully understand and compare the differences both Au and Pt SSV substrates were measured as well as Au ORC and PtAu SSV and ORC samples.

The Au SSV (Figure 4-1) shows a strong absorption at ~1.9 eV, with a broad maximum from 15 to 32° angle of incidence. This angular dependence identifies the plasmon as a Bragg mode, which is determined by the structure of the film above the voids, not the voids themselves. An absorption is also seen at 1.3 eV, which is much

less angular dependant, and hence can be attributed to a mixed mode (containing elements of the Bragg and Mie modes).

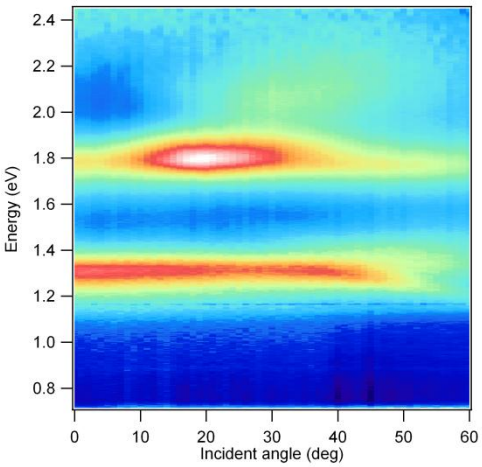

Figure 4-1 – Reflectance maps of Au 600 nm 0.75 *d* SSV and ORC substrates

It is well known that Pt SSV substrates offer much lower enhancements than Au [12] (an enhancement factor of 550 has been reported on Pt compared to 2.6 x10^7 for SSV), and this can be seen in the reflectance maps, as there is no absorption in the region of the laser line (1.9 eV), or Raman scattered light (~1.7 eV) (see Figure 4-2).

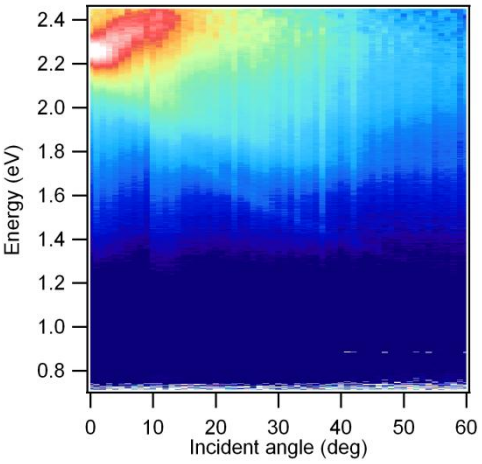

Figure 4-2 – Reflectance map of Pt 600 nm 0.75 *d* SSV substrate

There is, however, a strongly angular dependant mode from 2.2 – 2.4 eV centred around 3° angle of incidence. Previous work has shown that Pd films can be used to achieve UV SERS [13], and it may be possible to obtain SERS using a common green laser source and the Pt substrate (such as a frequency doubled Nd:YAG giving an output of 532 nm, equivalent to 2.3 eV), but that is beyond the scope of this project.

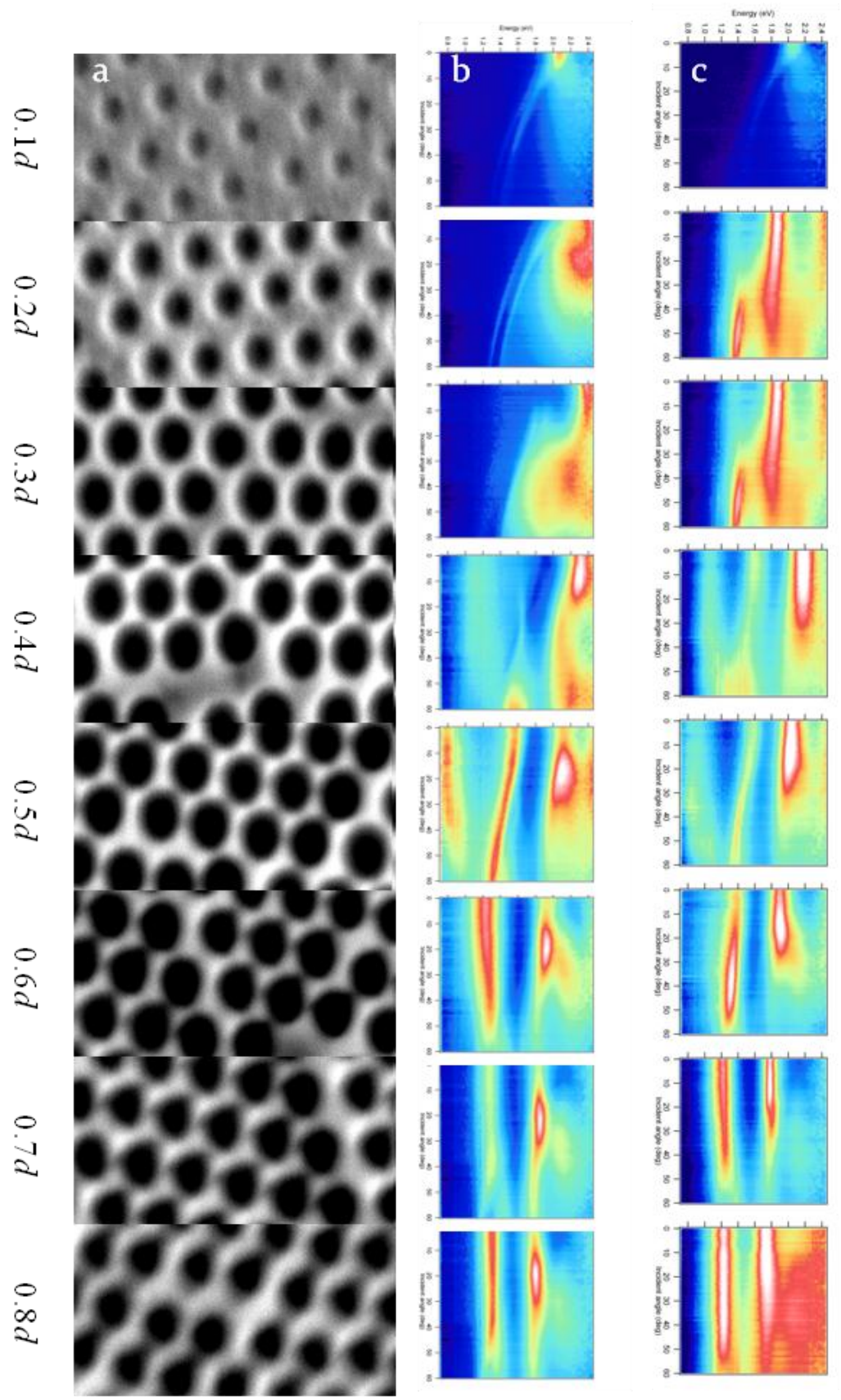

Figure 4-3 – A graded SSV sample, with a) scanning electron micrograph, b) reflectance maps for Au and c) reflectance maps for PtAu. In each map the x axis represents angle of incidence (0 to 60°), the y axis energy (from 0.6 to 2.4 eV) and the colour axis represents absorption, with dark low absorption and red/white high absorption.

One of the most effective ways to understand the plasmonics of an SSV substrate is through the use of a graded sample. The thickness of the film is increased in regular steps, and the reflectance map obtained at each step (see Figure 4-3).

From low film thicknesses (0.1 *d* to 0.4 *d*) the substrate can be thought of as a two dimensional grating, and the reflectance maps are dominated by the Bragg mode at higher energy. As the film height increases the top surface of the substrate becomes a series of triangles, and the Bragg mode is lost and Mie modes (standing waves inside the cavity) become much more important. At high film heights (> 0.6 *d*) a balance is struck between the two modes, and some mixed modes are observed as well.

There are some distinctive differences to the plasmonics once the Pt modification has been undertaken. There is a definite muting of the Bragg mode on a 0.1 *d* substrate, and the mode is shifted to very high energies (> 2.4 eV) on 0.2 and 0.3 *d* substrate. From 0.4 *d* onwards the plasmonics bear resemblance to those on a Au SSV, but the Mie modes become very intense at normal incidence (whereas on Au the maxima start from 15° onwards). The mixed modes with their maxima close to normal incidence are shifted to slightly lower energy, and those with their maxima away from 0° are shifted to higher energy (about 0.05 eV in both cases).

This change in energy is most likely due to either a change in the wave vector of the mode, or a change in dielectric constant. A change in wave vector would be due to a change in rim-to-rim distance, but as the amount of Pt deposited is very small, and the resulting effect on wave vector should be equally small. The addition of Pt to the Au surface will lead to a change in the metal's dielectric constant, and it is this change that has most likely lead to the change in plasmons.

The overriding result from the reflectance spectra is that galvanostatic deposition of a Pt overlayer results in a slight change in the plasmonics of the substrate. The difference, however, is limited to less than 0.1 eV in energy, and 5° in the dependence on angle of incidence.

4.1.2. Electrochemical characterisation

The thin nature of the overlayer makes it difficult to characterise through techniques such as EDX as any signal from the Pt is obscured by that originating from the underlying Au substrate. SEM images (see Figure 4-4) show no difference from a bulk Au substrate, indicating that the Pt deposition did not peturb the underlying structure.

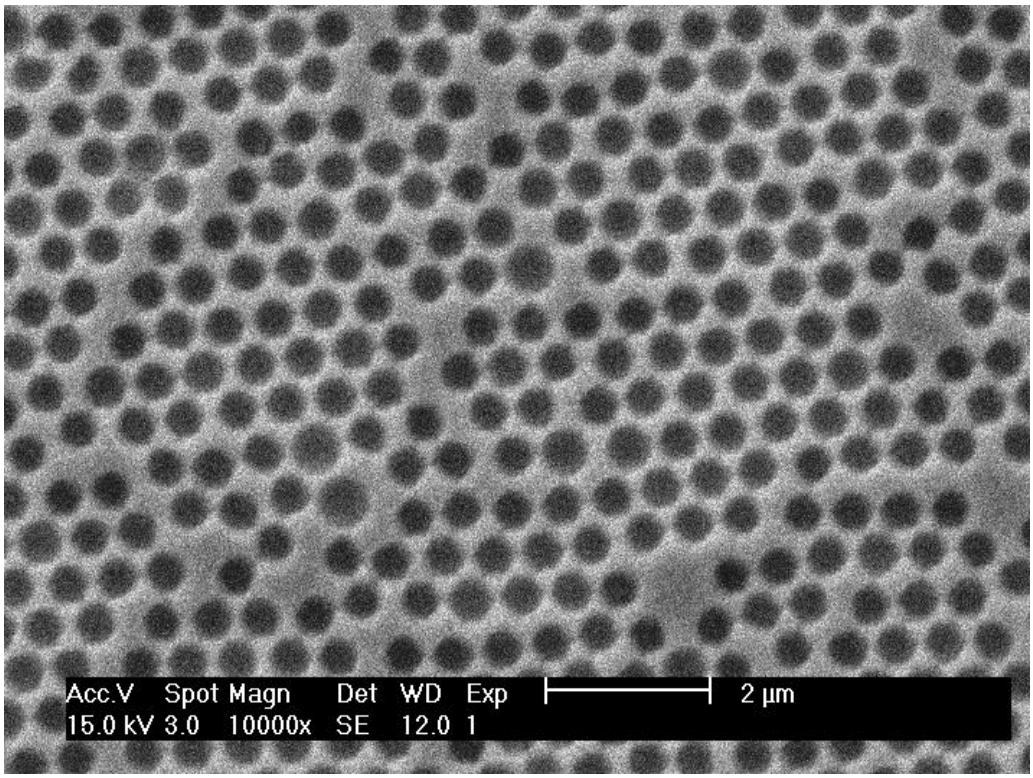

Figure 4-4 – SEM micrograph of a PtAu SSV substrate. The scale bar shows 2 µm.

Given the shortcomings of electron microscopy and EDX mentioned above, the most appropriate method of characterising the modified substrates was by performing cyclic voltammetry in acid, (see Figure 4-5). The unmodified Au substrates showed mostly double layer charging in the region shown here, and have been omitted for clarity.

Both the ORC and SSV substrates show hydrogen adsorption and stripping peaks between -0.45 and -0.65 V vs MMS, although the adsorption peaks are best defined on the ORC substrate. The SSV substrate shows a large feature for adsorption, but is poorly defined. These differences may be explained by the nature of the underlying substrate, as the SSV is much smoother than the ORC, which means the resulting overlayers will differ in topography.

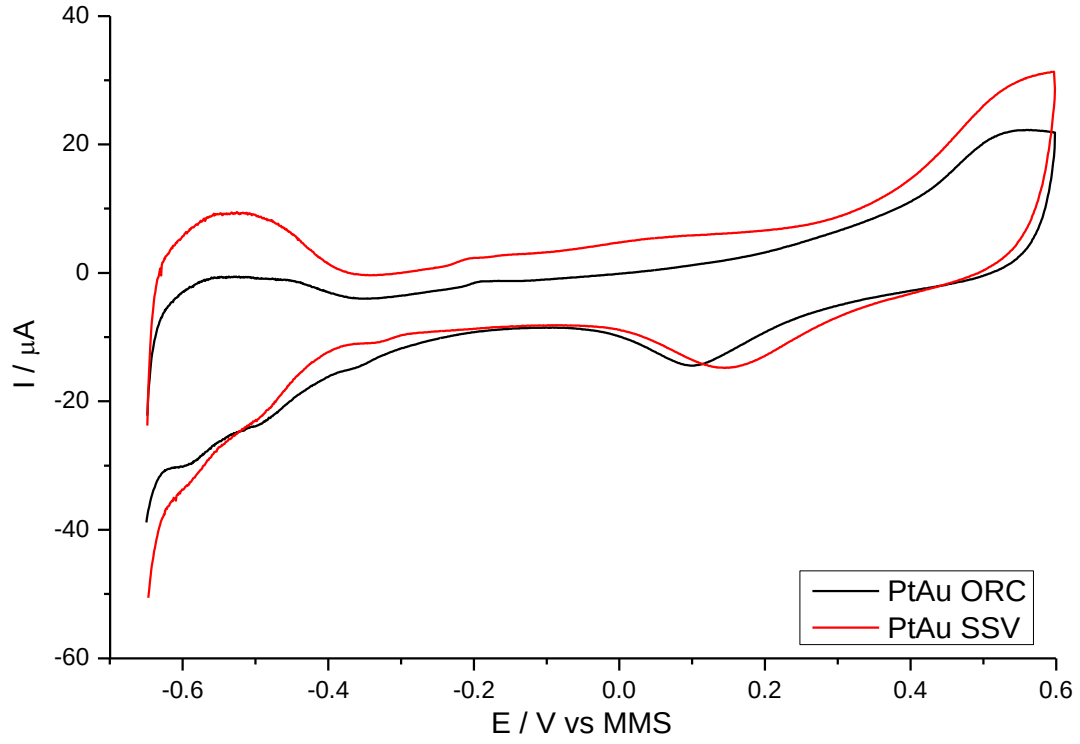

Figure 4-5 – Cyclic voltammogram of PtAu ORC and SSV substrates in 0.1 M H_2SO_4 taken at 100 mV s^{-1} with a Pt wire counter electrode and a MMS reference electrode.

The oxide stripping peak occurs at a slightly more positive potential on the SSV than the ORC, with values of 0.15 and 0.09 V respectively. This suggests that there is a difference in the chemical nature of the Pt overalyer between the ORC and SSV, which must originate in the underlying structure, (as this is the only difference between the two). Characterising the electrochemical differences between the two substrates is beyond the scope of this project.

The film was found to be unstable at higher potentials, so probing the nature of pinholes through the formation of Au oxide was not possible. There was no evidence of Au-S bonds on the PtAu modified substrates in benzenethiol spectra (see section 4.1.3), so it was assumed that no pinholes were formed.

4.1.3. Benzenethiol

Previous borrowed SERS type substrates have shown a decrease in SERS intensity with increasing overlayer thickness [14], so it is expected that the deposition of an overlayer onto a SERS active substrate would result in a loss of SERS enhancement. To quantify this with regards to an SSV substrate, the spectrum of benzenethiol was recorded on both ORC and SSV substrates for comparison, see Figure 4-6.

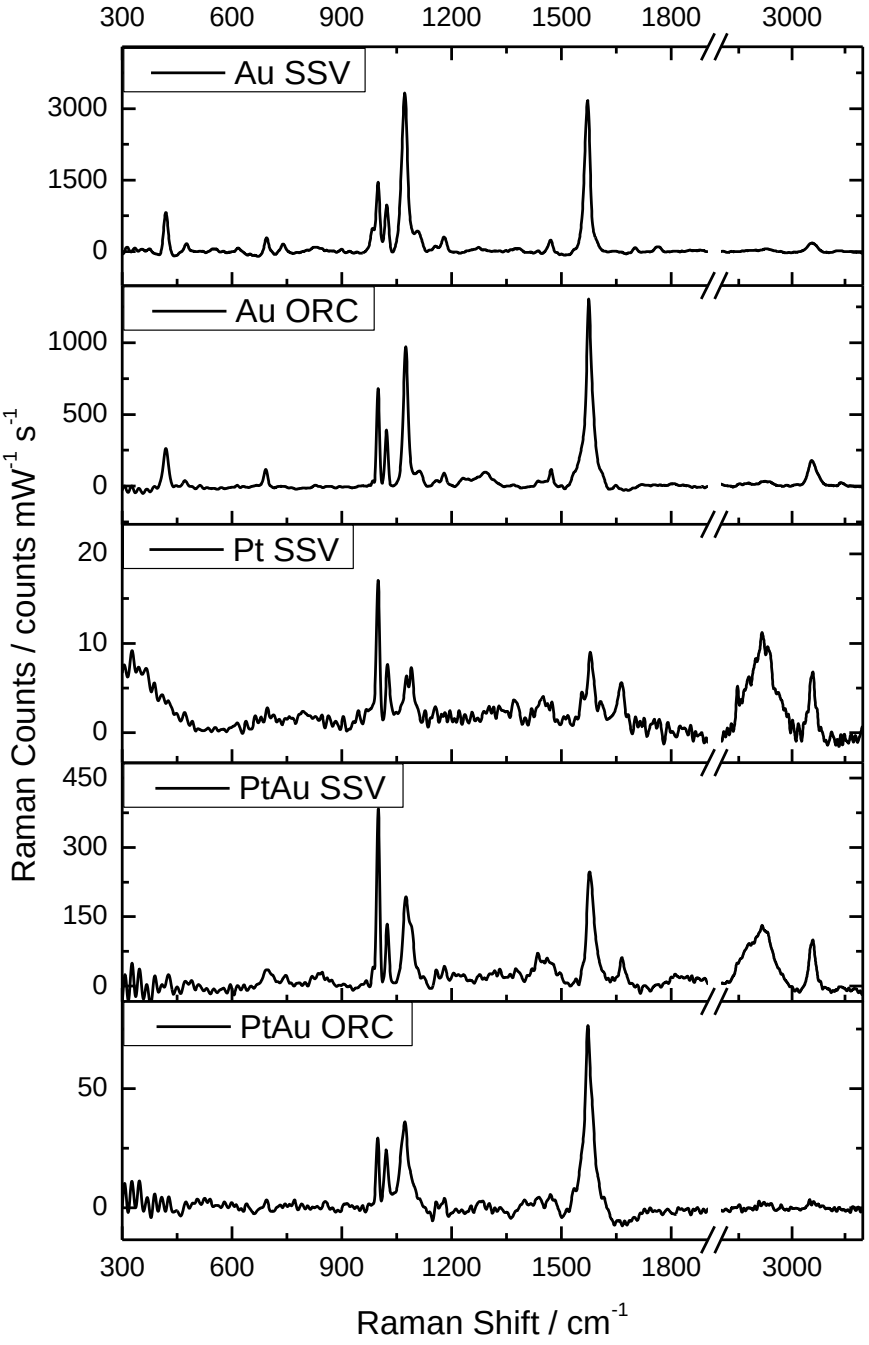

Figure 4-6 – SERS spectra of benzenethiol adsorbed onto various SSV and ORC SERS substrates taken with a 3 mW HeNe 633 nm laser and a 10 s scan time.

Modified substrates were left in a 10 mM ethanolic solution of benzenethiol overnight and the spectrum recorded. The spectrum obtained for an unmodified Au SSV substrate is in agreement with those previously recorded [15], showing two large peaks at 1072 and 1571 cm^{-1}, corresponding to 1 and 18a ring breathing stretches [16]. A full assignment of the bands is given in Table 3-2. The spectrum also clearly shows the peak associated with the ν(M-S) band at 420 cm^{-1} and the ν(C-S) at 694 cm^{-1}, although they are much less intense than the ring breathing modes. The γ(C-H) band at 740 cm^{-1} is present only in the SSV spectra. Lastly, it is worth noting that the symmetric ν(C-H) stretch at 3026 cm^{-1} is three times more intense than the barely observed anti-symmetric stretch at 2927 cm^{-1}.

Table 4-1 – Peak assignments and peak heights (in counts mW^{-1} s^{-1}) for benzenethiol adsorbed onto a variety of substrates

Peak centre / cm^{-1}	Assignment	AuSSV	Au ORC	Pt SSV	PtAu SSV	PtAu ORC
420	ν(M-S)	820	260			
694	ν(C-S)	290	120		35	4
740	γ(C-H)	150			20	
999	12	1450	680	17	380	30
1023	18a	960	390	8	130	25
1072	1	3330	970	6	200	40
1571	8a	3160	1310	9	250	80
2927	ν_{as}(C-H)	50		11	130	
3056	ν_{s}(C-H)	180	180	7	100	

The spectrum collected on the ORC substrate is very similar to that on the SSV, however the vast majority of the observed bands are about a third as intense on the roughened substrate. This is expected, as previous results [15] have shown much larger enhancement factors for SSV substrates than ORC (2.6×10^7 and 2.3×10^5 respectively).

One noticeable difference between the ORC and SSV Au substrates is in the C-H bands. Firstly, the γ(C-H) band at 740 cm^{-1} is not observed on the rough substrate, and secondly the relative intensity of the ν(C-H) symmetric stretch to the rest of the spectrum is much greater in the ORC substrate than SSV. This is attributed to the

difference in plasmonics of the substrates. Integration of the SSV plasmon map for a X50 objective with numerical aperture of 0.75 (see Figure 4-7) shows that the major regions of enhancement for outgoing radiation are between 250 and 1500 cm^{-1}, and that the higher frequency bands (such as ν(C-H) bands) are enhanced less. It is not possible to compare this to ORC substrates as they do not provide a reproducible enhancement.

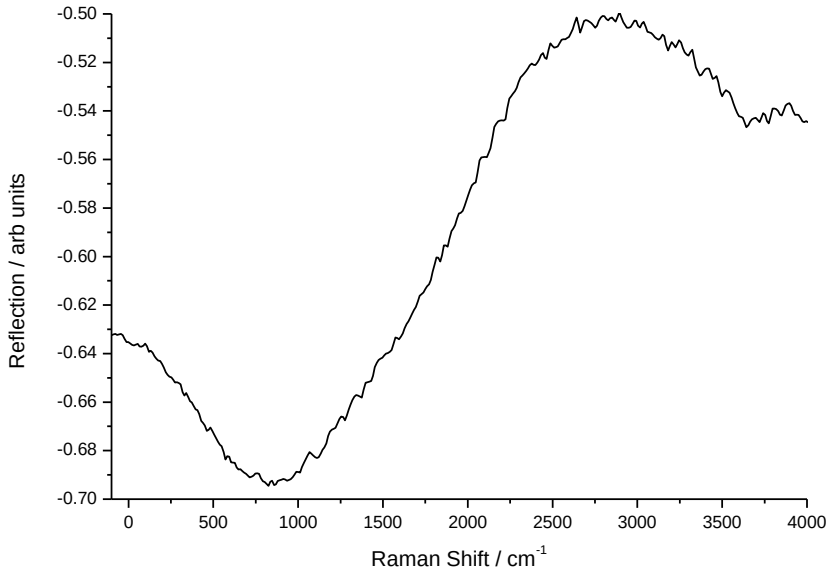

Figure 4-7 – Integrated reflection profile of reflectance map on a 600 nm 0.75 *d* SSV substrate for a X50 objective with numerical aperture of 0.75

The Pt SSV substrate shows very poor enhancement, which is expected given that the reflectance map shows very little absorption (see Figure 4-2). The ratio of band intensities within the spectrum is very different to that on the Au substrates. Figure 4-8 shows clearly that the Au spectra are dominated by the bands at 1072 and 1571 cm^{-1}, whilst the largest peak in the Pt spectrum is at 999 cm^{-1}. The ν_{as}(C-H) band at 2927 cm^{-1} is also much more strongly enhanced than the ν_s(C-H) stretch at 3096 cm^{-1} in the Pt spectrum. These differences are possibly due to charge transfer effects, which will be discussed in detail in Chapter 5.

The addition of a Pt overlayer to the SSV substrate shows a large decline in Raman signal, with an average decrease in peak intensity of ~7 fold. This may be explained by the strong distance dependence of the electric field strength on the SSV substrate, and is in agreement with previous examples of borrowed SERS [2, 4]. The chemical

nature of the substrate shows distinctive similarities to the bulk Pt equivalent, the most prevalent being the ratio of peak heights. As in the Pt SSV case, the peak at 999 cm^{-1} is by far the most intense in the spectrum, and the ν_{as}(C-H) band at 2927 cm^{-1} is also very strong.

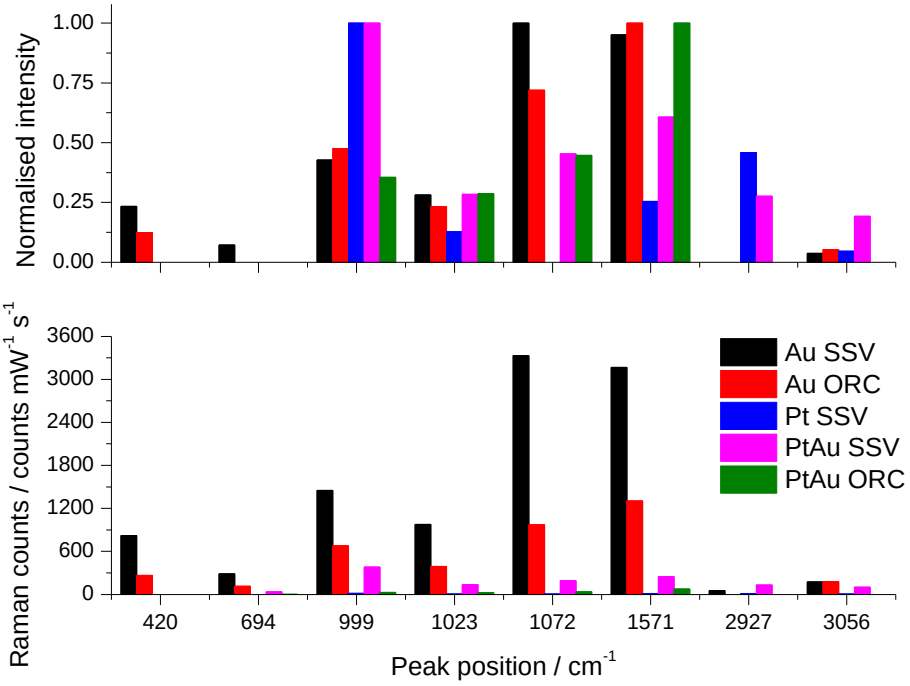

Figure 4-8 – Normalized (top) and absolute (bottom) intensity of peak heights in the SERS spectrum of benzenethiol on Au and Pt substrates taken with a 3 mW HeNe 633 nm laser and a 10 s scan time.

The PtAu ORC substrate shows less of an enhancement than the SSV equivalent, and is almost comparable with a bulk Pt SSV for peak intensities (see Figure 4-8). The spectrum is dominated by the one peak at 1571 cm^{-1}, with obvious other peaks at 999, 1023 and 1072 cm^{-1}. None of the C-H related bands are observable, and the ν(C-S) band at 694 cm^{-1} is barely distinguishable from the background noise. The spectrum is essentially similar to that obtained on Au ORC, but is much less intense.

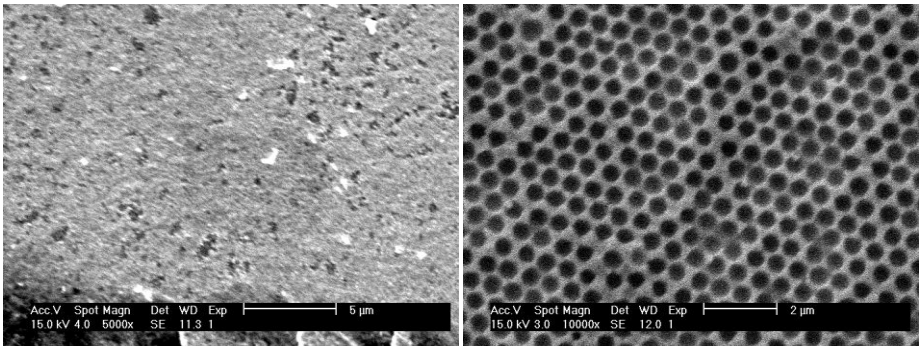

Figure 4-9 – SEM micrographs of ORC roughened Au and SSV structured Au. The scale bars are 5 and 2 µm for ORC and SSV respectively.

An explanation for this difference lies in the difference of structure between SSV and ORC substrates. The size of the features in an SSV substrate are very large (see Figure 4-9) – in this case of the order of 450 nm – whilst the size of the roughened peaks and troughs in an ORC substrate are of the order of <100 nm. This means that an unmodified SSV substrate has chemical properties mostly like flat Au, and with an overlayer the spectral data suggests it acts like flat Pt. The ORC substrate, however, acts much more like Au nanoparticles, which are well documented to have vastly different properties to flat Au [17]. The modified ORC substrate may well be acting much more like a PtAu alloy, or a Au@Pt core shell [18].

To summarise, SSV and ORC substrates were compared whilst unmodified and after coating with a galvanostatically deposited ultrathin layer of Pt. The SSV substrate outperformed the ORC substrate both on peak intensity, and in similarity to a Pt SSV spectrum on peak ratios. This is most likely due to the inherent rough nature of the ORC substrate, whereby the nanofeatures are acting more like immobilised nanoparticles than bulk Au.

4.2.NaSCN Spectroelectrochemistry

The benzenethiol adsorbate results suggest that the PtAu SSV substrate shows characteristics of bulk Pt whilst maintaining good SERS enhancement. The ideal use of an overlayer-modified substrate however, is for electrochemistry, so a comparison of how the various substrates perform in a spectroelectrochemical situation is necessary.

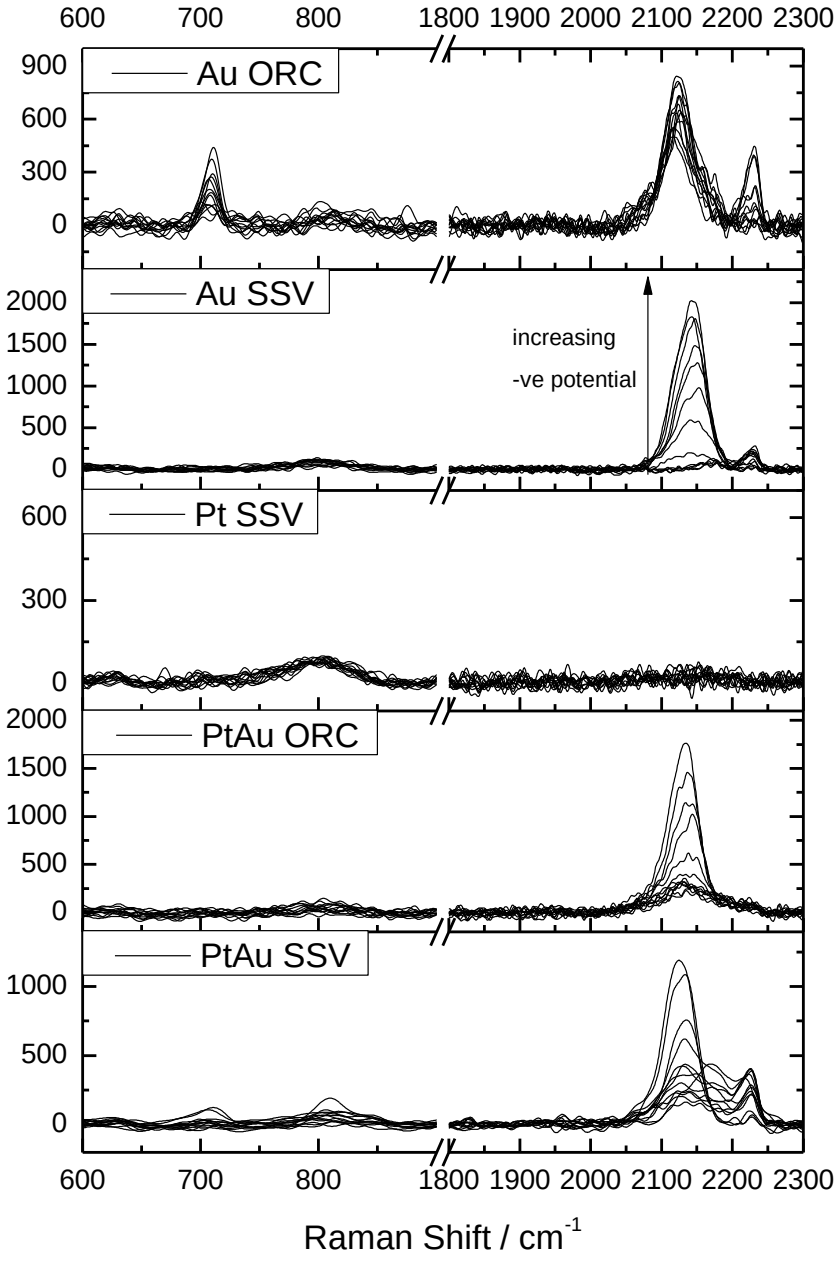

Figure 4-10 – Potential dependant SERS spectra of NaSCN adsorbed onto various SSV and ORC substrates in 5mM NaSCN and 0.1 M $NaClO_4$ solution.

The probe chosen for this comparison is sodium thiocyanate, as it has been previously shown to give good SERS with metal overlayers [3, 4]. The electrodes were positioned in the spectroelectrochemical cell and a solution of 5 mM NaSCN in 0.1 M $NaClO_4$ was added and purged with N_2 for 10 min. The desired potential was applied (all potentials are vs SCE), and the system allowed to equilibrate for 1 min before scanning. A collation of all the spectra acquired is given in Figure 4-10, and each spectrum is displayed individually below for a more precise potential-dependant study.

The spectra on Au SSV (see Figure 4-11) clearly show several bands (see Table 4-2). The spectra are dominated by the $\nu(CN)_{N\text{-bound}}$ band at 2140 cm^{-1} which becomes apparent from 0.1 V and reaches a maximum at -0.5 V. The swap from S-bound to N-bound ν(CN) bands is in agreement with the literature.

Table 4-2 – Peak assignments [3, 4, 19] for SCN^- and peak centres on various substrates at 0 V vs SCE

Assignment	Au SSV	Au ORC	Pt SSV	PtAu SSV	PtAu ORC
ν(CS)		710			
$\nu(CN)_{N\text{-bound}}$	2227	2220		2225	
$\nu(CN)_{S\text{-bound}}$	2140	2121		2140	2124

The ν(CS) band at 710 cm^{-1} is not observed on the Au SSV substrate, and this may again be due to the plasmonics. There are two distinctive differences between the experimental setup of benzenethiol and NaSCN, and these are the choice of objective and surrounding media. In the case of benzenethiol the objective used was a short working distance, high aperture objective (0.37 mm and 0.75 respectively); whereas the spectroelectrochemistry requires a longer working distance, which results in a smaller aperture (14 mm and 0.12 respectively). This means that the collection angle is changed substantially and, therefore, very different plasmon modes are accessed than in the benzenethiol case. Moreover, the difference in refractive index between air and water will result in a large change of the plasmonics. It is likely that the absorption close to the laser line tails off at ~500 cm^{-1} and no further enhancement is seen until ~2000 cm^{-1}, hence the apparent disappearance of the 710 cm^{-1} band.

The Au ORC substrate also delivers acceptable spectra, however the overall intensities and signal to noise ratios are reduced with respect to the SSV substrate. There is some evidence of a ν(M-SCN) band at 289 cm^{-1}, but this cannot be sufficiently resolved over the inherent noise from the notch filter cutoff (apparent in all spectra below 300 cm^{-1}). The ν(CS) band is present, becoming apparent after 0.1 V, which is consistent with the change from S-bound to N-bound. The shape and intensity of the δ(SCN) band remains relatively constant across the potential range, which is very different to the SSV case. The centre of the $\nu(CN)_{N\text{-bound}}$ band is also red-shifted by 20 cm^{-1} with respect to the SSV substrate (from 2120 to 2140 cm^{-1}).

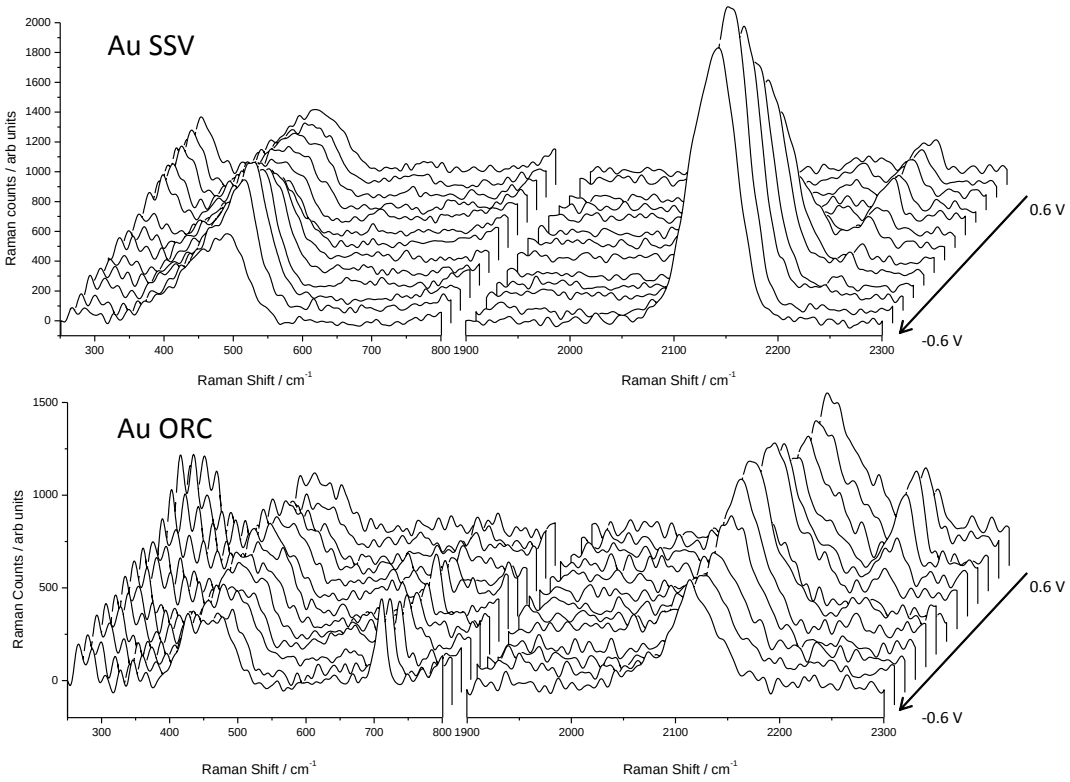

Figure 4-11 – SERS spectra of 5 mM NaSCN in 0.1 M $NaClO_4$ on Au SSV and ORC substrates, taken with a 3 mW 633 nm HeNe laser, a scan time of 45 s and a X5 objective with a working distance of 14 mm and NA of 0.12.

Both of these changes can be accounted for (once again) by the size of the features on the ORC substrate. If the thiocyanate is less strongly bound to the surface then the lone pair present on the N can feed into the C≡N bond and strengthen it, which results in a red-shift of the vibrational frequency. The difference in electronic behaviour of flat and nanostructured Au could well result in such an effect.

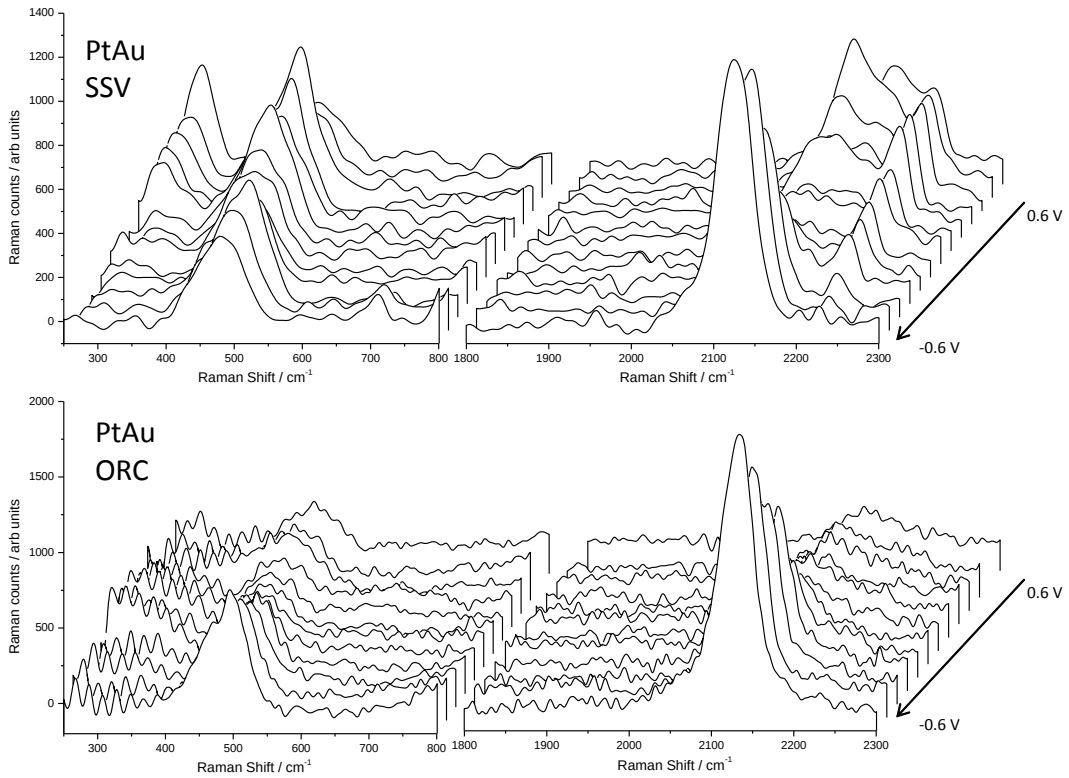

Figure 4-12 - SERS spectra of 5 mM NaSCN in 0.1 M $NaClO_4$ on PtAu SSV and ORC substrates, taken with a 3 mW 633 nm HeNe laser, a scan time of 45 s and a X5 objective with a working distance of 14 mm and NA of 0.12.

Deposition of the Pt overlayer onto the Au SSV and Au ORC substrates once again results in a loss of Raman signal, (see Figure 4-12), but the bands present on the Au substrates are still present. The characteristic change in Raman shift of the δ(SCN) band (see Figure 4-13) is moved from an onset of 0.1 V to -0.2 V. Previous studies on Pt core-shell SERS substrates have shown a change in orientation at similar potentials [20].

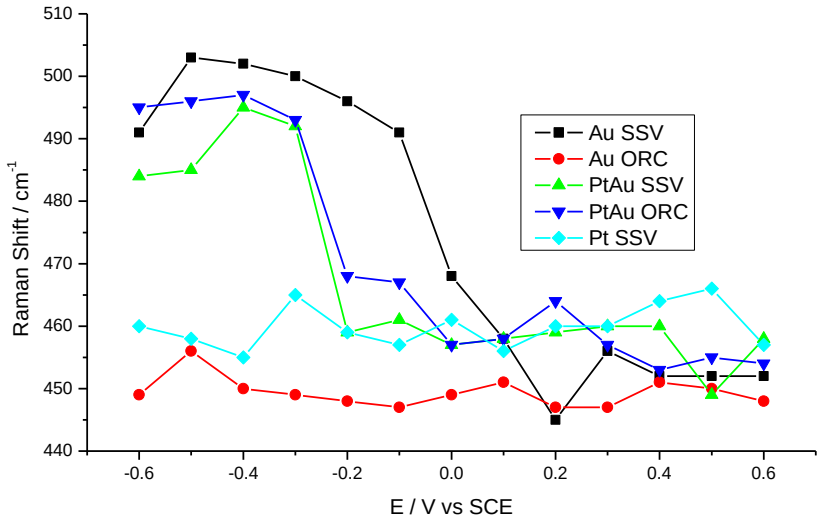

Figure 4-13 – Peak centre of the δ(SCN) band from the SERS spectra of 5 mM NaSCN in 0.1 M $NaClO_4$ on various SERS substrates.

The intensity of the N-bound *ν*(CN) stretch follows a similar trend (see Figure 4-14), with a distinctive growth in intensity from -0.2 V vs SCE on Pt modified electrodes (in comparison to 0.1 V on Au). The ORC substrate actually shows a stronger Raman signal in this case, with peaks consistently ~1.5 counts mW^{-1} s^{-1} higher. This is again due to the lack of plasmonic tuning on an ORC substrate, as it is less affected by the change of microscope objective, and the addition of water to the system.

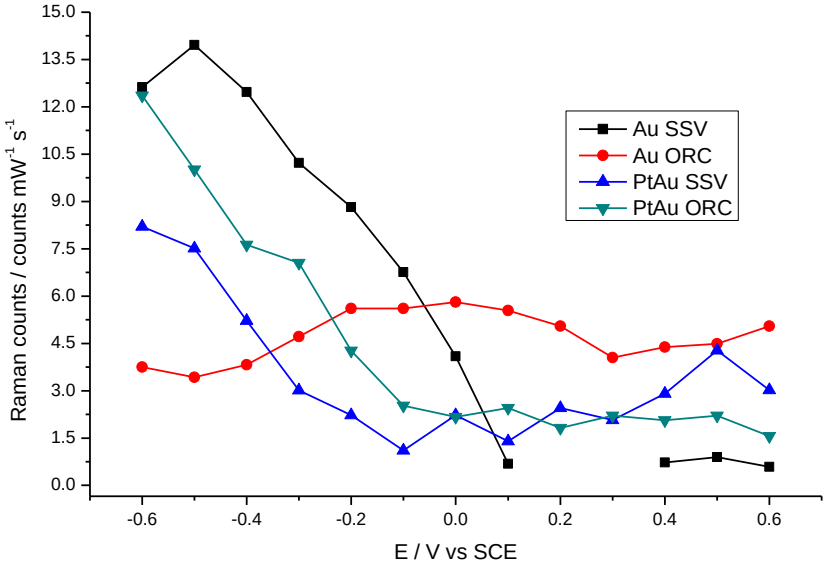

Figure 4-14 – Peak intensities for $\nu(CN)_{N\text{-bound}}$ band on Au and PtAu SSV and ORC substrates.

The extremely poor enhancement of the Pt SSV substrate hinders its direct comparison with PtAu substrates, but the results obtained are similar to previous reports, particularly the core-shell substrates [20]. The band attributed to S-bound *ν*(SCN) is not observed on the PtAu ORC substrate, which suggests that the SSV equivalent yields more truly representative spectra. The ORC does give a slightly stronger enhancement of the N-bound *ν*(SCN) stretch, however this is far outweighed by the observation of the S-bound species. Overall the thiocyanate system suggests that galvanostatically modified SSV substrates should prove to be extremely useful for the study of electrochemical reactions at Pt surfaces.

4.3.References

1. Z. Q. Tian, B. Ren, J. F. Li and Z. L. Yang, *Chemical Communications*, 2007, 3514-3534.
2. S. Zou and M. J. Weaver, *Analytical Chemistry*, 1998, **70**, 2387-2395.
3. H. Luo and M. J. Weaver, *Langmuir*, 1999, **15**, 8743-8749.
4. S. Zou, M. J. Weaver, X. Q. Li, B. Ren and Z. Q. Tian, *The Journal of Physical Chemistry B*, 1999, **103**, 4218-4222.
5. M. F. Mrozek, Y. Xie and M. J. Weaver, *Analytical Chemistry*, 2001, **73**, 5953-5960.
6. S. Park, P. X. Yang, P. Corredor and M. J. Weaver, *Journal of the American Chemical Society*, 2002, **124**, 2428-2429.
7. S. C. S. Lai, University of Leiden, 2010.
8. T. A. Kelf, Y. Sugawara, R. M. Cole, J. J. Baumberg, M. E. Abdelsalam, S. Cintra, S. Mahajan, A. E. Russell and P. N. Bartlett, *Physical Review B*, 2006, **74**.
9. R. M. Cole, J. J. Baumberg, F. J. Garcia de Abajo, S. Mahajan, M. Abdelsalam and P. N. Bartlett, *Nano Letters*, 2007, **7**, 2094-2100.
10. S. H. Pelfrey, University of Southampton, 2008.
11. P. Gao, D. Gosztola, L. W. H. Leung and M. J. Weaver, *Journal of Electroanalytical Chemistry*, 1987, **233**, 211-222.
12. M. E. Abdelsalam, S. Mahajan, P. N. Bartlett, J. J. Baumberg and A. E. Russell, *Journal of the American Chemical Society*, 2007, **129**, 7399-7406.

13. L. Cui, S. Mahajan, R. M. Cole, B. Soares, P. N. Bartlett, J. J. Baumberg, I. P. Hayward, B. Ren, A. E. Russell and Z. Q. Tian, *Physical Chemistry Chemical Physics*, 2009, **11**, 1023-1026.
14. P.-P. Fang, J.-F. Li, Z.-L. Yang, L.-M. Li, B. Ren and Z.-Q. Tian, *Journal of Raman Spectroscopy*, 2008, **39**, 1679-1687.
15. S. Cintra, M. E. Abdelsalam, P. N. Bartlett, J. J. Baumberg, T. A. Kelf, Y. Sugawara and A. E. Russell, *Faraday Discussions*, 2006, **132**, 191-199.
16. S. W. Han, S. J. Lee and K. Kim, *Langmuir*, 2001, **17**, 6981-6987.
17. S. Eustis and M. A. El-Sayed, *Chemical Society Reviews*, 2006, **35**, 209-217.
18. L. H. Lu, G. Y. Sun, H. J. Zhang, H. S. Wang, S. Q. Xi, J. Q. Hu, Z. Q. Tian and R. Chen, *Journal of Materials Chemistry*, 2004, **14**, 1005-1009.
19. D. B. Parry, J. M. Harris and K. Ashley, *Langmuir*, 1990, **6**, 209-217.
20. B. Zhang, J.-F. Li, Q.-L. Zhong, B. Ren, Z.-Q. Tian and S.-Z. Zou, *Langmuir*, 2005, **21**, 7449-7455.

5. Nanoparticle enhanced SERS

Confined plasmon modes are created when nanoparticles (NPs) or fine tips are brought into contact with each other or flat surfaces [1-3]. If an STM tip is brought very close to a flat surface, the resulting electromagnetic field can be used for enhanced Raman, and this is known as tip enhanced Raman spectroscopy, or TERS [4-6]. The concept explored in this chapter is to determine if, by tethering a metallic nanoparticle to an SSV surface results in an increase in the localised electric field to further enhance the SERS effect from the substrate.

5.1 Ag nanoparticle enhanced SERS

Ag nanoparticles are commonly used as SERS substrates [7-9], as they offer excellent enhancement and are simple to synthesise. By exploiting the favourable interaction of Ag and many heteroatoms to displace the NP's protecting agent (citrate in this case) it is easy to form a simple assembly of NPs, organic linker and the structured surface.

5.1.1 Experimental

Ag NPs were synthesised according to a the procedure described by Lee *et al.* [10]. 500 mL of 1 mM solution of $AgNO_3$ in water was brought to boiling, and to it was added 10 mL of 1% (by weight) solution of trisodium citrate. The mixture was allowed to reflux for 1 hr before cooling to room temperature, and the NPs were collected by centrifugation and used without any further purification. The resulting NPs (averaged of 50 NPs) have a diameter of 18.6 ± 3.6 nm (see Figure 5-1).

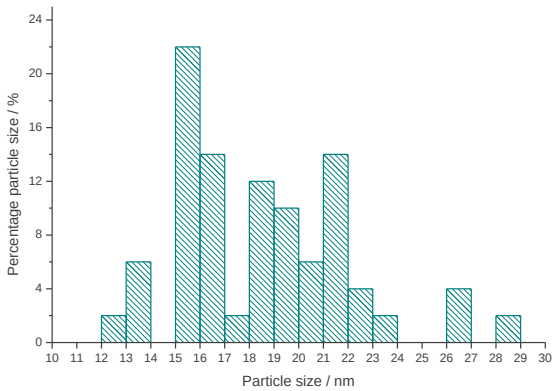

Figure 5-1 – Histogram of Ag NP size and TEM micrograph of the particles

The NPs were also characterised using UV-vis spectroscopy Figure 5-2), and the solution shows one clear peak at 403 nm, which is in agreement with the literature [10]. The absence of any other peaks, denotes that there is no visible aggregation of the particles, as this often causes absorption at longer wavelengths [9].

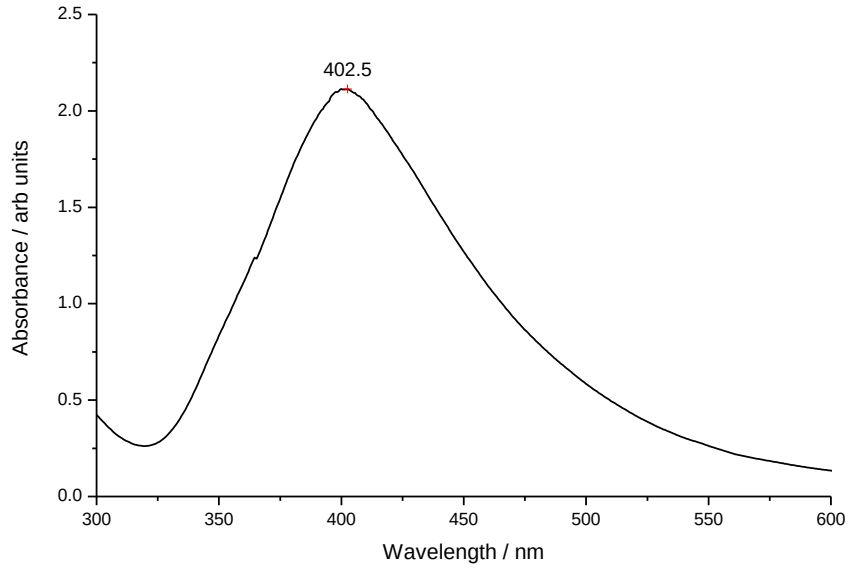

Figure 5-2 – UV-vis absorption spectrum of Ag NPs suspended in water

The organic adsorbate used as a tether for the NP was adsorbed onto the SSV substrate from a 10 mM ethanolic solution of the compound overnight, then the modified substrate was finally soaked in an aqueous NP suspension for 2 hr to form the final assembly (see Figure 5-3).

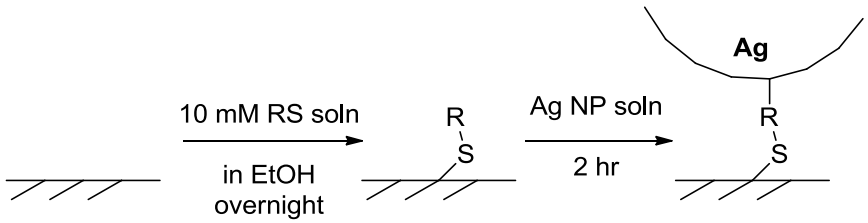

Figure 5-3 – Reaction scheme for the NP assembly

The modified substrate was washed with water and ethanol to remove any unbound NPs or desorbed organic linker. They were finally dried with N_2 before use.

5.1.2 Mercaptoaniline

Because of its similarity to benzenethiol, mercaptoaniline makes an excellent initial probe molecule. It has a large Raman scattering cross section, and an amine group para to the thiol, which means benzene ring lies in the centre of the assembly.

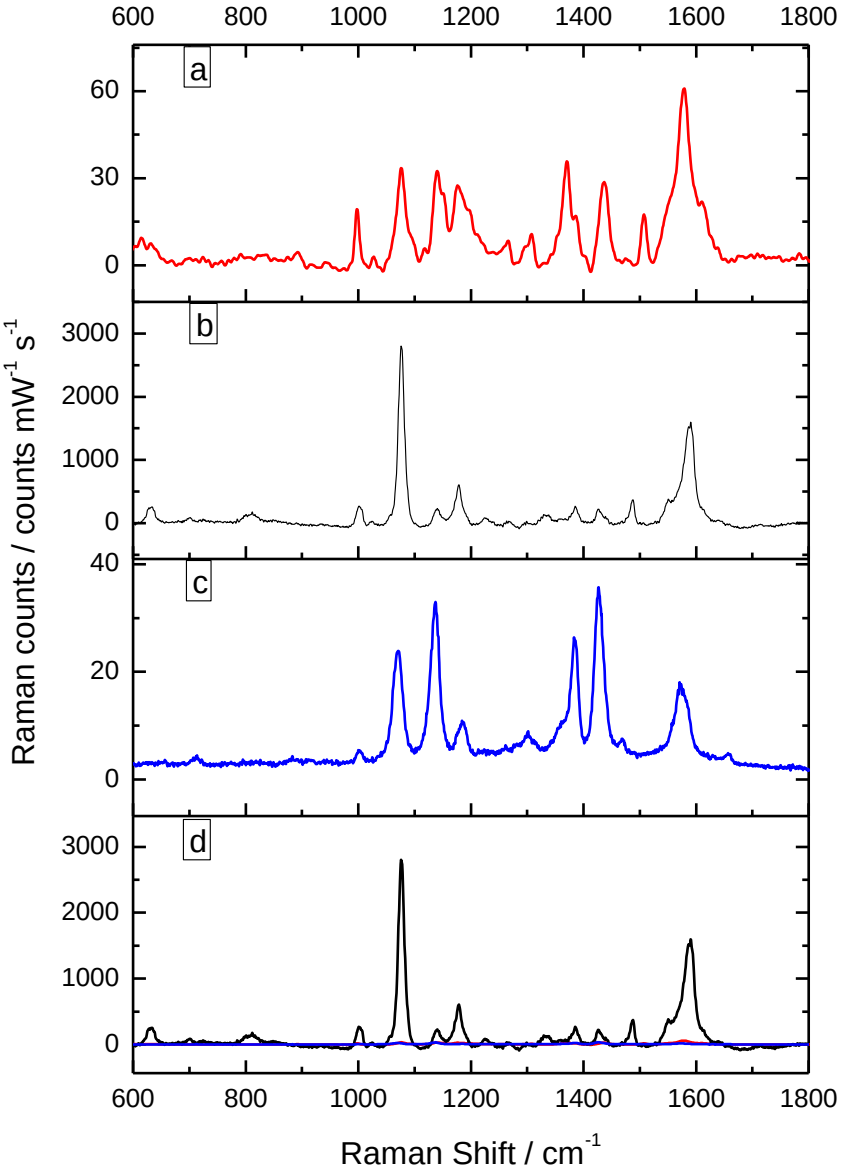

Figure 5-4 – SERS spectra of a) MA on SSV, b) MA-NP assembly on SSV, c) MA-NP on flat Au and d) all three on the same scale. Spectra were taken with a variety of acquisitions and have been normalised to counts mW^{-1} s^{-1}.

The spectrum of MA (see Figure 5-4) is dominated by a strong peak at 1590 cm^{-1} which corresponds to the 8a mode (a ring breathing mode). The SERS spectrum of

MA has been extensively studied previously [11-13], and a full band assignment is given in Table 5-1. The ring breathing and stretching modes at 1001, 1076, 1177, 1386 and 1425 cm^{-1} (corresponding to the 18a, 7a + *ν*(C-S), 9a, 3 and 19b modes respectively) are all strong in the spectrum.

The formation of the SSV-MA-NP adduct results in a substantial increase in the SERS intensity. This increase in intensity is attributed to a very strong localised electric field present between the nanoparticle and the surface, and this explanation is borne out by the relative peak heights within the enhanced spectrum.

Table 5-1 – Band assignments for MA on Au SSV[13]

Peak centre / cm^{-1}	**Assignment**	Enhancement mechanism [12]
632	12 (a_1)	
1001	18a (a_1)	
1076	7a *ν*(C-S) (a_1)	EM
1140	9b (b_2)	CT
1177	9a (a_1)	
1332	14 (b_2)	
1386	3 (b_2)	CT
1425	19b (b_2)	CT
1487	19a (a_1)	
1562	8b (b_2)	CT
1590	8a (a_1)	EM

The SSV-MA-NP spectrum is dominated by two bands at 1076 and 1590 cm^{-1}, which are attributed to the 7a + *ν*(C-S) and 8a stretches. Both these bands have a_1 symmetry and have been shown by Osawa *et al.* [12] to be strongly dependant on EM enhancements. The rest of the spectrum is still enhanced relative to the unmodified MA spectrum, but the other ring breathing modes (which are attributed to the CT mechanism) are now of comparable intensity to the ring-twisting and deformations (which had a low intensity in the original spectrum).

Interestingly, the underlying SSV structure seems to play an important role in this enhancement, as can be seen by comparison to the spectrum obtained for the NP on flat Au (FG). Figure 5-4c shows the spectrum of FG-MA-NP, and it is clear that the

ratio of peaks has changed. The EM enhanced bands are very small and the CT bands (at 1140, 1386, 1425 and 1562 cm^{-1}) [12] dominate the spectrum. The enhancement in this case is therefore attributed to a charge transfer from the NP into the LUMO of the MA. It is worth noting that no spectrum was observed on FG without an adsorbed NP at the same scan settings, and therefore no direct comparison can be made.

The difference in peak ratio and spectrum intensity between the SSV and FG sections of the NP modified substrate clearly show that the structured surface affect the magnitude and type of the enhancement. Reflectance measurements taken before and after adsorption of the NPs can be seen in Figure 5-5.

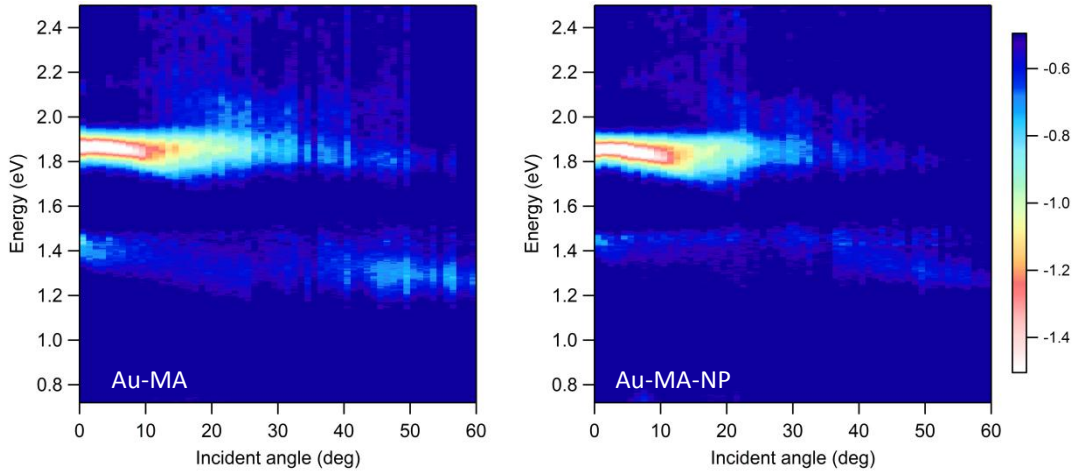

Figure 5-5 – Reflectance maps of 600 nm 0.75 *d* Au SSV substrate with a monolayer of MA and after further modification with Ag NPs.

The reflectance maps show little change to the plasmonics after addition of the NPs, however if the absorption across 1.85 eV is plotted vs angle of incidence, (see Figure 5-6) then a slight change does become apparent. There is a slight shift of the Mie part of the mode to a broader angle of incidence and a stronger absorption at 45° (although this absorption is still much weaker than that at ~15°).

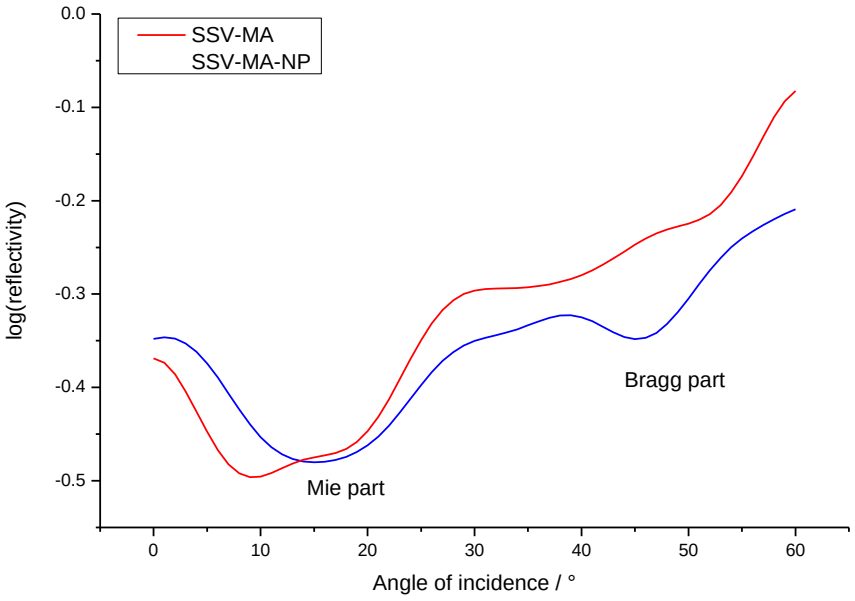

Figure 5-6 - Plot of log(reflectivity) vs angle of incidence for 600 nm 0.75 *d* Au SSV with a layer of adsorbed MA and after modification with NPs taken from the reflectance maps in Figure 5-5 across 1.85 eV

The lack of any drastic change to the plasmonics is most likely explained by a fairly low coverage of the NPs, despite the favourable interaction of the N and the Ag. Stripping voltammetry was performed as described in the literature [14]. The Ag NP modified substrate was placed in a N_2 purged solution of 0.5 M KNO_3 and the resulting cyclic voltammogram (see Figure 5-7) shows a broad feature corresponding to NP stripping between 0.25 and 0.65 V vs SCE (highlighted in blue).

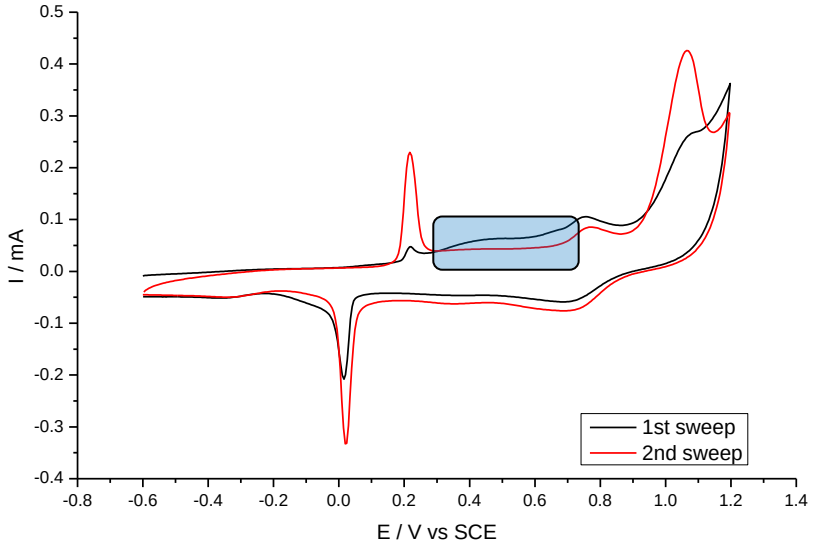

Figure 5-7 – Cyclic voltammogram of Ag NP modified Au SSV substrate in 0.5 M KNO_3 with a scan rate of 100 mV s^{-1} and a scan range of -0.6 to 1.2 V vs SCE. The stripping feature is shown by the blue box.

The voltammetry gives a stripping charge of 460 µC cm^{-2} which, assuming a NP size of 18 nm, gives ~ 4.8 x10^{9} NP cm^{-2} (given a molar volume for Ag of 10.27 cm^{3} mol^{-1}). A 1 cm^{2} area of substrate is made up of 3.5 x 10^{8} voids; the loading is therefore 158 NPs per void. The area under one NP is 2.54 x 10^{-12} cm^{2}, which means that 3.8% of the substrate is covered by NPs. Given an increase that the spectrum is increased by x83, this gives an additional enhancement factor of 2x10^{3} over that obtained on the SSV substrate in the absence of the NP.

This low loading inevitably leads to the formation of hotspots commonly associated with colloidal or rough substrates [15], and a loss of the uniformity normally evident on SSV substrates [16]. Multiple spectra taken at various points on a modified SSV-MA-NP substrate show a large variability in the enhancement (see Figure 5-8). The maximum and minimum peak heights (for the band at 1142 cm^{-1}) were 5545 and 459 counts mW^{-1} s^{-1} respectively, with a mean of 2301 ± 1560 counts mW^{-1} s^{-1} (the error comes from the standard deviation, and equates to 67% variability). The spot size for this experiment was 0.51 µm in diameter, and therefore an average of only one void was sampled per spectrum.

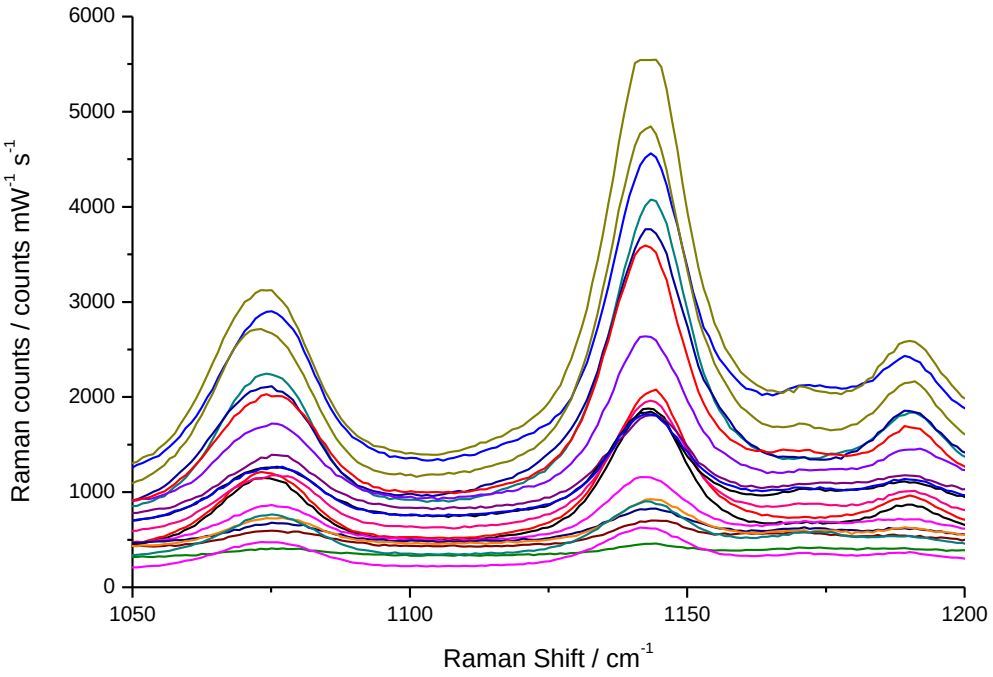

Figure 5-8 – SERS spectra of MA-NP adduct on a 600 nm 0.75 *d* Au SSV substrate taken with a 10 s static scan centred at 1300 cm^{-1}, with a 633 nm HeNe laser at 3 mW power and a X50 objective with a NA of 0.75, and spot size of 0.51 µm

However, when a number of voids are sampled at once, (using an objective with a spot size of 32.1 µm diameter, which means up to 20 voids were illuminated simultaneously) the results vary much less (see Figure 5-9). In this case the maximum and minimum peak heights (for the band at 1142 cm^{-1}) were 2188 and 1379 counts mW^{-1} s^{-1} respectively, with a mean of 1660 ± 217 counts mW^{-1} s^{-1} (13% variability).

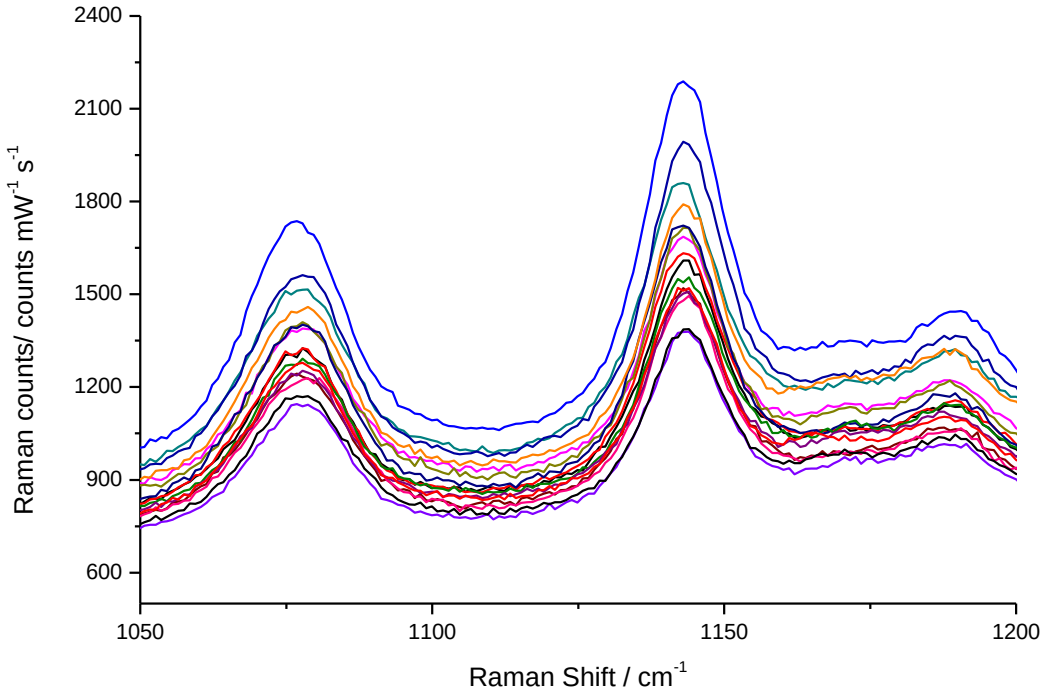

Figure 5-9 – SERS spectra of MA-NP adduct on a 600 nm 0.75 *d* Au SSV substrate taken with a 10 s static scan centred at 1300 cm^{-1}, with a 633 nm HeNe laser at 3 mW power and a X5 objective with a NA of 0.12, and spot size of 35.1 µm

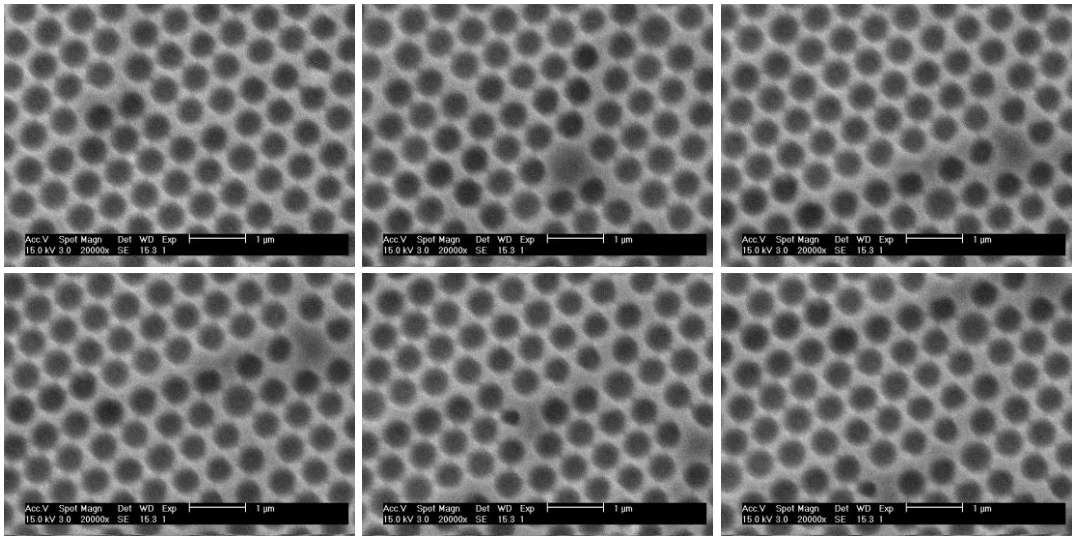

Figure 5-10 – Scanning electron micrographs of a MA-NP modified substrate used in Figure 5-8, the scale bar is 1 µm

The variation of peak height observed with the larger spot size is comparable to that obtained with unmodified SSV substrates [16]. The much larger variation observed with a smaller spot size can be ascribed to the non-uniformity of the arrangement of NPs on the surface.

Scanning electron micrographs of the NP modified substrate (see Figure 5-10) show that there is little or no variation in the surface topography of the substrate. This means that the differences in spectral intensity must be accounted for by the variation in NP density of the voids and not the substrate. Neither the NPs themselves or aggregations of them can be seen, again confirming that the enhancement must be from the electric field footprint of isolated NP adducts.

5.1.3 Mercaptobenzoic acid

Further proof that the enhancement comes from an EM mechanism over CT lies in changing the type of bond between the adsorbate and the NP, as CT enhancements are highly specific to the chemical nature of the interaction.

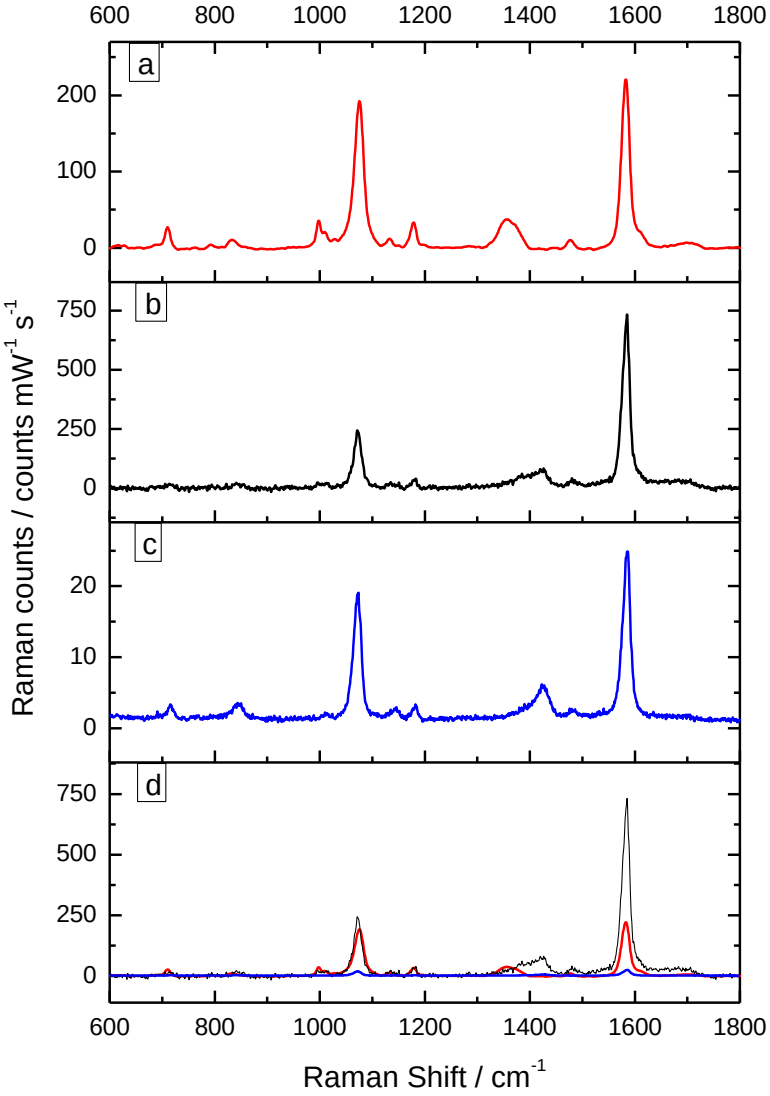

Figure 5-11 – SERS spectra of a) MBA on SSV, b) MBA-NP assembly on SSV, c) MBA-NP on flat Au and d) all three on the same scale. Spectra were taken with a variety of acquisitions and have been normalised to counts mW^{-1} s^{-1}.

In this case, the amine group of the MA was replaced with a carboxylic acid in mercaptobenzoic acid (MBA). The spectrum (see Figure 5-11) is dominated by two ring breathing modes, attributed to the 12 and 8a [17, 18] modes. There is also a very

broad band at 1362 cm^{-1} attributed to the $\nu_s(COO^-)$ stretch, and a smaller feature caused by the γ(CCC) mode. There is some debate as to the exact origin of the other bands, but Michota *et al.* [18] suggest that they may be caused by decarboxylation of the acid, resulting in some benzenethiol on the surface.

The addition of the NPs to the assembly does once again result in an increase in the intensity of the spectrum, although a much smaller increase than on the MA system. The two ring breathing modes (both from the EM mechanism [12, 18]) are enhanced, and there is a significant shift in the $\nu_s(COO^-)$ band (from 1362 to 1426 cm^{-1}), which confirms the presence of the COO-NP interaction. The CT enhancement is not as obvious as in the MA case, but the presence of the band at 846 cm^{-1} due to $\delta(COO^-)$ (not seen in the SSV-MBA or SSV-MBA-NP spectra), suggests that the CT enhancement is still present.

The difference in the magnitude of the additional enhancement between the MA and MBA modified substrates can be accounted for by the relative concentration of NPs. The MA substrate showed 158 NPs per void, whilst the stripping voltammetry on the MBA surface gave a charge of just 0.12 mC cm^{-2}, which equates to 9.1×10^7 NP cm^{-2}, and hence only 41 NPs per void. This equates to a coverage of just 0.9%, which gives an additional enhancement of 3.7×10^2.

This value is 10 times less than that obtained with the MA, a difference that can be explained by the nature of the adsorbate-NP interaction. Ag is a soft metal and the aniline is a borderline-soft base [19] so the interaction is strong, whilst the carboxylate is more of a hard base, so the interaction is weaker. Whilst this is partially accounted for in the lower loading of NPs on the MBA substrate, it is also likely that the particle will be held further from the surface, resulting in a smaller enhancement of the electric field, and, therefore the SERS.

5.1.4 Cysteamine

The benzene ring present in both MA and MBA is highly polarisable, and hence is a very strong Raman scatterer with a large cross section. It is therefore expected that a good SERS spectrum should not be difficult to obtain using such an adsorbate.

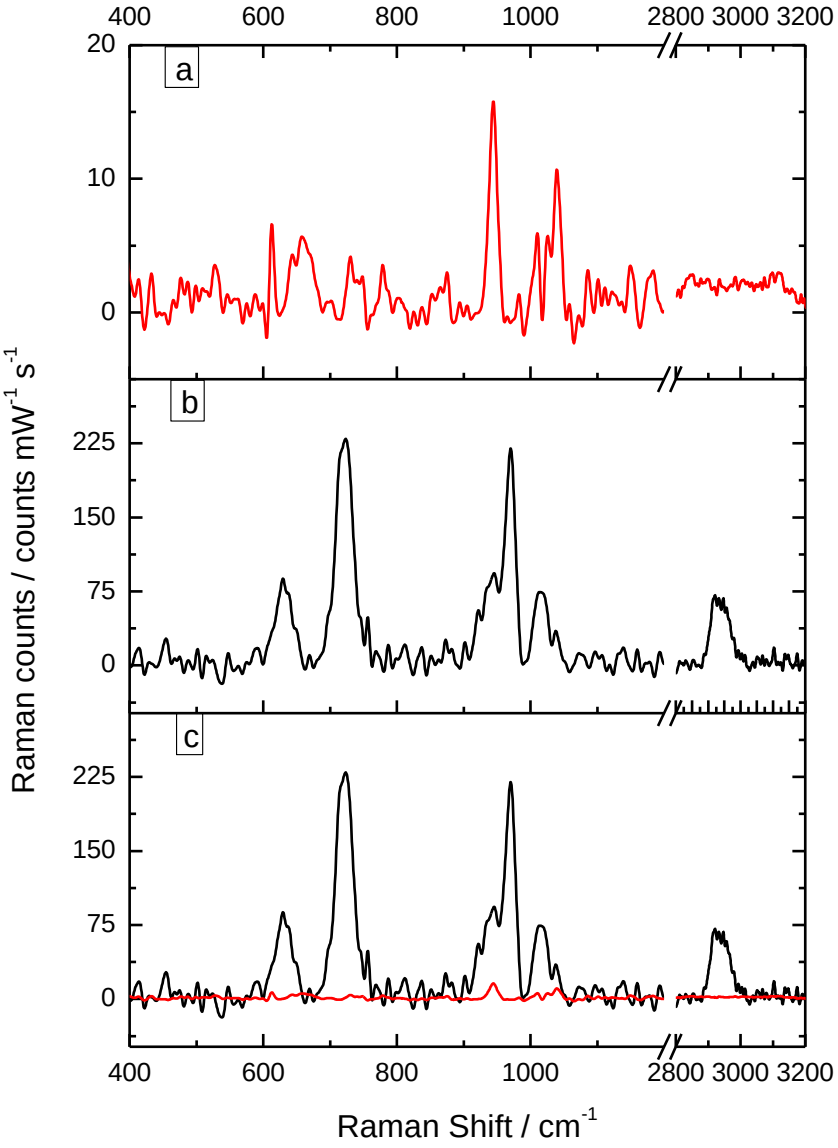

Figure 5-12 – SERS spectra of a) cysteamine on SSV, b) cysteamine-NP assembly on SSV and c) all three on the same scale. Spectra were taken with a variety of acquisitions and have been normalised to counts mW^{-1} s^{-1}.

To test the NP induced enhancement with a more challenging system, cysteamine was used as the linker, as it has the primary amine group present in MA (shown to

have a reasonable loading of NPs and excellent enhancement), but is a relatively poor Raman scatterer. The SERS spectrum of cysteamine on the SSV is lower quality than that of MA, with a reduced signal to noise ratio. However, it is possible to assign the peaks observed to a mixture of gauche and trans cysteamine on the surface (see Figure 5-12). The broad feature at 663 cm^{-1} corresponds to the ν(C-S) mode for gauche cysteamine, and the peaks at 940 and 1036 cm^{-1} are attributed to the ν(C-C(-N)) modes of trans cysteamine [20]. The various ν(C-H) modes (at 2870 and 2925 cm^{-1} in the literature) are not observed in the SSV spectrum.

The addition of Ag NPs to the system once again results in a much stronger spectrum, with a much improved signal to noise ratio. The intensity of the ν_{trans}(C-C(-N)) peaks are greatly increased, and the ν_{trans}(C-S) band at 722 cm^{-1} is present after formation of the Cysteamine-NP adduct (in fact, this becomes the strongest band in the whole spectrum). There is evidence of the gauche conformation however, as the ν_{gauche}(C-S) band is still present but shifted to 625 cm^{-1}. The ν_{as}(C-H) feature is also present in the NP modified substrate. The FG-Cysteamine-NP spectrum showed no bands at all, and has been omitted for clarity.

Electrochemical stripping shows a stripping peak of 120 µC cm^{-2} which equates to 40 NPs per void, or a 0.9% coverage. Accurate determination of the additional enhancement of the spectrum is difficult, given that a change of orientation occurs, however using the ν(C-S) peak at 663 and 625 cm^{-1} the enhancement factor is 1.6×10^3, a value very similar to that on MA. This is expected as both cysteamine and MA involve amine-Ag interactions, which form a stronger bond to the NP than the MBA carboxylate-Ag equivalent.

5.1.5 Calculations

Calculations performed by our collaborators in Cambridge predict an enhancement in the ^{0}D plasmon mode [21] with the addition of the NP. The calculation is based on Mie theory and predicts a variety of plasmon modes [21]. Two of the modes are shown in Figure 5-13, namely the ^{0}D and ^{0}P modes, located in the centre of the void. The ^{0}D mode is found close to the surface, whilst the ^{0}P mode fills most of the void, and couple to incoming radiation of ~550 and ~750 nm respectively.

The addition of NPs to the substrate shows a large increase in the intensity of the absorption of the ^{0}D mode (see Figure 5-13). This is strongly localised to the centre

of the void, where the NP has been arbitrarily located. It is worth noting, therefore, that these calculations only cover one of many possible situations, particularly as in the case of MA, where an average of ~100 NPs resides in each void. An increase is also observed for the intensity of the ^{0}P absorption, although not as strong as that for the ^{0}D mode. A mode corresponding solely to the NP is also observe at ~350 nm over 15-40° angle of incidence, however this is not taken into consideration for this enhancement as it is too far removed from the excitation wavelength used in this work.

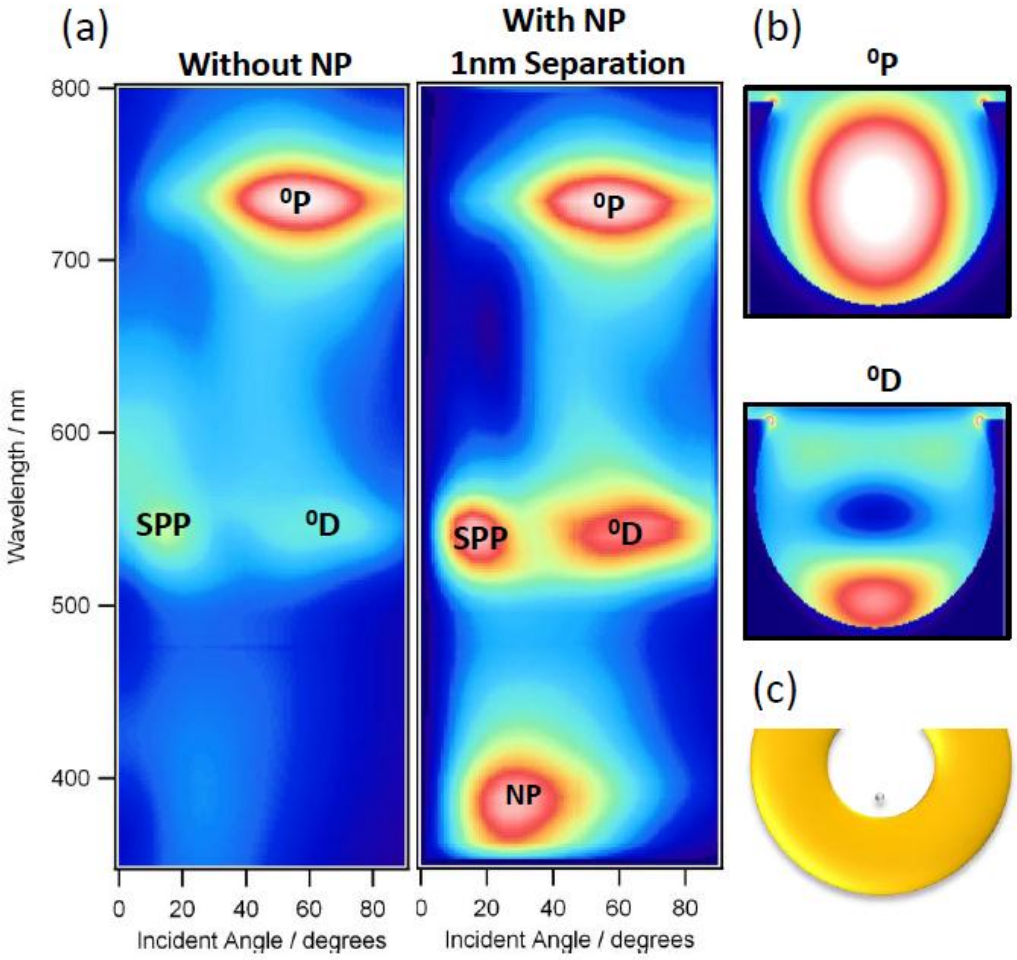

Figure 5-13 – (a) Calculations of the plasmon modes of a 0.75 *d* 600 nm Au SSV substrate, (b) schematic of ^{0}P and ^{0}D modes from Mie theory, (c) schematic of positioned NP

The effect of field enhancement of the plasmon modes was calculated with a varying distance between the Ag NP and the surface of the void. The field was calculated for a constant point, at the centre of the void and 0.25 nm from the surface of the substrate.

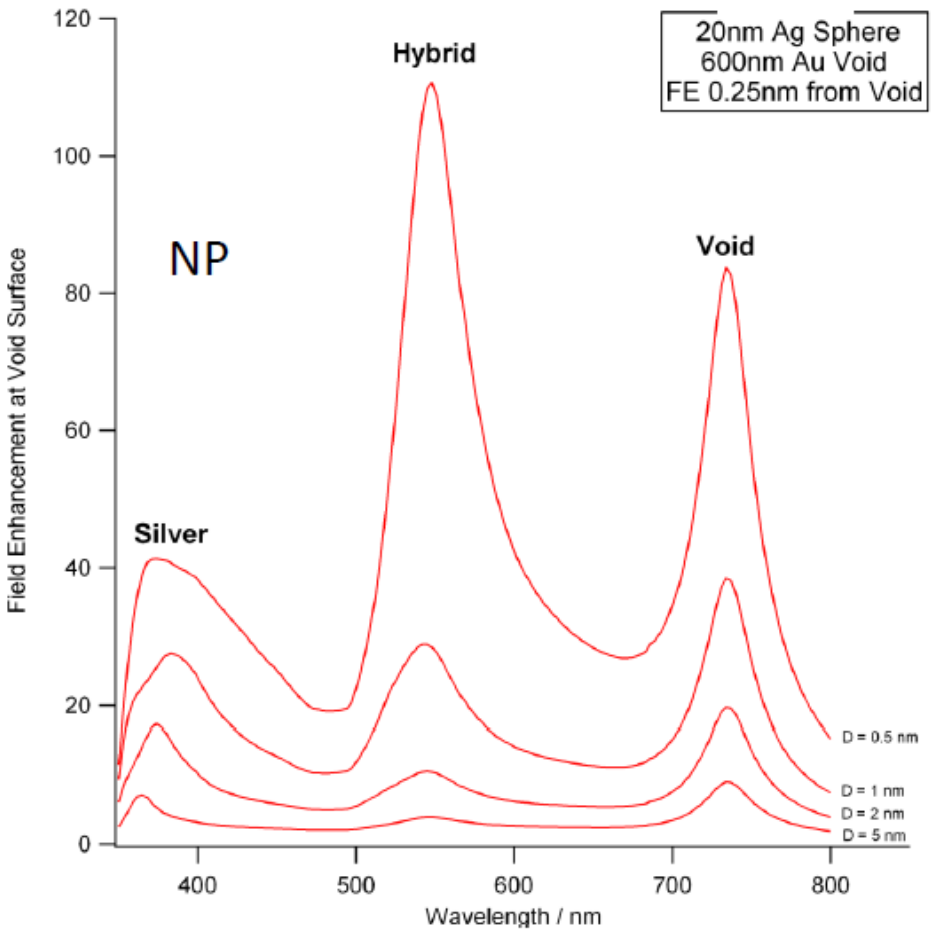

Figure 5-14 – Calculated enhancement of the plasmon modes on a 600 nm 0.75 *d* Au SSV substrate with decreasing distance between a 20 nm diameter Ag NP and the surface of the Au

The effect is very strongly linked to the distance between the nanoparticle and the surface of the substrate, as can be seen in Figure 5-14. The smaller the distance between the NP and the surface, the stronger the enhancement. Other calculations have suggested that the enhancement is proportional to the size of the particle, with a maximum enhancement offered by a diameter of ~50 nm.

5.1.6 Au colloids

The NP induced enhancement is not limited solely to Ag colloids, as is demonstrated in Figure 5-15. The substrate was prepared as above, then allowed to soak in commercially available Au colloid solution (Sigma Aldrich, ~0.01% $HAuCl_4$, 17-23 nm particle size) for 2 hr, then washed with water and ethanol (as above).

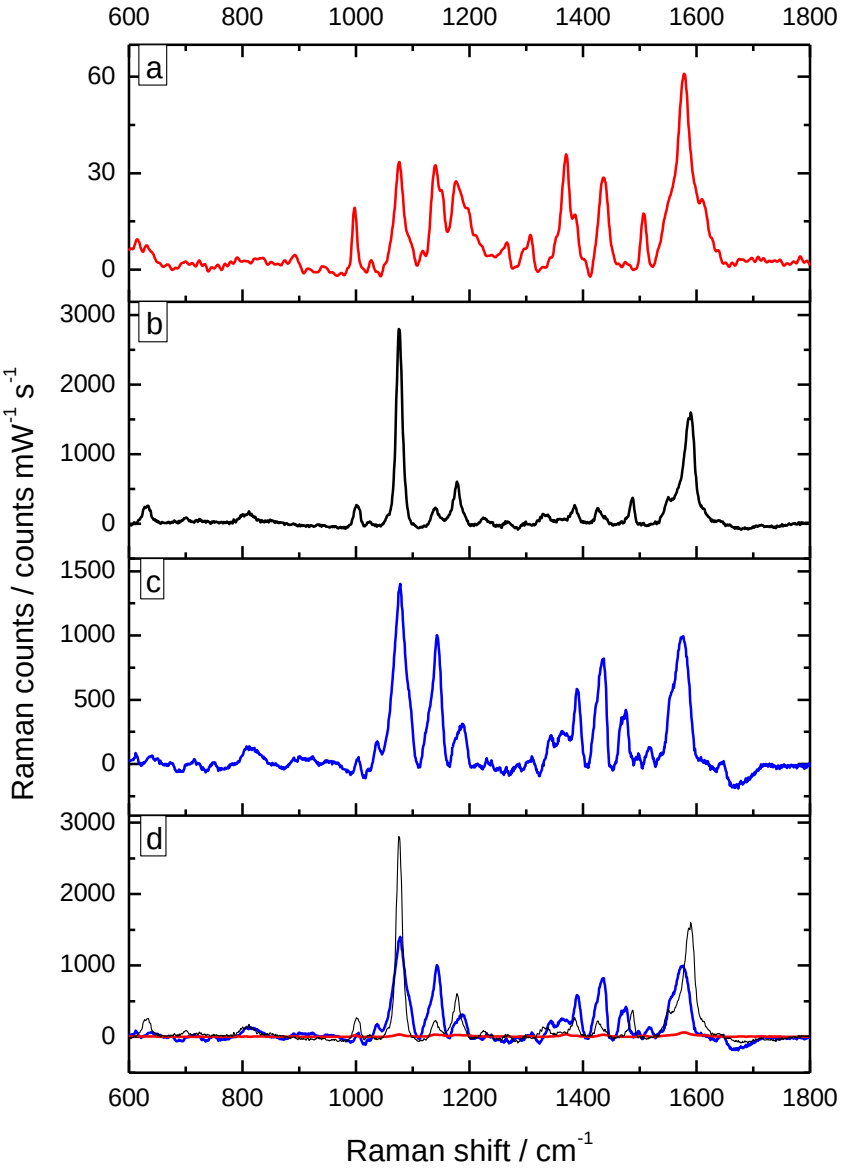

Figure 5-15 – SERS spectra of a) MA on SSV, b) MA-AgNP assembly on SSV, c) MA-AuNP assembly on SSV and d) all three on the same scale. Spectra were taken with a variety of acquisitions and have been normalised to counts mW^{-1} s^{-1}.

The enhancement is weaker than before with a maximum intensity of 1500 counts mW^{-1} s^{-1} (as opposed to 3000 counts mW^{-1} s^{-1} for Ag), and this is probably due to a weaker EM field between the particle and the substrate. An alternative explanation may arise from a lower loading of Au NPs, as the N-Au bond is not as strong as N-Ag, but the ratio of peaks within the spectrum refutes this. The EM band at 1076 cm^{-1} is still the strongest band in the spectrum, and the 1590 cm^{-1} band has the characteristic shape of the EM band (non-enhanced shows a shoulder at

higher frequency, whilst the EM enhanced shoulder is lower frequency due a change in the ratio of the two close bands). However the rest of the bands are comparable in intensity, showing that the CT enhancement is equally as important to the spectrum.

Similar calculations to those for Ag (see 5.1.5) were also performed for Au and they showed only a small enhancement for a 20 nm Au NP in a 600 nm SSV void. The maximum theoretical enhancement is expected to be observed on a 750 nm void (again with 0.75 *d*).

5.1.7 Mercaptopyridine with Ag NPs

One of the prerequisites for a high loading of NPs on the substrate is a N-Ag interaction in the assembly. Ideally this comes in the form of a primary amine, (such as MA used above), as anything else starts to introduce steric hindrance.

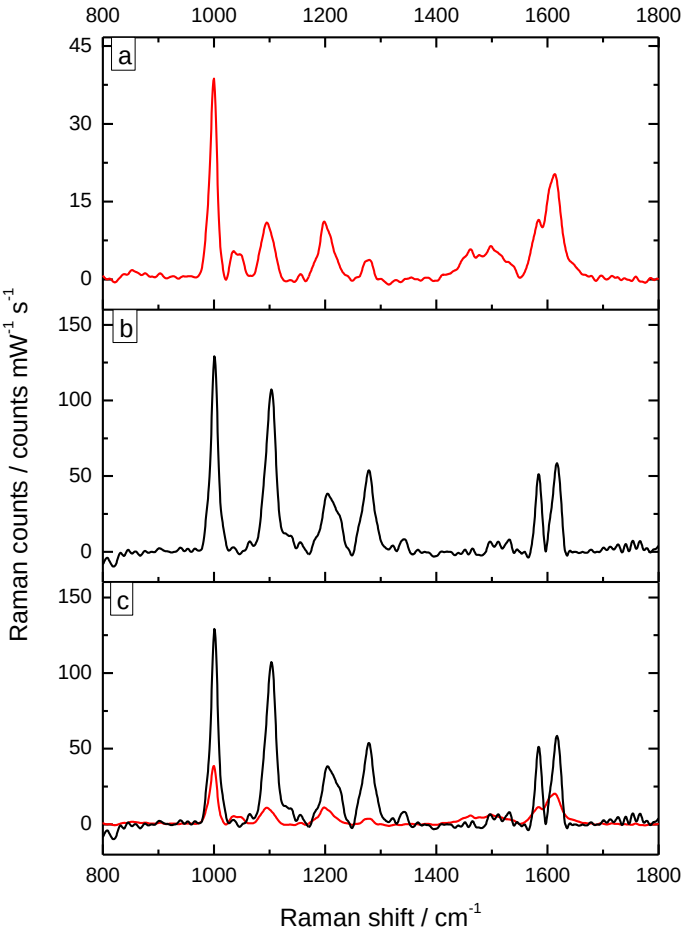

Figure 5-16 - SERS spectra of a) MP on SSV, b) MP-AgNP assembly on SSV, c) both on the same scale. Spectra were taken with a variety of acquisitions and have been normalised to counts mW^{-1} s^{-1}.

Future studies may wish to incorporate an electrochemical aspect to this experiment, and MA is known to undergo electropolymerisation [22, 23], so mercaptopyridine (MP) was also used in this study. To check that the NP induced enhancement was still evident, a MP modified substrate was soaked in Ag NP solution for 2 hr, and the spectrum acquired (see Figure 5-16).

An additional enhancement is observed, but it is much smaller than on the MA equivalent. The Ag stripping voltammetry showed a much lower coverage, of only 0.2 mC cm^{-2}, which is comparable to the value obtained for MBA. This equates to a loading of only ~80 NPs per void, and gives an additional enhancement of 3.8×10^2.

An assignment [24] of the bands observed is given in Table 5-2, and the most intense band is once again the symmetric ring breathing mode (as in the majority of benzene derivatives). After addition of the NPs the 18a + *ν*(C-S) band becomes a dominant feature as well.

Table 5-2 – Band assignments for MP on Au SSV

Peak centre / cm^{-1}	Assignment
1001	1
1103	18a + *ν*(C-S)
1203	9a
1279	3
1581	8a
1616	8a

This is expected, as both 1 and 18a modes only feature the C-C stretches, whereas the 3 and 9a modes also encompass C-H deformations, which have a smaller polarisability, and hence one would expect less of an enhancement. Jung *et al.* [24] have observed that the position of the 8a band is strongly dependant on protonation of the N in the ring, and so an explanation for the clear splitting of the broad band centred at 1600 cm^{-1} upon modification is most likely due to the presence of both MP and MP-NP on the surface.

5.1.8 Summary

This section has presented a method for increasing the SERS signal from an SSV substrate by a factor of 10^3 through a simple modification with Ag NPs. The enhancement is thought to be electromagnetic in nature, as bands associated with the EM enhancement mechanism are significantly larger in the final spectrum than CT. The enhancement also requires a structured substrate, as on flat Au the spectrum is much lower in intensity, and is dominated by the CT bands.

The enhancement relies on the formation of an adsorbate-Ag NP adduct, and so is proportional to the coverage by NPs. This was calculated from electrochemical stripping in KNO_3 solution. The weaker binding MBA showed less enhancement in the spectrum, but had a much lower loading of NPs too; which, once taken into consideration gave an enhancement factor comparable to MA. The enhancement has also been observed with the weak Raman scatterer, cysteamine. This shows that the enhancement is not limited to molecules with traditionally high Raman scattering cross sections, such as benzene rings, and that it may prove to be applicable to the study of a wide variety of molecules, providing the adsorbate-NP bond is formed.

The NP enhancement effect was also demonstrated on commercially available Au NPs, although with a smaller enhancement. This was explained by calculating the relative enhancements on the substrate, which predicts an increase in the ^{0}D plasmon mode on the substrate. The optimum void diameter for Au was shown to be 750 nm, where a much stronger enhancement is expected to be observed.

5.2 Uses for NP-SSV SERS

The use of NPs in modern science is not limited solely to catalysis, they are being integrated into modern medicine, and have been used for drug delivery [25-28] and as an aid for imaging techniques [29, 30]. Often, they must be coated with either organic coatings, or in the case of drug delivery, the drug itself. SERS is an effective, quick and non-destructive technique for evaluating the efficiency of coating, and also to study NP-biochemical interactions both *in vitro* and *in vivo*.

5.2.1 Drug detection through cysteine

Cysteine is a naturally occurring amino acid, and has thiol, amine and carboxylic acid functionality, which make it perfect for binding to a large number of different compounds, as well as a metal surface. A monolayer was formed by soaking a Au SSV substrate in 10 mM aqueous cysteine solution overnight. As with the molecules used above, cysteine undergoes an enhancement in the presence of Ag NPs, (see Figure 5-17).

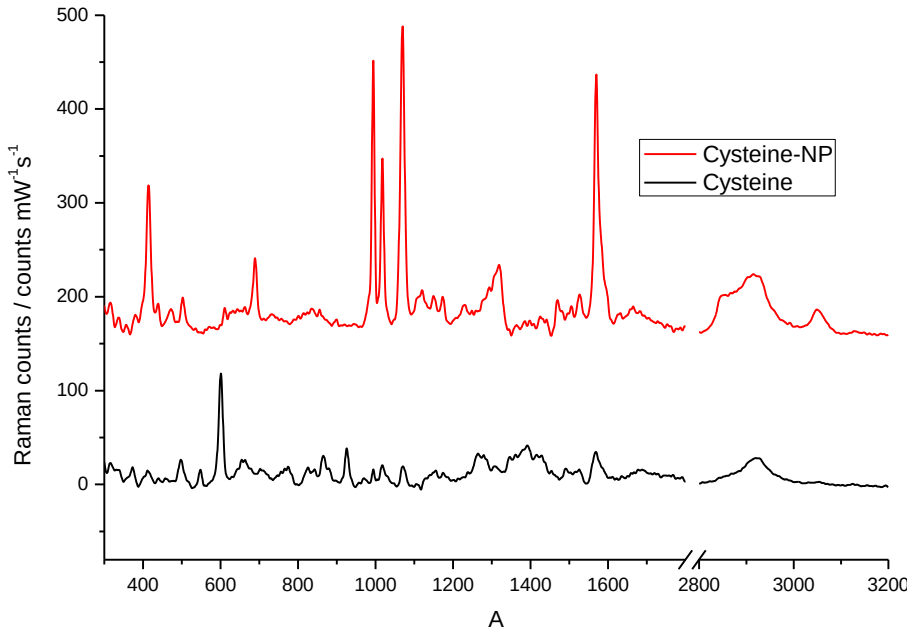

Figure 5-17 – SERS spectra of cysteine with and without Ag NP modification on a 600 nm 0.75 *d* Au SSV substrate, taken with a X50 objective and the spectra have been normalised to counts mW^{-1} s^{-1}

Whilst there is a large difference between the two spectra, the large enhancement seen on previous experiments is not observed here. The band assignments [31] are given in Table 5-3, and are in agreement with a zwitterionic nature of the adsorbate. The unmodified spectrum has only one strong band at 600 cm^{-1}, which corresponds

to a ν(CN) + δ(CCO) mode, and a small band at 925 cm^{-1}, from the ν(C-COO^-) mode. This, coupled with the absence of any ν(N-H) modes suggests an orientation as shown in Figure 5-18, as the central C-C bond lies parallel to the substrate, and the majority of the stretches will not be observed, due to the surface selection rules [32].

Table 5-3 – Major band assignments in cysteine and cysteine-NP adduct

Cysteine bands / cm^{-1}	Cysteine-NP bands / cm^{-1}	Assignment
	415	νNP-Cysteine
600		ν(CN) + δ(CCO)
	688	ν(C-S)
868		δ(HCS)
925		ν(C-COO^-)
994		δ(HCN) + δ(HCH)
	1018	δ(NCH + δ(HCH)
	1070	HCH rock + δ(NCH)
1393		δ(CH_2)
	1569	δ(NH_3^+)
	2846	ν(CH)
2919	2915	ν(CH)
	3047	ν(NH_2)

During the modification process, a zwitterionic exchange can occur between the carboxylic acid and primary amine of the cysteine, causing two different binding motifs in the final adduct. The dominant model seems to be the zwitterion, as indicated by the presence of the strong band at 1569 cm^{-1}, caused by the δ(NH_3^+) mode. It is worth noting that the presence of the ν(NH_2) stretch at 3047 cm^{-1} indicates that not all of the cysteine forms the zwitterion.

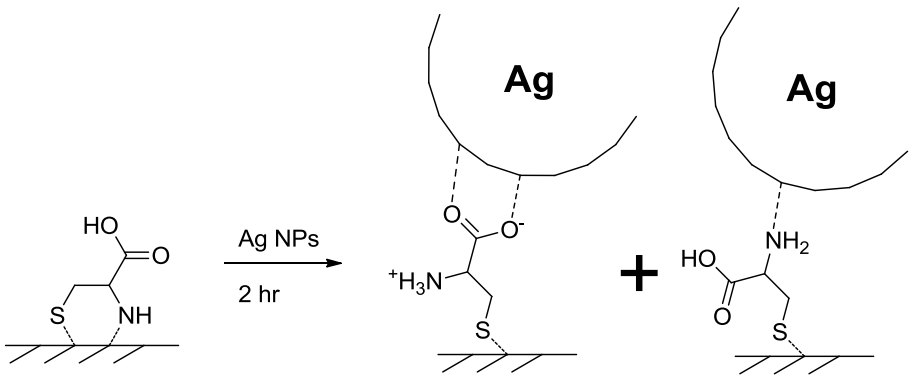

Figure 5-18 – Orientation change of cysteine on a Au SSV substrate with the addition of Ag NPs

The various functional groups in the cysteine molecule can form supramolecular bonds to other organic molecules, holding them close to the surface, for detection *via* SERS. To this end, a cysteine-NP modified SSV substrate was soaked in 10mM aqueous nicotine solution for 15 min, and the Raman spectrum obtained (see Figure 5-19).

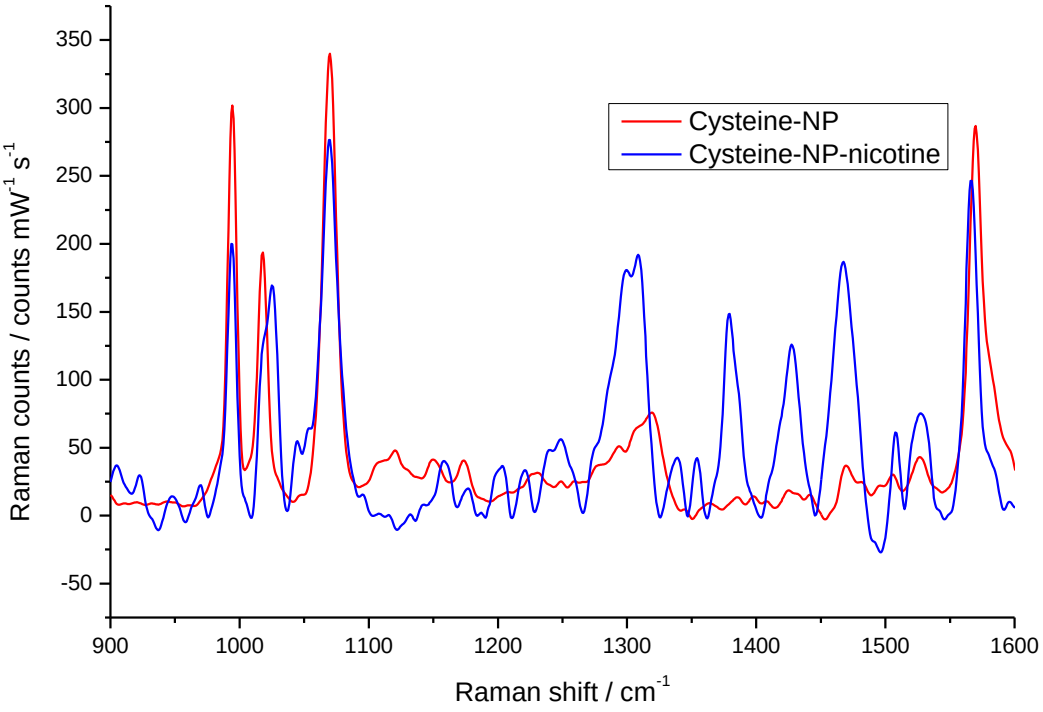

Figure 5-19 – SERS spectra of cysteine-NP with and without the addition of nicotine on a 600 nm 0.75 *d* Au SSV substrate, taken with a X50 objective and the spectra have been normalised to counts mW^{-1} s^{-1}

The appearance of the bands at 1308, 1379, 1428, 1466 and1525 cm^{-1} are all evidence of the insertion of nicotine into the surface. A full assignment of the nicotine bands [33] is given in Table 5-4.

Table 5-4 – Major band assignments for nicotine

Nicotine bands / cm^{-1}	Assignment
1221	CH_2 wag
1246	CH_2 wag
1308	CH_2 twist
1379	Pyridine ring stretch
1428	Ring stretch
1466	Pyridine ring stretch
1525	Ring stretch

The bands from cysteine at 1018 and 1569 cm^{-1} (from the δ(NCH) + δ(HCH) and δ(NH_3^+) modes respectively) are both shifted with respect to the unmodified spectrum. The 1018 cm^{-1} band is red shifted to 1026 cm^{-1},which could be indicative of an obstruction to the δ(NCH) part of the mode, as the presence of the nicotine will result in a steric strain, causing the vibration to shift to a higher frequency. The 1569 cm^{-1} band is blue-shifted to 1565 cm^{-1}, suggesting a donation of electron density into the N-H bond, and resulting a lower frequency *ν*(N-H) mode.

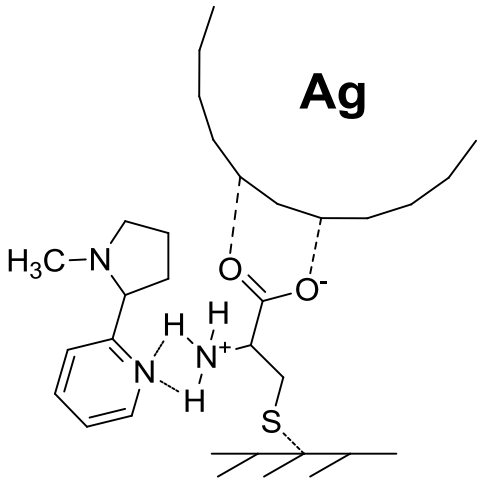

Figure 5-20 – Potential binding motif for the nicotine-cysteine interaction

The fact that only these two bands are altered implies that the nicotine is bound to the cysteine (and not the NPs themselves), and that the interaction is centred on the protonated amine. A possible binding motif is shown in Figure 5-20, where the lone pair of the N in the pyridine ring of nicotine binds the protonated amine of the cysteine.

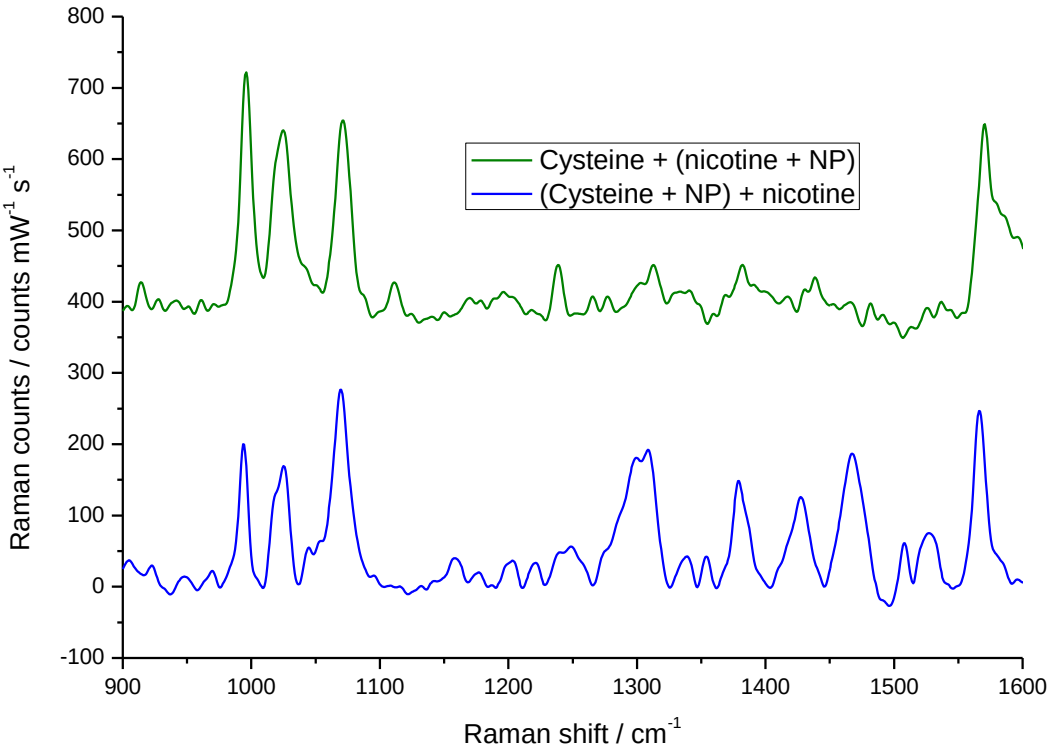

Figure 5-21 – SERS spectra of cysteine + (nicotine + NPs) and (cysteine + NPs) + nicotine on a 600 nm 0.75 *d* Au SSV substrate, taken with a X50 objective and the spectra have been normalised to counts mW^{-1} s^{-1}

To establish that the nicotine is indeed interacting with the cysteine and not the NPs themselves, an alternative assembly method was used, where the nicotine was mixed with the NP suspension first. The nicotine modified NPs were then adhered to the cysteine-modified substrate by soaking for 2 hr, and the spectrum obtained, (see Figure 5-21). The nicotine peaks are clearly only evident when the NPs are adsorbed to the cysteine first, suggesting that the nicotine is not bound to the particle.

The preliminary study in this section has shown that using fairly quick assembly times (of 15 min) the detection of a small organic biologically active molecule is possible using NP enhanced SSV SERS. With careful choice of the initial adsorbate that has a low Raman scattering cross section, as well as potential binding sites for the probe molecule it should be possible to detect much lower concentrations than the 10 mM used in this study.

5.2.2 Analysis of modified NPs

The functionalisation of NPs and then subsequent analysis through SERS has been previously established [34-36], but very little has been shown using a modified NP and a surface. Earlier sections in this chapter have shown that Ag NPs cause a very strong enhancement in the SERS spectra of organic adsorbates lying directly between the NP and the surface. Chapter 3 showed that despite a large increase in plasmonic absorption of the Mie mode, the SERS spectrum of electrochemically reduced diazonium salts (DS) were extremely poor, due to a permanent polarisation inside the molecule. This means that any increased EM enhancement across the adsorbate should not result in an enhancement for the DS, but may lead to an increased spectrum for the molecules adsorbed on the NP.

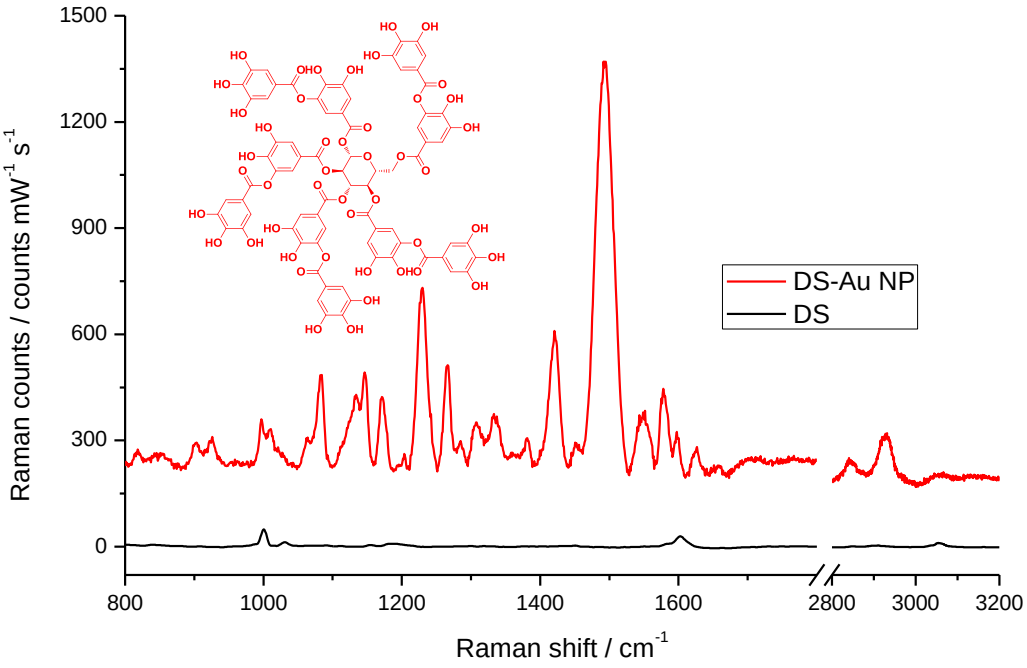

Figure 5-22 – SERS spectra of DS and DS-Au NP (protected with tannic acid and sodium azide) on a 600 nm 0.75 *d* Au SSV substrate, taken with a X50 objective and the spectra have been normalised to counts mW^{-1} s^{-1}, the structure of tannic acid is shown as an insert.

Commercially available (Sigma Aldrich) 20 nm diameter tannic acid and sodium azide protected NPs were adsorbed to a DS modified substrate by soaking for 2 hrs. The SERS spectrum, (see Figure 5-22) shows a fairly strongly enhanced spectrum of tannic acid, which dwarfs any contribution from the previously adsorbed DS. The same NPs were used in Chapter 5 to demonstrate the MA-Au NP enhancement, where the tannic acid was not evident. This implies that the NP-protecting group is

enhanced much less than the SSV-NP linkage adsorbate, and any Raman signal is obscured by the adsorbate itself. Tannic acid has an extremely high Raman scattering cross-section, but is only visible when the adsorbate bound to the SSV substrate has little or no signal of its own (as is the case with DS).

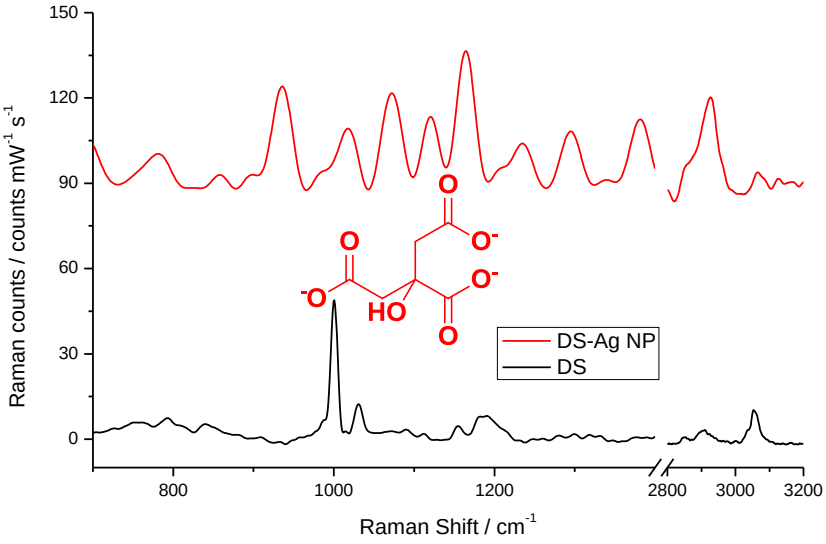

Figure 5-23 – SERS spectra of DS and DS-Ag NP (protected with citrate) on a 600 nm 0.75 *d* Au SSV substrate, taken with a X50 objective and the spectra have been normalised to counts mW^{-1} s^{-1}, citrate is shown as an insert.

In a second experiment, a DS-Ag NP assembly was also fabricated, to probe the spectrum of the citrate used to protect the Ag. The spectrum for citrate (see Figure 5-23) is not as strong or as clear as for the tannic acid on Au NPs, but shows a characteristic $\nu(COO^-)$ band at 1382 cm^{-1} [37] and $\nu(C_4O)$ at 800 cm^{-1}; a full band assignment is given in Table 5-5.

Table 5-5 – Major band assignments for citrate

Citrate bands / cm^{-1}	Assignment
800	$\nu_s(C_4O)$
860	$\nu_s(C_4O)$
935	$\nu_s(C\text{-}C)$
1018	$\nu_s(COO^-)$
1165	$\nu_s(COO^-)$-Ag
1293	$\nu_{as}(COO^-)$-Ag
1381	$\nu_{as}(COO^-)$

The fact that the spectrum of even a relatively poor scatterer such as citrate was obtained from NPs indicates the feasibility of using a NP-SSV array to probe the chemistry of adsorbed species. The formation of a DS modified substrate, however requires the use of highly reactive intermediates, and is not trivial. Even low scattering thiol adsorbates such as cysteamine have been shown to be enhanced by Ag NPs, and the poorly scattering citrate is not observed. However, in the case of Au NPs, which are coated with the strongly scattering tannic acid, it should be possible to observe the NP bound adsorbate over the linker, provided it has a low scattering cross section (such as cysteamine).

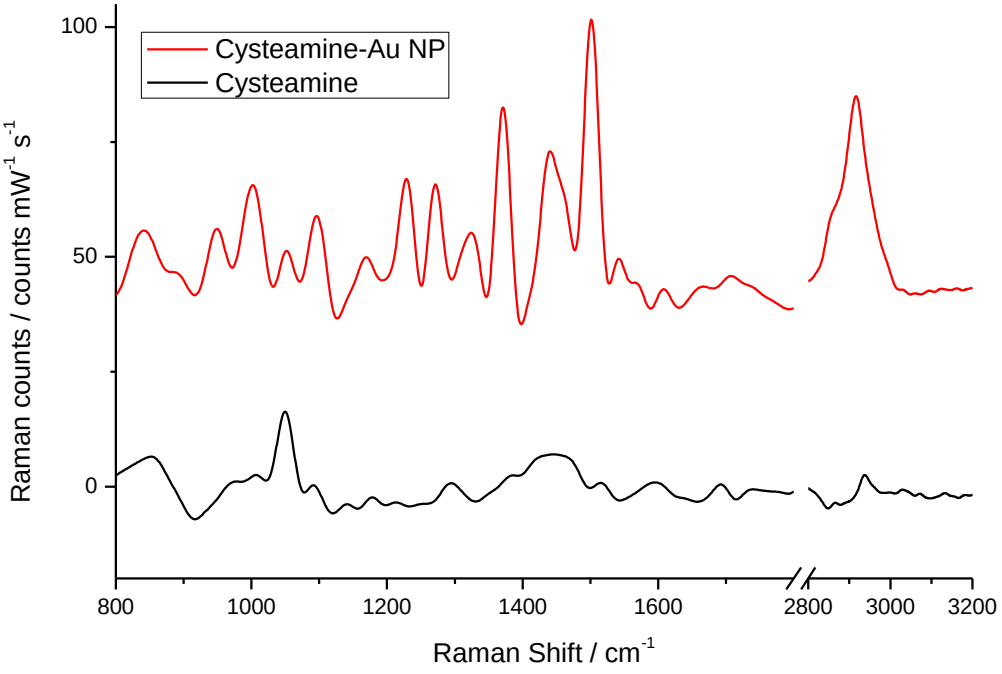

Figure 5-24 – SERS spectra of cysteamine and cysteamine-Au NP (protected with tannic acid and sodium azide on a 600 nm 0.75 *d* Au SSV substrate, taken with a X50 objective and the spectra have been normalised to counts mW^{-1} s^{-1}, citrate is shown as an insert.

In this case, the tannic acid spectrum is once again the main element of the spectrum, with little or no contribution from underlying cysteamine. It is worth noting, however, that whilst the cysteamine-NP system is significantly easier to establish, the maximum peak height for the band at 1502 cm^{-1} is only 50 counts mW^{-1} s^{-1}, whilst with the DS modified substrate this is closer to

1500 counts mW^{-1} s^{-1}. The difference is due to the greater plasmonics on the DS modified substrate (see Chapter 3), and therefore a trade-off exists between facility of assembly and relative enhancement of the structure.

5.2.3 Cis-platin coated NPs

Whilst the detection of adsorbed tannic acid on the surface of a Au NP demonstrates the potential of SSV-NP SERS for the study of NP assisted drug delivery, a much more real world example is the study of an actual anti-cancer drug. A recent paper by Huang *et al.* [38] shows the modification of Au-Au_2S NPs with cis-platin, and the subsequent release of the drug using near IR radiation.

The method was adapted from a procedure by Huang *et al.* [38], whereby citrate protected Ag NPs were collected from the suspension by centrifugation at 10,000 rpm for 15 min, then resuspended in 1 mL of 100 mM aqueous mercaptoundecanoic acid (MUA) solution and incubated at 40°C for 3 days. Excess MUA was removed from the modified NPs by centrifuging the NPs at 10,000 rpm for 10 min and resuspension in water; the washing process was repeated three times. Finally 1 mL of 3.33 mM cis-platin solution was added and the mixture was mixed by sonication for 30 min, before incubation at room temperature for 3 days. The cis-platin modified NPs were then used without any further purification.

The ultimate aim of this experiment is to create artificial lipid bilayers on a SSV substrate and observe the migration of the NP through it, before dissociation of the drug and NP with NIR light. As a simplification for this work, another layer of MUA was deposited onto a SSV substrate from 100 mM aqueous solution overnight. A schematic of the idealised experimental setup is shown in Figure 5-25. The interaction between the amine of the cis-platin and the carboxylic acid of MUA that holds the drug to the NP should also hold the assembly together at the SSV-MUA/cis-platin-MUA-NP interface.

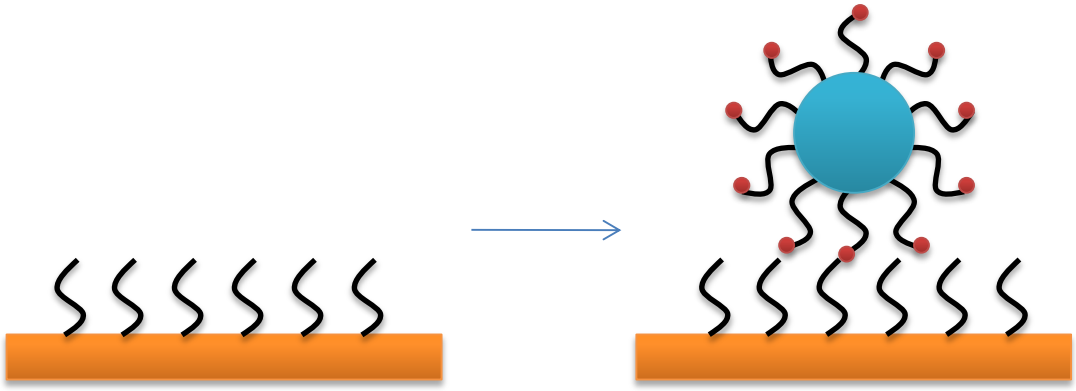

Figure 5-25 – Schematic of cis-platin/NP assembly. The black lines represent MUA, the blue circle is a Ag NP and the red circles are cis-platin molecules

The SERS spectrum of MUA modified SSV (see Figure 5-26) shows a mixture of gauche and trans orientations, as the peaks at 650 and 730 cm^{-1} correspond to the ν_{gauche}(C-S) and ν_{trans}(C-S) modes respectively [39, 40]. A full band assignment is given in Table 5-3.

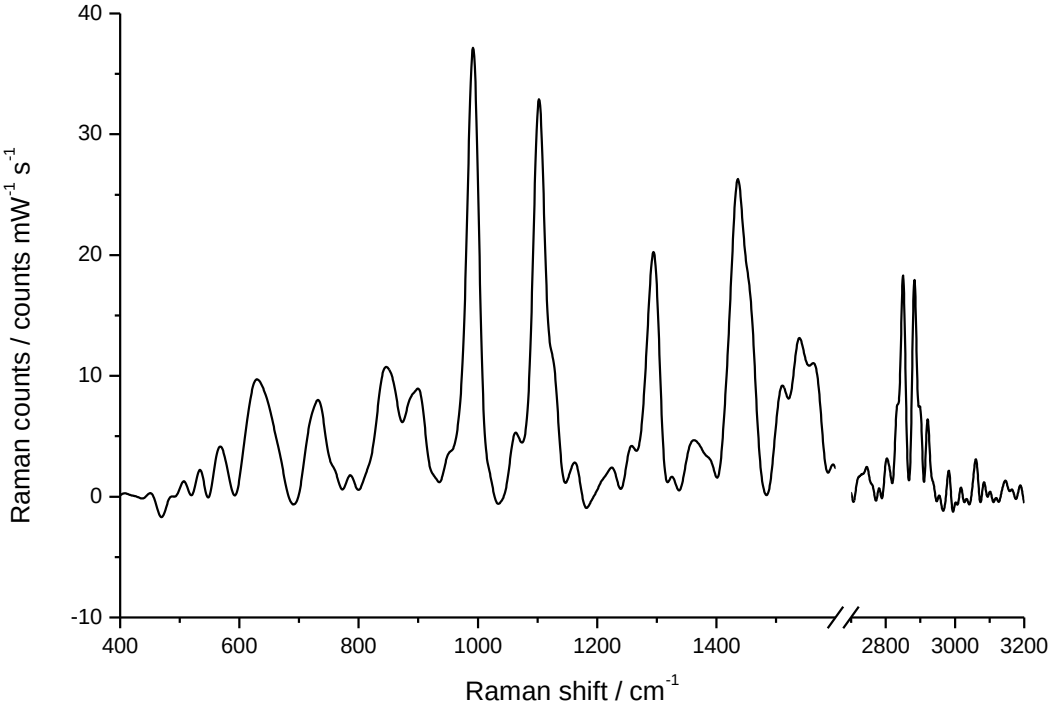

Figure 5-26 – SERS spectrum of MUA adsorbed onto a 600 nm 0.75 *d* Au SSV substrate, taken with a X50 objective and the counts have been normalised to counts mW^{-1} s^{-1}

The strongest bands in the spectra come from the ν(C-COO^-), ν(C-C) and ν(COO^-) bands at 992, 1103 and 1436 cm^{-1} respectively, as would be expected from a predominantly trans configuration. The most probable orientation for the MUA as a

whole is a mixture of trans and gauche conformers at the C_1-C_2 section close to the Au surface with the rest of the chain extending away from the surface; this would be expected due to steric hindrance for any other conformation. The strong ν(C-H) bands present at 2845 and 2883 cm^{-1} are most likely due to the C-H bonds from the C_1 and C_2 gauche molecules, whilst the lower intensity band at 2899 is represents the rest of the C-H bonds within the adsorbate.

Table 5-6 – Major band assignments for MUA on SSV

MUA bands / cm^{-1}	Assignment
650	ν_{gauche}(C-S)
730	ν_{trans}(C-S)
992	ν(C-COO^-)
1103	ν_s(C-C)
1296	δ(C-H)
1436	ν(COO^-)
2845	ν(C-H)
2883	ν(C-H)
2899	ν(C-H)

The spectrum of a MUA-cis-platin modified NP is shown in Figure 5-27. The two strong ν(C-H) bands at 2848 and 2925 cm^{-1} arise from the alkane chain, and the band at 1442 cm^{-1} (slightly blue-shifted from the SSV-MUA) corresponds to the ν(COO^-) stretch. This shift is caused by binding to the cis-platin, as the interaction is between the COO^- and NH_4^+ [41].

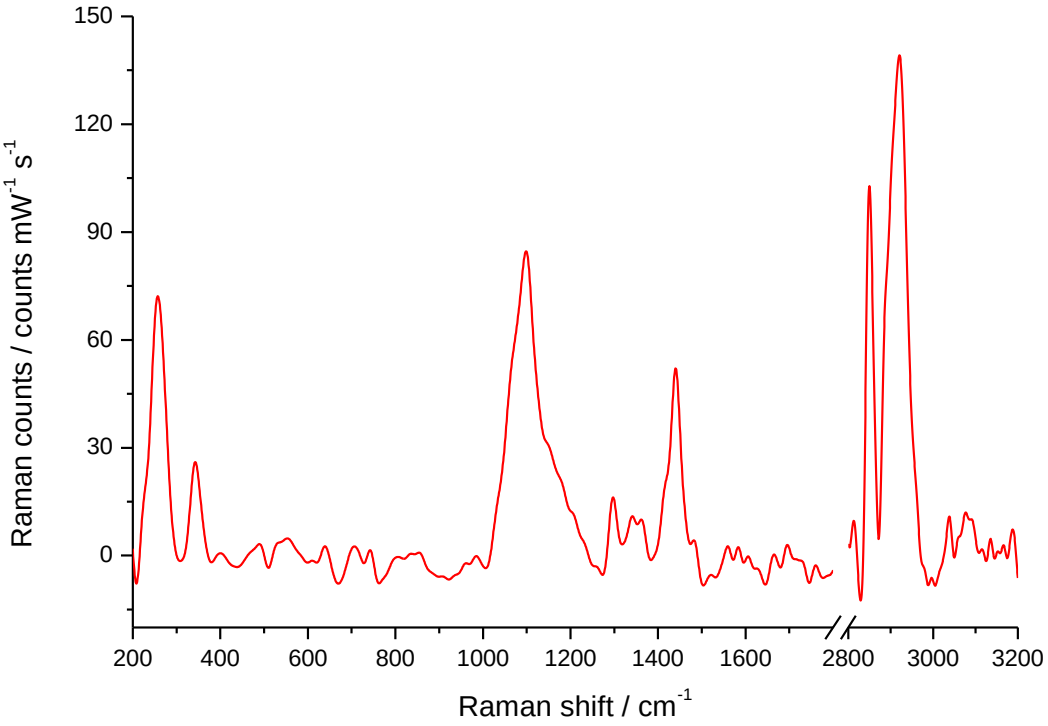

Figure 5-27 – SERS spectrum of MUA-cis-platin modified Ag NPs, taken with a X50 long working distance objective, and normalised to counts mW^{-1} s^{-1}.

A full assignment [42, 43] is given in Table 5-7. The *ν*(C-C) mode seen on the SSV substrate is not as clear in this case, and the *ν*(C-COO^-) band is also not observed either. The broad feature centred at 1095 cm^{-1} accounts for the alkane backbone, and its lack of definition points towards a fairly disordered structure of the MUA adsorbate, with multiple orientations, hence the broad band. This is expected, as on the large comparatively flat SSV surface the monolayer can form a well-ordered structure, however on the much smaller NP the chains are forced into a variety of angles with much less structure.

Table 5-7 – Major band assignments of MUA-cis-platin modified NP

MUA-cis-platin bands / cm^{-1}	Assignment
258	ß(N-Pt-N)
348	*ν*(Pt-Cl)
1095	*ν*(C-C) from MUA
1299	δ(NH_3)
1442	*ν*(COO^-)
2848	*ν*(C-H)
2925	*ν*(C-H)

The most characteristic bands for the cis-platin are the ϐ(N-Pt-N) and *ν*(Pt-Cl) bands at 258 and 348 cm^{-1} respectively. The observed frequency and strength of the ϐ(N-Pt-N) – in-plane bending mode – indicates that the cis-platin is bound to the MUA through only one of the amine groups. If both amine groups were bound then this mode would be highly perturbed away from the literature value [42], and one would expect the intensity to decrease. The *ν*(Pt-Cl) band indicates that the structure of the cis-platin remains intact through binding to the MUA.

The surface modification process on the Ag NPs caused aggregation, which whilst good achieving colloidal SERS greatly decreases the rate of adsorption onto the SSV surface. In previous cases the surface was left for only 2 hr to form a NP adduct, but for this experiment the substrates were soaked for 72 hr to ensure the maximum coverage of NPs.

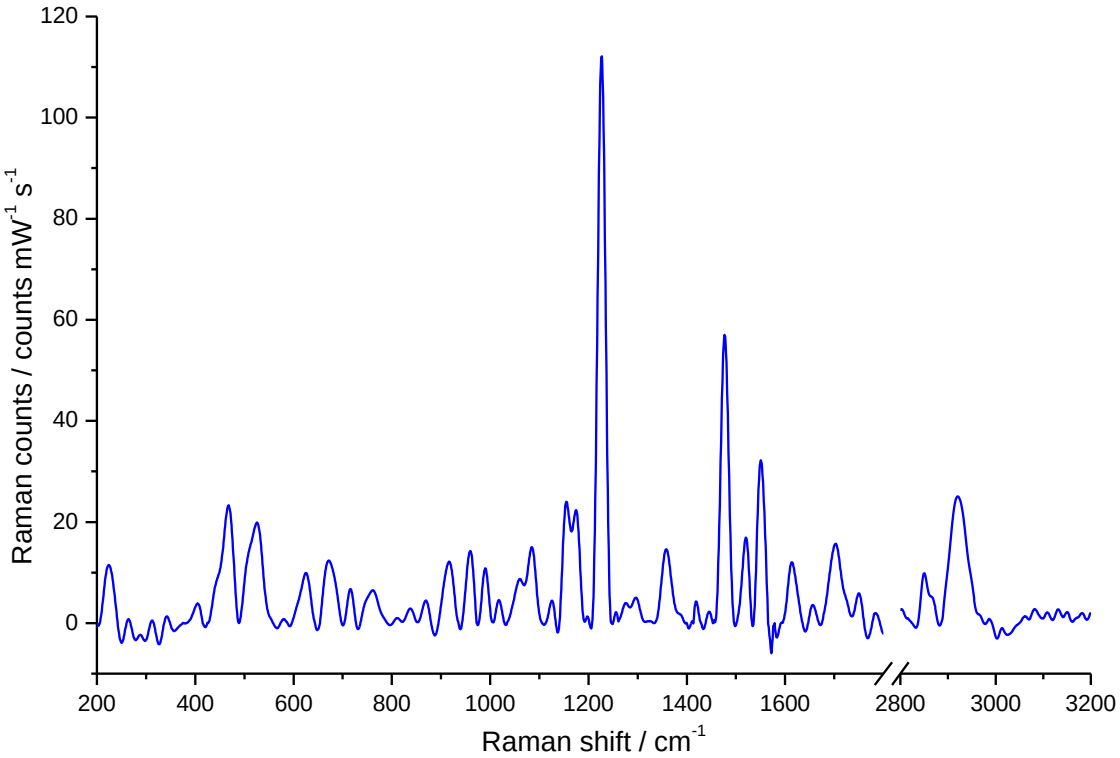

Figure 5-28 – SERS spectrum of MUA-(MUA-cis-platin NP) formed on a 600 nm 0.75 *d* Au SSV substrate, taken with a X50 objective and the counts have been normalised to counts mW^{-1} s^{-1}

The SERS spectrum of the final adduct is shown in Figure 5-28, and shows more bands than either the SSV-MUA or MUA-cis-platin NP. The spectrum shows many

small peaks attributed to a variety of *v*(C-C) modes, but also shows bands characteristic of cis-platin, most notably the large peak at 1223 cm^{-1}, attributed to the $\delta_s(NH_3)$ mode [42, 43].

A full band assignment is given in Table 5-8. There is still evidence of both trans and gauche conformations of MUA, from two different *v*(C-S) bands, and various *v*(C-C) bands at 1085, 1151 and 1173 cm^{-1}. There are also three different bands originating from the COO^- functionality (at 1475. 1518 and 1551 cm^{-1}), most probably due to a mixture of carboxlyates bound and unbound to cis-platin. The *v*(C-H) bands are still observed, and are also indicative of the presence of some gauche MUA, as the orientation of trans C-H bonds lie parallel to the plane of the substrate, and are not allowed by the surface selection rules.

Table 5-8 – Major band assignments for MUA-(MUA-cis-platin NP) assembly [39, 40, 42, 43]

MUA-(MUA-cis-platin) bands / cm^{-1}	Assignment
222	ß(N-Pt-N)
468	υ(Pt-OH)/υ(P-N)
521	υ(Pt-N)
620	υ_{gauche}(C-S)
670	υ_{trans}(C-S)
992	υ(C-COO^-)
1085	υ(C-C)
1151	υ(C-C)
1173	υ(C-C)
1223	$\delta_s(NH_3)$
1359	$\delta_s(NH_3)$
1475	$\upsilon_s(COO^-)$
1518	$\upsilon_{as}(COO^-)$
1551	$\upsilon_{as}(COO^-)$
1613	$\delta_d(NH_3)$
1701	υ(CO)
2847	υ(C-H)
2919	υ(C-H)

The ß(N-Pt-N) mode is clearly evident at 222 cm^{-1}, as is the *v*(Pt-N) stretch at 521 cm^{-1}, indicating the presence of cis-platin. The *v*(Pt-Cl) band at 348 cm^{-1} (in the MUA-cis-platin NP) is not present here, which suggests that the complex has been hydrolysed during the binding process [43]. The band at 468 cm^{-1} may therefore represent a *v*(Pt-OH_2) mode, although this is inconclusive without the presence of any *v*(O-H) features (which are not observed).

The presence of strong δ(NH_3) modes suggest that one of the amine groups of the complex remains unbound, and that the cis-platin is not linked to both the surface and NP simultaneously (see Figure 5-29 A). This is also confirmed by the presence of the ß(N-Pt-N) band, as the in-plane bend would be very constrained if both amine groups were bound simultaneously.

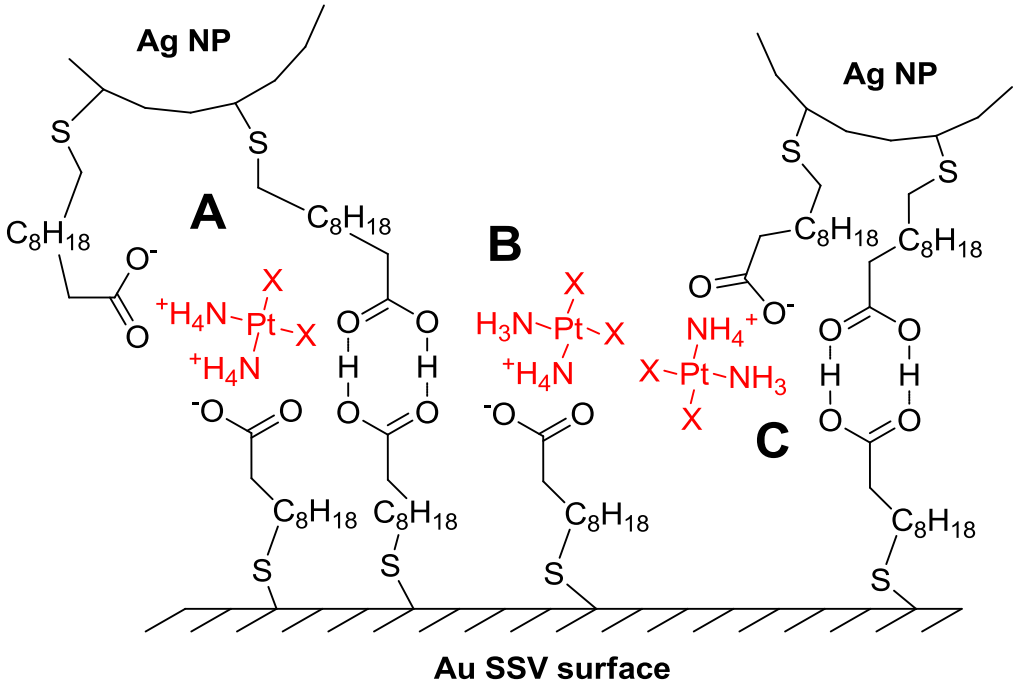

Figure 5-29 – Schematic of potential binding motifs for cis-platin modified NPs on a MUA modified SSV surface through A) an interaction of the cis-platin with the MUA on the surface and NP simultaneously; B) a transfer of the cis-platin from the NP to the surface bound MUA, C) the cis-platin is held close to the surface by an interaction between the surface-bound and particle-bound MUA. The cis-platin is shown in red for clarity, and the X atom represents either Cl or H_2O.

It is possible that the cis-platin molecule is transferred from the MUA surrounding the NP to the monolayer on the SSV surface (see Figure 5-29 B) or that the large number of *v*(C-C) stretches could be indicative of a difference in the structure of the monolayer between the SSV-MUA and this substrate (see Figure 5-26). It is more probable, however, that the new peaks arise from a combination of the MUA on the

NP and on the surface. This strongly suggests that whilst the cis-platin may be transferred from the NP to the surface, the NP is still present close to the surface.

A fourth possibility is that an interaction between the two MUA layers holds the cis-platin close to the surface without altering the original carboxylate-protonated amine interaction present on the NPs (see Figure 5-29 C). This is the most probable orientation, as it leaves an amine group unbound, (hence the strong $\delta(NH_3)$ bands), and holds a NP close to the surface (hence the numerous ν(C-C) bands).

It is worth noting that in this case the NP is used solely as a delivery mechanism for the cis-platin, as no extra SERS enhancement can be obtained from the NPs. This is because the distance between the surface and NPs is much greater with this type of assembly, meaning the localised EM field (and subsequent enhancement) from the surface-NP interaction is very small.

5.2.4 Summary

This section has shown that there are many different uses for NPs other than just enhancing the adsorbate layer. By using a molecule with multiple functionalities (such as cysteine), the detection of a small drug-like molecule has been demonstrated, using relatively fast assembly times. NPs cause an orientation change of the adsorbate, that otherwise may not act as a receptor for the molecule of interest.

Moreover, the detection of stabilisation agents for the NPs themselves has been achieved, by using an SSV substrate modified by an adsorbate with a low Raman scattering cross section. This enables the enhanced spectrum of the NP-adsorbate to come through, and has been extremely effective for the detection of tannic acid protected Au-NPs. The detection of citrate coating of Ag NPs is less effective, however it can be detected. This may be useful in the identification of compounds using NP scavengers, as the NP can bind to compounds of interest in a sample then be added to an SSV substrate for rapid identification.

Lastly the observation of cis-platin adsorbed to a potential drug delivery system has been achieved using MUA. The cis-platin is held close to the Au surface, still bound to the NP ready for release. By creating an artificial lipid bilayer on the surface of the substrate [44] and then releasing the drug using NIR radiation it may be possible

to observe the movement of the drug through an artificial cell membrane, gaining a better understanding of drug delivery.

5.3 References

1. S. Kawata, Y. Inouye and P. Verma, *Nat. Photonics*, 2009, **3**, 388-394.
2. Y. Tanaka, N. N. Nedyalkov and M. Obara, *Appl. Phys. A-Mater. Sci. Process.*, 2009, **97**, 91-98.
3. D.-S. Kim, J. Heo, S.-H. Ahn, S. W. Han, W. S. Yun and Z. H. Kim, *Nano Letters*, 2009, **9**, 3619-3625.
4. B.-S. Yeo, J. Stadler, T. Schmid, R. Zenobi and W. Zhang, *Chemical Physics Letters*, 2009, **472**, 1-13.
5. E. Bailo and V. Deckert, *Chemical Society Reviews*, 2008, **37**, 921-930.
6. B. Pettinger, in *Surface-Enhanced Raman Scattering: Physics and Applications*, Springer-Verlag Berlin, Berlin, 2006, vol. 103, pp. 217-240.
7. T. Dadosh, J. Sperling, G. W. Bryant, R. Breslow, T. Shegai, M. Dyshel, G. Haran and I. Bar-Joseph, *ACS Nano*, 2009, **3**, 1988-1994.
8. W. H. Ke, D. F. Zhou, J. Z. Wu and K. Ji, *Appl. Spectrosc.*, 2005, **59**, 418-423.
9. J. A. Creighton, C. G. Blatchford and M. G. Albrecht, *Journal of the Chemical Society-Faraday Transactions Ii*, 1979, **75**, 790-798.
10. P. C. Lee and D. Meisel, *The Journal of Physical Chemistry*, 1982, **86**, 3391-3395.
11. W. P. Griffith and T. Y. Koh, *Spectrochimica Acta Part A: Molecular and Biomolecular Spectroscopy*, 1995, **51**, 253-267.
12. M. Osawa, N. Matsuda, K. Yoshii and I. Uchida, *The Journal of Physical Chemistry*, 1994, **98**, 12702-12707.
13. W. Hill and B. Wehling, *The Journal of Physical Chemistry*, 1993, **97**, 9451-9455.
14. Vandaveer and I. Fritsch, *Analytical Chemistry*, 2002, **74**, 3575-3578.
15. T. Shegai, A. Vaskevich, I. Rubinstein and G. Haran, *Journal of the American Chemical Society*, 2009, **131**, 14390-14398.
16. S. Cintra, M. E. Abdelsalam, P. N. Bartlett, J. J. Baumberg, T. A. Kelf, Y. Sugawara and A. E. Russell, *Faraday Discussions*, 2006, **132**, 191-199.
17. E. B. Wilson, *Physical Review*, 1934, **45**, 706.

18. A. Michota and J. Bukowska, *Journal of Raman Spectroscopy*, 2003, **34**, 21-25.
19. D. F. Shriver and P. W. Atkins, *Inorganic Chemistry*, Oxford University Press, Oxford, 1999.
20. A. Kudelski and W. Hill, *Langmuir*, 1999, **15**, 3162-3168.
21. R. M. Cole, J. J. Baumberg, F. J. Garcia de Abajo, S. Mahajan, M. Abdelsalam and P. N. Bartlett, *Nano Letters*, 2007, **7**, 2094-2100.
22. J. Molina, A. L. del Rio, J. Bonastre and F. Cases, *European Polymer Journal*, 2009, **45**, 1302-1315.
23. B. Kennedy, A. Glidle and V. J. Cunnane, *Journal of Electroanalytical Chemistry*, 2007, **608**, 22-30.
24. H. S. Jung, K. Kim and M. S. Kim, *Journal of Molecular Structure*, 1997, **407**, 139-147.
25. M. I. Alam, S. Beg, A. Samad, S. Baboota, K. Kohli, J. Ali, A. Ahuja and M. Akbar, *Eur. J. Pharm. Sci.*, 2010, **40**, 385-403.
26. I. Roy and N. Vij, *Nanomed.-Nanotechnol. Biol. Med.*, 2010, **6**, 237-244.
27. J. Gao, H. Gu and B. Xu, *Accounts of Chemical Research*, 2009, **42**, 1097-1107.
28. W. H. De Jong and P. J. A. Borm, *Int. J. Nanomed.*, 2008, **3**, 133-149.
29. R. Jain, P. Dandekar and V. Patravale, *Journal of Controlled Release*, 2009, **138**, 90-102.
30. V. I. Shubayev, T. R. Pisanic Ii and S. Jin, *Advanced Drug Delivery Reviews*, 2009, **61**, 467-477.
31. C. Y. Jing and Y. Fang, *Chem. Phys.*, 2007, **332**, 27-32.
32. K. Nakamoto, *Infrared and Raman spectra of inorganic and coordinated compounds, 3rd edition*, Wiley, 1977.
33. T. E. Barber, M. S. List, J. W. Haas and E. A. Wachter, *Appl. Spectrosc.*, 1994, **48**, 1423-1427.
34. F. McKenzie, K. Faulds and D. Graham, *Nanoscale*, 2010, **2**, 78-80.
35. D. Graham, K. Faulds, D. Thompson, F. McKenzie, R. Stokes, C. Dalton, R. Stevenson, J. Alexander, P. Garside and E. McFarlane, *Biochem. Soc. Trans.*, 2009, **37**, 697-701.
36. X. M. Qian and S. M. Nie, *Chemical Society Reviews*, 2008, **37**, 912-920.

37. M. Kerker, O. Siiman, L. A. Bumm and D. S. Wang, *Appl. Opt.*, 1980, **19**, 3253-3255.
38. X. L. Huang, B. Zhang, L. Ren, S. F. Ye, L. P. Sun, Q. Q. Zhang, M. C. Tan and G. M. Chow, *J. Mater. Sci.-Mater. Med.*, 2008, **19**, 2581-2588.
39. S. K. Tripathy and Y.-T. Yu, *Spectrochimica Acta Part A: Molecular and Biomolecular Spectroscopy*, 2009, **72**, 841-844.
40. T. Ignat, R. Munoz, K. Irina, I. Obieta, M. Mihaela, M. Simion and M. Iovu, *Superlattices and Microstructures*, 2009, **46**, 451-460.
41. L. Ren and G. M. Chow, *Materials Science and Engineering: C*, 2003, **23**, 113-116.
42. R. Wysokinski and D. Michalska, *Journal of Computational Chemistry*, 2001, **22**, 901-912.
43. B. Giese and D. McNaughton, *Biopolymers*, 2003, **72**, 472-489.
44. I. Zawisza, X. M. Bin and J. Lipkowski, *Langmuir*, 2007, **23**, 5180-5194.

6. Conclusions and further work

6.1. Conclusions

The overall aim of this thesis was to build upon previous research using SSV SERS substrates [1-7], by delving deeper into understanding the enhancement obtained, and to develop methods of tuning their sensitivity and surface properties to the chemical environment studied.

The origin of the spectral background continuum was probed further in Chapter 3, with an investigation into its dependence on applied potential. The intensity of the background was found to increase with increasing negative potential, but only whilst the adsorbate remained on the surface of the substrate. The background dropped rapidly with stripping of the substrate, which is in agreement with the current explanation [1].

The change in plasmonics of the substrate with binding an adsorbate was also probed through reflectance spectroscopy with our colleagues in Cambridge. The plasmon modes were found to shift slightly with chemisorption of an adsorbate, which is in essence an example of SPR spectroscopy. The formation of a Au-C bond through electrochemical reduction of a diazonium salt (DS), however, caused a significant increase in plasmonic absorption of the Mie modes. This was attributed to a physical sharpening of the void rim, which in turn leads to an increase in the Mie mode, and greater plasmonic absorption. The SERS spectrum of the adsorbed species for the DS is relatively poor, however, and this is thought to be caused by an induced polarisation in the molecule, which leads to a lower polarisability, and hence reduced Raman scattering cross section.

Chapter 4 focused on depositing an ultrathin layer of Pt onto the surface of the substrate, which would allow electrochemistry to study Pt surfaces, but with the optics of the underlying Au substrate for SERS. A comparison between ORC and SSV substrates was performed, which found that for *ex situ* spectra the PtAu SSV substrates had more Pt like characteristics, whilst PtAu ORC substrates behaved similarly to Au ORC. *In situ* spectroelectrochemistry on NaSCN in $NaClO_4$ solution gave similar results for both ORC and SSV substrates.

The SERS enhancement from an SSV substrate was increased by a further 10^2-10^3 in Chapter 5 through the use of metallic NPs. It was found that by tethering a Ag NP close to a structured surface the spectrum of the adsorbate is increased substantially, due to an extremely strong localised electromagnetic field. The enhancement has been found to be purely electromagnetic in nature, as the bands originating from the EM mechanism [8] are significantly stronger in the spectrum than those from CT.

If the NP is present on flat Au, then the CT bands dominate the spectrum, which in itself is significantly weaker than on a structured-NP section. This confirms that the structured area of substrate is critical to the additional enhancement. The enhancement is thought to be caused by the void acting as an antenna for incoming radiation, and focuses it into the area between the NP and substrate where the localised EM field is very strong.

The nature of the bond between adsorbate and NP is also integral to the additional enhancement. Mercaptoaniline (MA) binds to the NP *via* a primary amine, and has the strongest enhancement, whilst mercaptobenzoic acid (MBA) binds through a carboxylic acid, which is a much harder ligand [9] and binds less strongly to the NP, and consequently the MBA has a weaker enhancement than MA. The additional enhancement has also been observed using Au NPs, but to a slightly lesser degree. Theoretical calculations performed by the Cambridge group suggest that a void of 750 nm would offer the largest enhancement for Au NPs.

It has also been shown that by using NPs modified with mercaptoundecanoic acid (MUA) it is possible to observe drug molecules such as cis-platin at a self assembled monolayer. Cis-platin was adsorbed onto MUA coated NPs in such a way that allows NIR induced desorption [10]. The NPs were then added to a monolayer of MUA that acts as a simplified artificial cell membrane, and has been identified at the NP/SSV interface.

6.2.Further work

This project could develop in two distinct directions, namely electrochemistry using the borrowed SERS shown in Chapter 4, or further development of the NPs shown in Chapter 5.

6.2.1. Borrowed SERS

The ideal use for a PtAu SSV substrate is to study electrocatalytic reactions, such as methanol oxidation. Preliminary work shows that a PtAu SSV substrate performs methanol oxidation as expected (see Figure 6-1).

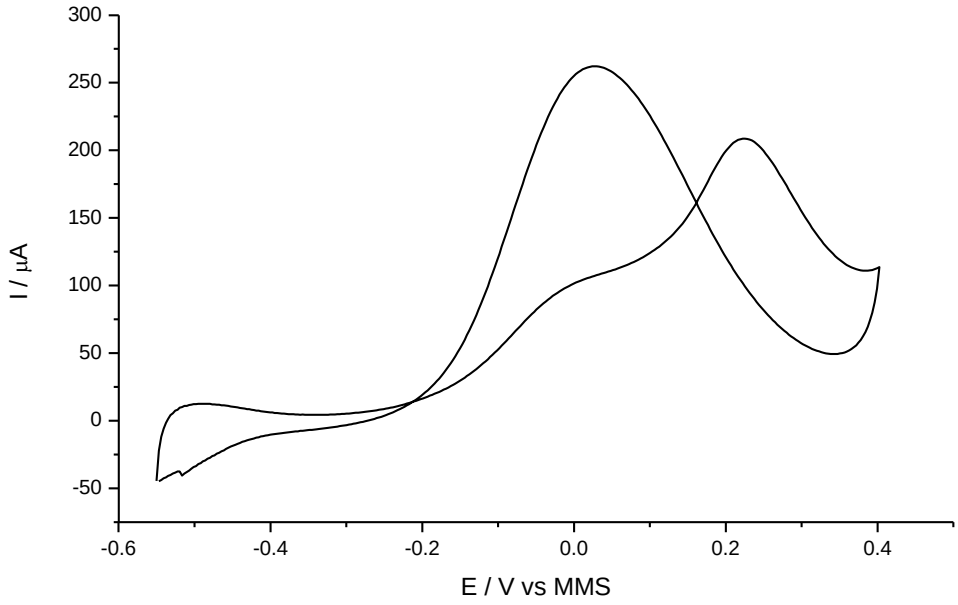

Figure 6-1 – Cyclic voltammogram of 0.5 M MeOH in 0.1 M H_2SO_4 with a PtAu SSV substrate as working electrode, Pt wire counter electrode and MMS reference electrode taken at 10 mV s^{-q}

So far, however, it has not been possible to obtain a Raman spectrum of CO on the electrode surface. This is most probably due to a detuning of the substrate's plasmonics by immersing the substrate in the electrolyte. Therefore the first step for future work is to accurately record the plasmonics *in situ*, with modification of Pt, and then to develop ideal substrate for this situation.

Once a perfectly tuned substrate has been developed, the Pt overlayer may be modified to investigate various fuel cell environments and reactions. An example may be the formation of spontaneously deposited Ru nanoislands [11], as Ru has been shown to increase CO tolerance of a catalyst.

Due to the reproducible and uniform nature of SSV substrates, the surface area under the laser spot may be estimated fairly accurately. This means that, (provided the same experimental conditions are used each time), semi-quantitative SERS may be achieved on a modified SSV substrate.

6.2.2. Nanoparticle SERS

Using NPs for drug delivery or diagnositics is a credible alternative to conventional methods [12-14]. It is important to understand exactly how the NPs is coated and how it behaves in biological systems. Using Langmuir-Blodgett DMPC bilayers such as those described by Zawisza *et al.* [15] an artificial cell membrane can be created on the surface of a SSV substrate.

The introduction of NPs to this will enable the study of how the NP passes through the membrane, by looking at structural changes to the DMPC. If the NP is coated with a drug, then any interactions between the drug and the bilayer will also be evident, giving more of an insight into the efficiency of the delivery system.

6.3. References

1. S. Mahajan, R. M. Cole, J. D. Speed, S. H. Pelfrey, A. E. Russell, P. N. Bartlett, S. M. Barnett and J. J. Baumberg, *Journal of Physical Chemistry C*, 2010, **114**, 7242-7250.
2. L. Cui, S. Mahajan, R. M. Cole, B. Soares, P. N. Bartlett, J. J. Baumberg, I. P. Hayward, B. Ren, A. E. Russell and Z. Q. Tian, *Physical Chemistry Chemical Physics*, 2009, **11**, 1023-1026.
3. M. E. Abdelsalam, S. Mahajan, P. N. Bartlett, J. J. Baumberg and A. E. Russell, *Journal of the American Chemical Society*, 2007, **129**, 7399-7406.
4. T. A. Kelf, Y. Sugawara, R. M. Cole, J. J. Baumberg, M. E. Abdelsalam, S. Cintra, S. Mahajan, A. E. Russell and P. N. Bartlett, *Physical Review B*, 2006, **74**.
5. S. Cintra, M. E. Abdelsalam, P. N. Bartlett, J. J. Baumberg, T. A. Kelf, Y. Sugawara and A. E. Russell, *Faraday Discussions*, 2006, **132**, 191-199.
6. J. J. Baumberg, T. A. Kelf, Y. Sugawara, S. Cintra, M. E. Abdelsalam, P. N. Bartlett and A. E. Russell, *Nano Letters*, 2005, **5**, 2262-2267.
7. M. E. Abdelsalam, P. N. Bartlett, J. J. Baumberg, S. Cintra, T. A. Kelf and A. E. Russell, *Electrochemistry Communications*, 2005, **7**, 740-744.

8. M. Osawa, N. Matsuda, K. Yoshii and I. Uchida, *The Journal of Physical Chemistry*, 1994, **98**, 12702-12707.
9. D. F. Shriver and P. W. Atkins, *Inorganic Chemistry*, Oxford University Press, Oxford, 1999.
10. X. L. Huang, B. Zhang, L. Ren, S. F. Ye, L. P. Sun, Q. Q. Zhang, M. C. Tan and G. M. Chow, *J. Mater. Sci.-Mater. Med.*, 2008, **19**, 2581-2588.
11. S. Park, A. Wieckowski and M. J. Weaver, *Journal of the American Chemical Society*, 2003, **125**, 2282-2290.
12. V. I. Shubayev, T. R. Pisanic Ii and S. Jin, *Advanced Drug Delivery Reviews*, 2009, **61**, 467-477.
13. I. Roy and N. Vij, *Nanomed.-Nanotechnol. Biol. Med.*, 2010, **6**, 237-244.
14. W. H. De Jong and P. J. A. Borm, *Int. J. Nanomed.*, 2008, **3**, 133-149.
15. I. Zawisza, X. M. Bin and J. Lipkowski, *Langmuir*, 2007, **23**, 5180-5194.